13th DELTA User Meeting

&

Annual Report 2017

Dortmund
29. November 2017

Edited by C. Sternemann, R. Wagner,
D. Lützenkirchen-Hecht (2017)

November 2017

Preface

Dear reader, dear colleague,

the last 12 month since the previous users meeting in November 2016 elapsed so quickly, and today, you see an overview of the users activities in that period of time. Again, synchrotron radiation from DELTA was used to address various scientific problems in physics, chemistry, biology and materials science, and we also have ongoing activities in archaeology – a historical painting has been investigated by using X-ray diffraction and spectroscopy by a group lead by Alex von Bohlen – of course in a non-destructive way. Although contributions related to the instrumentation at DELTA are not as prominent as in the years before, several developments, repairs and improvements took place in the past twelve month. Thus, this is the correct place to thank the DELTA machine group and the staff members for their continuous support and their contributions in keeping DELTA ready for operation, and also for taking care of the users.

Beamline BL 8 has been reserved for experiments using the lower end of the photon energy spectrum at the hard X-ray wiggler in the first half of 2017 providing an exceptional link between the soft and hard X-ray regimes. The dedicated setup has been optimized for this purpose, and a number of successful experiments were conducted, e.g. for the speciation of chlorine species in glasses as well as for sulphur K-edge spectroscopy in rubber samples. Due to the shut down of other instruments worldwide, X-ray spectroscopy in the region from 1-4 keV nowadays has become a unique feature of DELTA, and this has been also recognized by international users, e.g. from the UK. Although most of the DELTA users are still from universities and research centers in North Rhine-Westfalia, an increasing number of researchers from abroad visited DELTA for their experiments.

All the conducted projects would have been impossible without the financial support of the local government, the involved universities and research institutions – in particular the TU Dortmund – and the diverse funding agencies. We gratefully acknowledge all these different contributions and encourage our users to participate. We are looking forward to the upcoming beamtime periods, hoping that they will be as productive and successful as during the past years!

Christian Sternemann, Ralph Wagner & Dirk Lützenkirchen-Hecht

Contents:

Instrumentation

Status and Future of DELTA

S. Khan for the DELTA accelerator team[1]

Zentrum für Synchrotronstrahlung (DELTA), Technische Universität Dortmund

Operation and repairs in 2017

DELTA is a 1.5-GeV synchrotron light source operated by the TU Dortmund, comprising a linear pre-accelerator, a full-energy booster synchrotron and a storage ring with 115.2 m circumference. It is operated 2000 hrs/year for synchrotron radiation users and 1000 hrs/year for accelerator physics studies. The average availability (ratio of delivered to scheduled user beam time) in 2017 was 93.1%, dominated by problems with power supplies, the synchrotron extraction kicker pulser and the orbit correction system. After venting the southwest arc of the storage ring due to a leaking bellow at the photon absorber of beamline 11, the beam lifetime was low in August 2017 but recovered rather quickly to >10 h (at 100 mA) in September – see Fig. 1. During the summer shutdown, 32 coils of the undulator U250 were replaced without venting the vacuum chamber. The coils had been damaged when the cooling water supply failed in fall 2016.

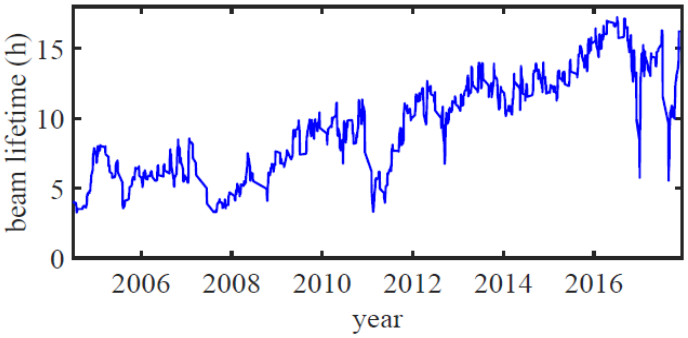

Figure 1: DELTA beam lifetime at a beam current of 100 mA from 2004 to 2017. The two recent dips correspond to a leak end of 2016 and venting the south-west arc in summer 2017.

Upgrades

A new superconducting wiggler [1] was ordered and will be delivered in 2018. In addition to a higher peak field (7 T instead of 5.3 T), the number of periods will be increased (9 instead of 5 periods) and the liquid-He consumption will be close to zero (instead of 130 l/week).

The klystron of the booster synchrotron was replaced by a 20-kW solid-state amplifier. In view of the higher energy loss due to the new wiggler, a second radiofrequency (RF) cavity will be added in 2018. A 75-kW solid-state amplifier to drive this cavity is already in place and a new FPGA-based low-level RF system has been ordered. Other improvements of the

[1] A. Althaus, W. Brembt, B. Büsing, G. Dahlmann, T. Dybiona, A. Erpelding, J. Friedl, P. Hartmann, B. Hippert, B. Isbarn, S. Khan, V. Kniss, S. Kötter, D. Krieg, C. Mai, A. Meyer auf der Heide, B. Riemann, D. Rohde, H.-P. Ruhl, B. Sawadski, D. Schirmer, G. Schmidt, T. Schulte-Eickhoff, M. Sommer, T. Weis

storage ring, such as a horizontal realignment of all vacuum chambers and magnets or upgrades of the control system [2], are in progress.

Other activities

The progress on other activities of the DELTA accelerator group such as new results from the short-pulse facility are presented in other articles of the 2017 Annual Report. In November 2017, DELTA hosted the 25th European Synchrotron Light Sources (ESLS) Workshop, attended by 30 experts from light sources in Europe, ranging geographically from ALBA in Spain to SOLARIS in Poland and even SESAME in Jordan. The two-semester course in accelerator physics is well attended, starting again in this winter semester with about 40 participants. The course comprises lectures, exercises, a seminar and excursions.

The future

By installing a new superconducting wiggler with superior properties, the scientific opportunities at the already overbooked beamlines will be increased. There is, however, still significant work to be done. A new vacuum vessel with improved absorbers to handle the increased radiation power is currently under design. The strong field of the wiggler is expected to influence the linear optics as well as the beam dynamics, and an extended commissioning period will be required once the new insertion device is in place.

A major future project is the upgrade of the short-pulse source using EEHG (echo-enabled harmonic generation) [3] to generate ultrashort radiation pulses at shorter wavelengths.

A design study for ultrafast electron diffraction (e.g., [4]) using a future few-MeV source of femtosecond electron bunches at DELTA has started.

The far future of accelerator physics at TU Dortmund has been addressed by a first workshop in July 2016. A follow-up workshop is scheduled for February 20th 2018.

References

[1] N. Mezentsev, Erik Wallén, *Superconducting Wigglers*, Sync. Rad. News 24:3, 3 (2011).

[2] D. Schirmer, A. Althaus, P. Hartmann, D. Rohde, *Control System Projects at the Electron Storage Ring DELTA*, Proc. of the ICALEPCS 2017, Barcelona, Spain, THPHA013.

[3] G. Stupakov, *Using the Beam-Echo Effect for Generation of Short-Wavelength Radiation*, Phys. Rev. Lett. 102, 074801 (2009).

[4] S. P. Weathersby et al., *Mega-electron-volt ultrafast electron diffraction at SLAC National Accelerator Laboratory*, Rew. Sci. Instrum. 86, 073702 (2015).

Results from the DELTA Short-Pulse Facility

A. Meyer auf der Heide, B. Büsing, S. Khan, N. M. Lockmann, C. Mai, R. Niemczyk, B. Riemann, B. Sawadski, M. Suski, P. Ungelenk

Zentrum für Synchrotronstrahlung (DELTA), Technische Universität Dortmund

Overview

The DELTA short-pulse facility [1] is based on coherent harmonic generation (CHG) [2]. Figure 1 shows the CHG scheme (left) and the layout of the facility (right). Seeding the electron bunches with femtosecond 800-nm or 400-nm laser pulses leads to microbunching and coherent emission of ultrashort pulses at harmonics of the laser wavelength. Further downstream, a gap in the longitudinal electron distribution gives rise to coherent emission of terahertz (THz) radiation.

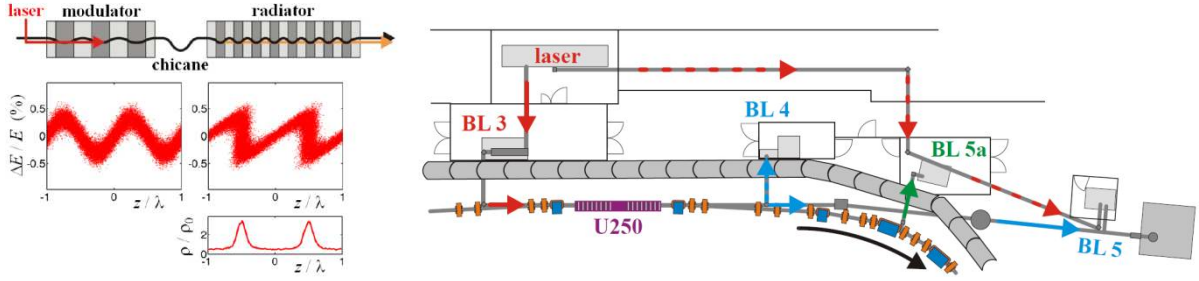

Figure 1: Left: CHG principle with laser-induced energy modulation in an undulator (modulator) converted into periodic microbunching by a magnetic chicane and coherent emission at laser harmonics in a second undulator (radiator). Right: Layout of the DELTA short-pulse facility with femtosecond laser system, laser beamline BL 3, undulator U250 (comprising modulator, chicane and radiator), diagnostics beamline BL 4, the soft-X-ray beamline BL 5 operated by the Forschungszentrum Jülich, and the dedicated THz beamline BL 5a.

Spectrotemporal control of CHG pulses

As shown in [3] for the case of the free-electron laser FERMI in Italy, the spectrotemporal properties of coherently emitted pulses can be controlled by the chirp of the seed pulses and the parameter r_{56} of the magnetic chicane. In early similar experiments at DELTA [4], CHG spectra were recorded using an avalanche photodiode while rotating the grating of a Czerny-Turner monochromator over several minutes. More recently, a gated image-intensified camera allows to obtain hundreds of single-shot spectra in the same period of time. For 800 nm seeding, Fig. 2 shows 600 spectra of the second and third harmonic under variation of r_{56} and for two different compressor settings of the laser amplifier. At large r_{56} values, microbunching occurs at two successive regions within the electron bunch. When the laser pulses pass through lenses and the vacuum window, positive chirp is increased while negative chirp is reduced leading to pronounced interference fringes only in the latter case.

Seeding with double pulses

A future application of a novel short-pulse scheme, echo-enabled harmonic generation (EEHG) [5], at DELTA will require a twofold energy modulation of the same electrons. To this end, first double-pulse seeding experiments were conducted. One example is seeding with

two 800-nm pulses in the same modulator [6]. As shown in the left part of Fig. 3, two laser pulses recorded using a standard CCD spectrometer show an interference pattern from which their relative delay can be calculated. Interference in the CHG spectra (Fig.3, center and right) demonstrates that the phase relationship between the two seed pulses is retained in the microbunching pattern and the coherently emitted radiation. For a delay in the picosecond range, interference is also observed in THz spectra directly after the laser-electron interaction and in sub-THz spectra one revolution later. Results on coherently emitted THz radiation and seeding with 800- and 400-nm pulses in different modulators [7] is described in other articles of the 2017 Annual Report.

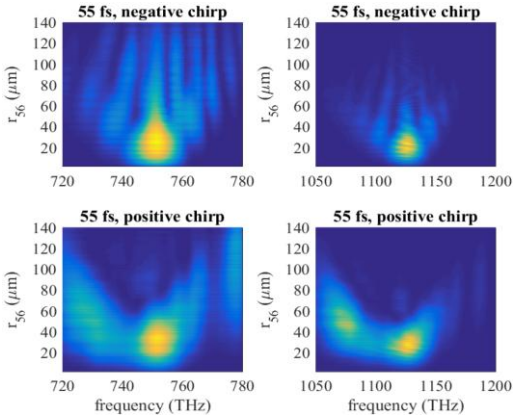

Figure 2: CHG spectra of the second (left) and third harmonic (right) of 800 nm seed pulses with negative chirp (top) and positive chirp (bottom), both with a pulse length of 55 fs under variation of the chicane strength r_{56}.

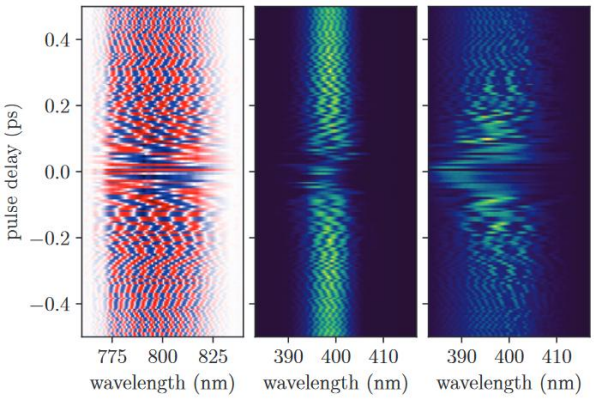

Figure 3: Under variation of the delay between two laser pulses, their spectral interference pattern (left) and interference of 400-nm CHG radiation are shown for small chirp (center, pulse length 50 fs) and a larger chirp (right, pulse length 90 fs) of the laser pulses.

References

[1] S. Khan et al., *Generation of Ultrashort and Coherent Synchrotron Radiation Pulses at DELTA*, Sync. Rad. News 26:3, 25 (2013).

[2] B. Girard et al., *Optical Frequency Multiplication by an Optical Klystron*, Phys. Rev. Lett. 53, 2405 (1984).

[3] D. Gauthier et al., *Spectrotemporal Shaping of Seeded Free-Electron Laser Pulses*, Phys. Rev. Lett. 115, 114801 (2015).

[4] S. Khan et al., *Spectral Studies of Ultrashort and Coherent Radiation Pulses at the DELTA Storage Ring*, Proc. of the 2016 Int. Part. Accel. Conf., Busan, Korea, 2851.

[5] G. Stupakov, *Using the Beam-Echo Effect for Generation of Short-Wavelength Radiation*, Phys. Rev. Lett. 102, 074801 (2009).

[6] S. Khan et al., *Pilot Experiments and New Developments at the DELTA Short-Pulse Facility*, Proc. of the 2017 Int. Part. Accel. Conf., Copenhagen, Denmark, 2878.

[7] A. Meyer auf der Heide et al., *Progress towards an EEHG-based Short-Pulse Source at DELTA*, Proc. of the 2017 Int. Part. Accel. Conf., Copenhagen, Denmark, 2878.

Survey and Alignment of the DELTA Magnets and Vacuum Chamber

G. Schmidt, T. Dybiona, S. Khan, P. Kortmann, T. Schulte-Eickhoff

Zentrum für Synchrotronstrahlung (DELTA), Technische Universität Dortmund

Overview

The performance of a storage ring regarding beam lifetime and stability depends on the alignment of all components. If the stored beam passes through the center of the focusing magnets, nonlinearities are minimized, the model of the magnetic optics is more accurate and the machine is easier to operate. Furthermore, magnets moved by the contact to the vacuum chamber, which is subject to thermal motion, have been a major problem at DELTA [1].
In a mayor effort over the last two years, all magnets and vacuum chambers of the storage ring were realigned vertically. The improvement is evidenced, e.g., by an improved beam lifetime, stability, reproducibility of magnet settings, and by a reduced radiation level in the DELTA hall. The fact that the beam can be stored during test operation with nearly all the vertical corrector magnets switched off (which was previously impossible) demonstrates the improvement of the vertical alignment. As a next step, the horizontal alignment has started in 2016.

Alignment Plates

To improve the position accuracy and to reduce the time needed for a survey, about 180 alignment plates (Figure 1) to place Taylor-Hobson spheres in a defined way were manufactured in the workshop of the TU Dortmund physics department.
Checking and comparing the alignment plate parameters was made possible using an adjustment and measurement environment developed and built by the DELTA workshop. Here, dial indicators [2] with a reading accuracy better than 0.01 mm allow to measure and adjust all important parameters in one step (Figure 2).

Figure 1: Alignment plates before installation.

Figure 2: Dial indicators measuring the position of a Taylor Hobson placed on an alignment plate.

Previously, a small set of alignment plates was used for the survey for all magnets resulting in a tedious and error-prone procedure. The accuracy of the new plates has been improved to a level better than 0.1 mm in horizontal and vertical direction. After careful measurement and adjustment of all important parameters, the alignment plates are permanently mounted on top of the magnets. A complete survey of the machine using a Leica Absolute Tracker AT 402 [3] is now possible within two days instead of an entire week.

Radial Alignment

It was necessary to generate a reference coordinate system for the DELTA magnets which takes into account several boundary conditions. One of the constraints is that the quadrupole magnets cannot be adjusted longitudinally. Another one is that the length of the electron orbit should not change during the realignment. The measured radial offsets with respect to the reference coordinate system are shown in Figure 3.

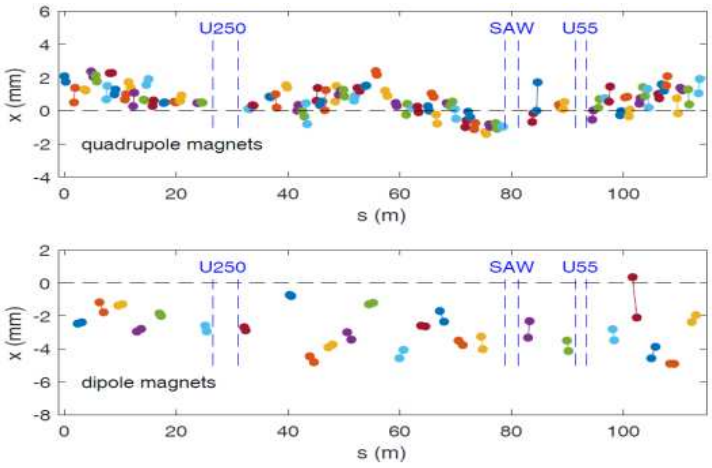

Figure 3: Radial displacement of quadrupole (top) and dipole magnets (bottom) as function of longitudinal position according to a survey in 2016. Each magnet is equipped with two alignment marks shown as two dots of the same color.

After a first test it was decided to perform the radial adjustment in steps localized within up to five quadrupoles. This allows to adjust the corresponding corrector magnet and to continue machine operation without time consuming optimization. Several adjustment steps were done in the western part of the storage ring. The anticipated setting of the respective corrector magnet always allowed to store beam after an alignment intervention. User operation was possible at all beamlines without loss of intensity by retaining the orbit position. In order not to impair user operation, the magnets were moved in several steps to their final position. The experience with alignment steps of up to 1 mm was positive. The vacuum chamber movement during magnet alignment is monitored by dial indicators. The final adjustment of the vacuum chamber is foreseen after all quadurpole magnets have reached their target position. The radial adjustment of dipole magnets is less critical and will be done after the quadrupole adjustment has been completed.

Outlook

The final goal of the alignment program is a stored electron beam passing through the center of the aligned quadrupole magnets. Finally, sensitive beamlines, which have already been adjusted vertically, have to be aligned horizontally to the new electron reference orbit.

References

[1] G. Schmidt et al., *Position Sensors for Monitoring Accelerator Magnet Motion at DELTA*, EPAC 2002 proceedings

[2] Hahn und Kolb Werkzeug GmbH, D-71636 Ludwigsburg

[3] Hexagon Metrology GmbH, *Leica Absolut Tracker AT 402*, D-35578 Wetzlar

Coupled-Bunch Instability Suppression Using RF Phase Modulation at DELTA

M. Sommer, B. Isbarn, S. Kötter, T. Weis

Zentrum für Synchrotronstrahlung (DELTA), Technische Universität Dortmund

Introduction

Besides the effects on the longitudinal phase space of RF phase modulation [1,2], it is also able to suppress the excitation of coupled-bunch instabilities [3]. This effect has been investigated with the bunch-by-bunch feedback system installed at DELTA [4]. The system is mainly used as a diagnostic tool to measure the damping rates of the coupled-bunch modes. In addition, it is used to excite specific modes of the beam for further investigations.

The RF phase modulation system is fully characterized by the two parameters, modulation frequency f_{mod} and amplitude φ. In order to get information about the interaction of RF phase modulation and coupled-bunch instabilities, these two parameters are scanned and the influence on the damping rates are measured.

Finding the Optimum Frequency

To determine the optimum modulation frequency, at which the suppression of the RF phase modulation is at its maximum, one coupled-bunch mode is excited by the bunch-by-bunch feedback system and the spectral power at the mean synchrotron frequency of all bunches, which represents the sum of all single bunch oscillations, is obtained for different modulation frequencies f_{mod} = 28 kHz to 54 kHz with $\varphi \approx 2.2°$.

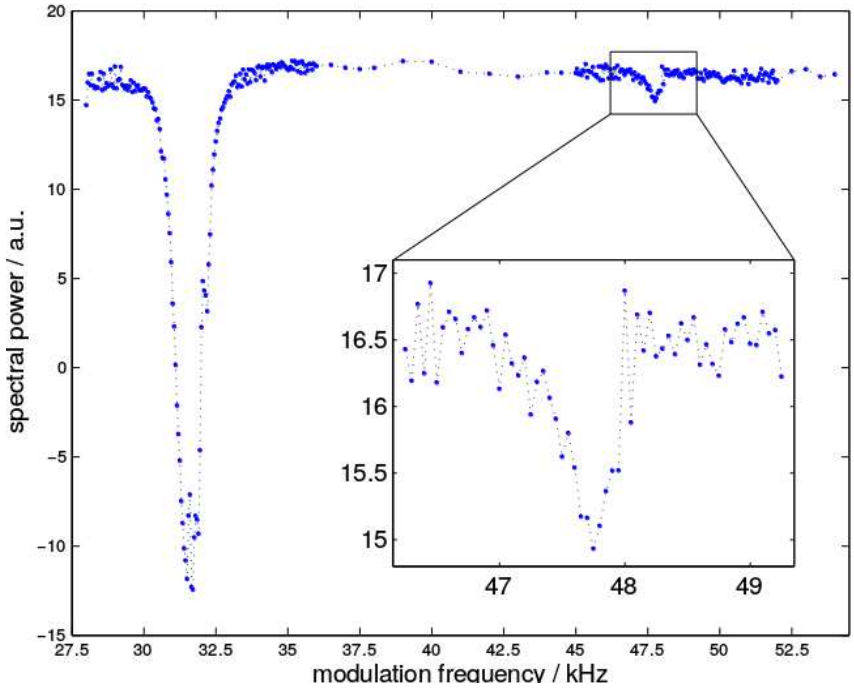

The results show, that the beam instability strongly decreased when the modulation frequency is a multiple of the synchrotron frequency f_s = 16.05 kHz with a higher effect at f_{mod} being at twice f_s as shown in Figure 1 [5].

Figure 1: Spectral power at the mean synchrotron frequency of all bunches, representing the sum of all single bunch oscillations, as a function of the modulation frequency. The highest stability can be achieved at twice the synchrotron frequency.

Coupled-Bunch Instability Damping Rates as a Function of the Modulation Amplitude

With the optimum modulation frequency, additional studies sweeping the modulation amplitude were done to examine the effect on coupled-bunch instability damping rates.

As a first step, a new measurement method was developed to be able to determine damping rates in the presence of RF phase modulation. After one calibration measurement, the beam is excited by the bunch-by-bunch feedback system into saturation and the damping rate can be calculated from the saturation amplitude (for additional information see [6]).

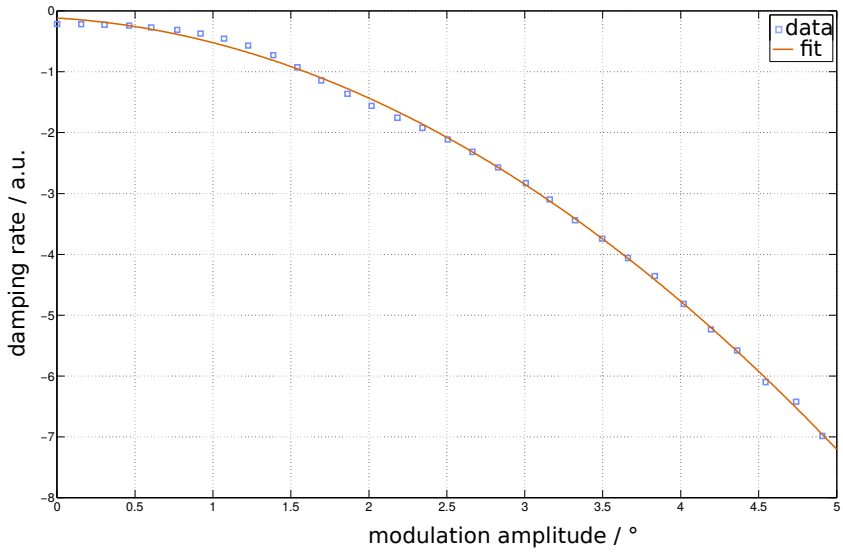

With this method, the damping rate of one specific coupled-bunch mode could be obtained for modulation amplitudes up to 5° with $f_{mod} = 2\ f_s$. The results are shown in Figure 2 and demonstrate, that the damping rates are proportional to the square of the modulation amplitude.

Figure 2: Damping rate of mode 12 as a function of the modulation amplitude at a beam current around 39 mA. Using a second-order polynomial fit shows a quadratic correlation.

References

[1] H. Huang, et. al., *Experimental determination of the Hamiltonian for synchrotron motion with rf phase modulation*, Phys. Rev. E48, pages 4678-4688, 1993.

[2] J.M. Byrd, et. al., *Nonlinear Effects of Phase Modulation in an Electron Storage Ring*, Phys. Rev. E57, 4706, 1997.

[3] S. Khan, et. al., *Studies and Control of Coupled-Bunch Instabilities at DELTA*, IPAC '10, Kyoto, Japan, WEPEB032, 2010.

[4] M. Höner, *Investigation of Transient Processes at the DELTA Electron Storage Ring Using a Digital Bunch-by-Bunch Feedback System*, dissertation, TU Dortmund University, Dortmund, Germany, 2015.

[5] M.Sommer, et. al., *Coupled-Bunch Instability Suppression Using RF Phase Modulation at the DELTA Storage Ring*, IPAC '15, Richmond, VA, USA, MOPWA034, 2015.

[6] M.Sommer, et. al., *Interaction of RF Phase Modulation and Coupled-Bunch Instabilities at the DELTA Storage Ring,* IPAC '16, Busan, South Korea, TUPOR027, 2016.

Radiofrequency Upgrade at DELTA

P. Hartmann, W. Brembt, V. Kniss, J. Friedl, S. Khan, D. Schirmer, G. Schmidt, T. Weis

Zentrum für Synchrotronstrahlung (DELTA), Technische Universität Dortmund

The advent of a new wiggler (9.8 kW irradiated power at 100 mA beam current) will make it necessary to increase the overall accelerating voltage in the storage ring DELTA. Calculations clearly favor the installation of a second radiofrequency (RF) resonator equipped with a dedicated RF amplifier of at least 50 kW power at 500 MHz in the DELTA storage ring [1]. At the same time, the booster RF tube amplifier suffered from damage that happened during a power surge in 2014. Thus, in 2016, two power amplifiers, 20 kW for the booster and 75 kW for the storage ring, and one EU-type RF resonator [2] were ordered.

The booster amplifier was delivered, installed and commissioned in a 2-week shutdown in February 2017. As of mid-January 2018 it has done almost 3000 hours of operation without any problems. Due to a better AC-to-RF efficiency of the transistor amplifier, the cost for electricity is lowered significantly. We expect a return of investment after approx. 5 years [3].

While the environmental installations for the new booster amplifier were reasonably low, the new storage ring RF required the installation of a new power line delivering 150 kW electrical power to the amplifier and two new cooling water lines, one to the amplifier and one to the new resonator location inside the ring, with 75 kW cooling power, each. Furthermore, a 6 1/8” coaxial tube capable of transporting 75 kW of RF power from the amplifier to the cavity has to be installed.

The storage ring amplifier (see Fig. 1) was delivered, installed, and tested in April 2017.

Figure 1: Radiofrequency amplifier delivering 75 kW RF power for the storage ring DELTA.

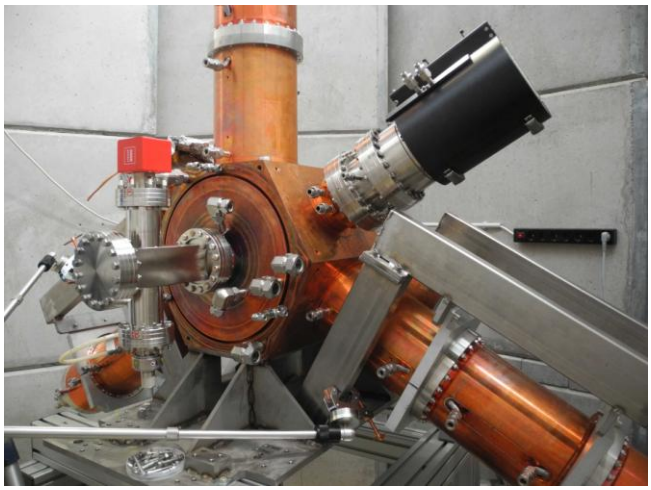

Figure 2: EU-type resonator [2] for 500 MHz with coupler and plunger (black ended) and absorbers for higher-order modes.

During the summer shutdown, a power circulator and two dummy loads were installed, waiting ever since for the installation of the RF resonator in a radiation-protected area outside the storage ring.

After some problems with the manufacturing of the ferrite RF absorbers in the higher-order mode (HOM) tubes of the RF resonator (copper-colored radial tubes in Fig. 2) it was finally delivered in December 2017.

Preparations for the commissioning of the amplifier together with the resonator at 75 kW RF power are in progress. Commissioning is expected to start in February 2018 so that the ring installation of the resonator can take place in the summer shutdown 2018.

References

[1] P. Hartmann et al., *RF Upgrade Plans at DELTA*, 20th ESLS-RF Meeting, Brugg, Switzerland (2016).

[2] E. Weihreter, *Status of the European HOM Damped Normal Conducting Cavity*, Proc. EPAC 2008, Genoa, Italy, 2932 (2008).

[3] P. Hartmann et al., *RF Upgrade at DELTA*, 21st ESLS-RF Meeting, Cracow, Poland (2017).

Recent Upgrades of the YACS Cavity Solver Code

B.D Isbarn, S. Kötter, B. Riemann, M. Sommer, T. Weis

Zentrum für Synchrotronstrahlung (DELTA), Technische Universität Dortmund

Introduction

YACS is a finite element method solver for bounded electrodynamic eigenvalue problems [1,2]. It was specifically designed to solve the eigenfrequency spectra of highly resonant superconducting multicell cavities. YACS utilizes the rotation symmetry [3] of common cavity designs to reduce the degrees of freedom (2.5D problem), and state of the art numerical techniques to efficiently solve the arising sparse eigenvalue problems.

Implementation of Arbitrary Order Basis Functions and Curved Elements

To further improve its performance the most recent revision of YACS now supports combinations of both arbitrary order basis functions [4] and arbitrary order curved elements. This led to a significant improvement in convergence rates, such that YACS now outperforms conventional commercial 2D, 2.5D and 3D codes by a large margin when using high order basis functions and / or curved elements (see Fig. 1).

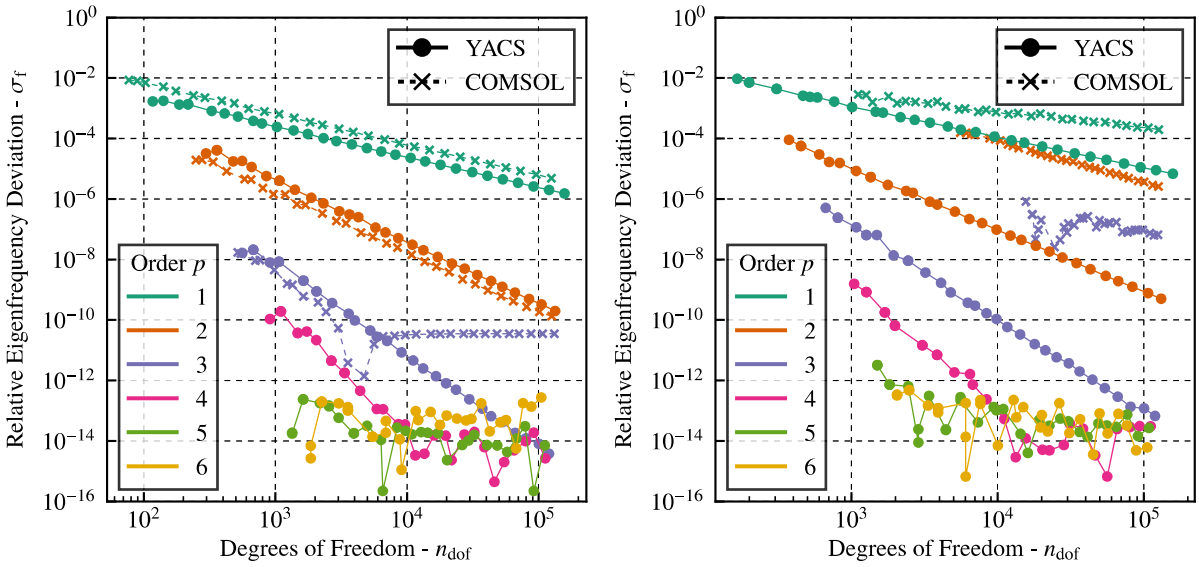

Figure 1: Relative eigenfrequency deviation of the first monopol (left) and dipole (right) mode of a pillbox resonator, obtained from YACS and COMSOL [5], as a function of the number of degrees of freedom for different polynomial orders of the basis functions. The frequency deviations were calculated with respect to the analytical solution [6].

Spline Cavity Parameter Space Scan

Despite their popularity in superconducting cavity designs, the optimization of cavities that utilize an elliptical parametrization is difficult due to their large parameter space. In order to circumvent this issue a new cavity parametrization has been proposed based on cubic spline curves [7]. This parametrization shares the major benefits of elliptical cavities with a substantially reduced parameter space. To further investigate this new parameterization, a complete parameter space scan for the non-reentrant cavity regime has been carried out with YACS (see Fig. 2).

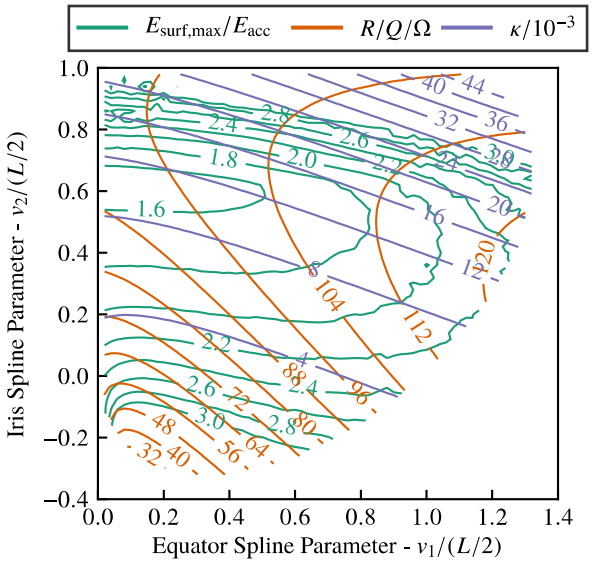

Figure 2: Parameter space scan for the subset of spline parameters within the non-reentrant regime of cubic spline cavities.

Higher Order Spline Cavity Optimization Algorithm

In contrast to the elliptical parametrization, the order of spline cavities can be chosen arbitrarily. In addition the degree elevation technique which enables the increase of curve order without modifying the curve shape has been used to implement a new optimization technique, which gradually increases the order of the spline curve to efficiently find the optimal solution for a high order spline cavity based on the optimal solution of lower order cavities.

References

[1] B.D. Isbarn, B. Riemann, M. Sommer, T. Weis, *YACS – A new 2.5D FEM eigenmode solver for axisymmetric RF-structures*, Proc. of the IPAC 2015, Richmond, VA, USA, MOPWA033.

[2] B.D. Isbarn, B. Riemann, M. Sommer, T. Weis, *Optimization of multicell microwave cavities using YACS*, Proc. of the IPAC 2017, Copenhagen, Denmark, THPAB011.

[3] R. Hiptmair, P.D.R. Ledger, *Computation of resonant modes for axisymmetric Maxwell cavities using hp-version edge finite elements*, Int. J. Numer. Meth. Eng. 62, 12 (2005).

[4] M. Ainsworth, J. Coyle, *Hierarchic hp-edge element families for Maxwell's equations on hybrid quadrilateral/triangular meshes*, Comput. Methods Appl. Mech. Engrg 190, 49-50 (2001).

[5] COMSOL Multiphysics 5.2, http://www.comsol.com.

[6] T. Wangler, *RF Linear Accelerators*, Wiley-VCH, Weinheim, Germany (2007).

[7] B. Riemann, T. Weis, A. Neumann, *Design of SRF cavities with cell profiles based on bezier splines*, Proc. of the ICAP 2012, Rostock-Warnemünde, Germany, WEP14.

Progress towards EEHG at the DELTA Short-Pulse Facility

B. Büsing, S. Khan, N. M. Lockmann,
C. Mai, A. Meyer auf der Heide, B. Riemann, P. Ungelenk
Zentrum für Synchrotronstrahlung (DELTA), Technische Universität Dortmund

Overview

Echo-enabled harmonic generation (EEHG) is a seeding scheme for free-electron lasers proposed in 2009 [1]. As shown in Fig. 1 (left), it is based on a twofold laser-induced modulation of the energy of relativistic electrons. Test experiments were conducted at SLAC in the US and SINAP in China [2,3]. EEHG is also proposed as a method to generate ultrashort pulses in storage rings [4,5]. Compared to coherent harmonic generation (CHG) presently employed at the DELTA short-pulse facility [6], EEHG will enable coherent emission at higher harmonics of the laser wavelength. DELTA is presently the only storage ring worldwide at which the implementation of EEHG is planned.

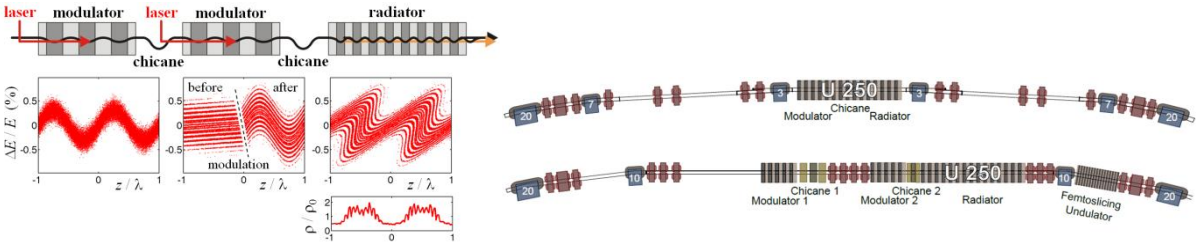

Figure 1: Left: EEHG principle with twofold laser-induced energy modulation in two undulators (modulators) converted into microbunching by magnetic chicanes and coherent emission at high laser harmonics in a third undulator (radiator). Right: Layout of the northern part of the DELTA storage ring (top) and a possible future configuration with a 20 m long straight section for EEHG [7].

Magnetic lattice of the storage ring

Starting from the layout shown in Fig. 1 (right) [7], the magnetic lattice of a 20 m long straight section in the northern part of the DELTA storage ring was reconsidered [8,9], resulting in two new configurations with moderate beta functions, zero dispersion in the straight section and large dynamic aperture.

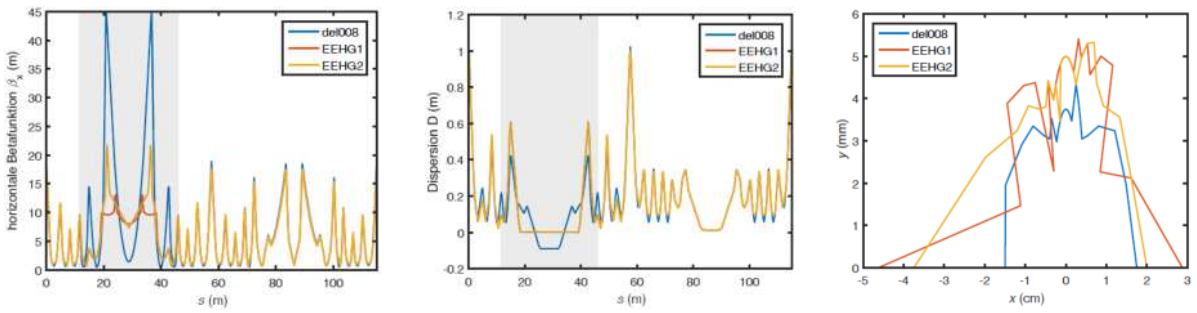

Figure 2: Horizontal beta function (left), horizontal dispersion (center) and dynamic aperture (right) for the present DELTA lattice (blue) and two possible EEHG lattices (red, orange) studied in [8].

Hardware

For the implementation of EEHG at DELTA, two new electromagnetic modulators (period length 200 mm, 7 periods) are already in house and tested [10] while the present U250 undulator (period length 250 mm, 17 periods) will be employed as radiator. Vacuum chambers for the modulators are currently manufactured and new dipole chambers were designed [8].

Seeding with double pulses

Energy modulation with 800- and 400-nm laser pulses in two different undulators was demonstrated at DELTA [11] verifying the spatial and temporal overlap of the seed pulses with the same electrons using three different methods as shown in Fig. 3.

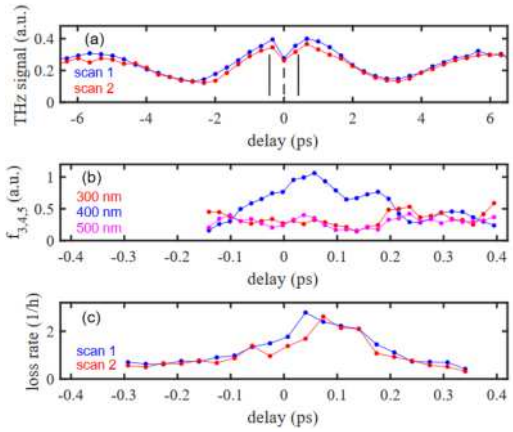

Figure 3: Picosecond variation of the delay between two seed pulses while recording THz radiation intensity (top), femtosecond variation of the delay while recording Fourier coefficients of the THz signal for sub-wavelength delay (center), and beam loss rate with reduced energy acceptance, i.e. low radiofrequency power (bottom). See [11] for details.

References

[1] G. Stupakov, *Using the Beam-Echo Effect for Generation of Short-Wavelength Radiation*, Phys. Rev. Lett. 102, 074801 (2009).

[2] Z. Zhao et al., *First lasing of an echo-enabled harmonic generation free-electron laser*, Nature Photonics 6, 360 (2012).

[3] E. Hemsing et al., *Echo-enabled harmonics up to the 75th order from precisely tailored electron beams*, Nature Photonics 10, 512 (2016).

[4] C. Evain et al., *Soft x-ray femtosecond coherent undulator radiation in a storage ring*, New J. Phys. 14, 023003 (2012).

[5] R. Molo et al., *EEHG and Femtoslicing at DELTA*, Proc. FEL 2013, New York, USA, 594.

[6] S. Khan et al., *Generation of Ultrashort and Coherent Synchrotron Radiation Pulses at DELTA*, Sync. Rad. News 26:3, 25 (2013).

[7] R. Molo, *Towards Echo-Enabled Harmonic Generation at FLASH1 and DELTA*, Dissertation, TU Dortmund (2017).

[8] B. Büsing, *Teilchenoptische Auslegung und Entwicklung von Dipolkammern für die EEHG-basierte Kurzpulsquelle bei DELTA*, Master Thesis, TU Dortmund (2017).

[9] J. Bengtsson, Moptima AB, Lund, Sweden.

[10] D. Zimmermann, *Aufbau eines Magnetmessstandes zur Feldvermessung von Undulatoren bei DELTA*, Master Thesis, TU Dortmund (2016).

[11] S. Khan et al., *Seeding of Electron Bunches in Storage Rings*, Proc. FEL 2017, Santa Fe, USA, MOP027.

Analysis of closed-orbit response matrices from storage rings without input of model optics

B. Riemann

Zentrum für Synchrotronstrahlung (DELTA), Technische Universität Dortmund

Based on experiments at the DELTA storage ring, an algorithm to retrieve information about actual beam optics without the previously necessary input of computer-generated ideal model optics has been developed. This algorithm with the name Closed-Orbit Bilinear-Exponential Analysis (COBEA) [1] uses the monitor-corrector response matrix, which is routinely recorded at common storage rings, and has been successfully validated at DELTA [1], the Metrology Light Source and at BESSY II [1,2].

Due to the Floquet-periodic boundary condition for particle trajectories in storage rings, quasi-static beam perturbations and eigenfrequency information are closely connected. While constructing a response matrix from beam optics is an elementary task, the opposite process of decomposing a response matrix into optics is a non-trivial problem. This problem has been solved with a minimum of necessary input data by COBEA; the key idea is the generation of "virtual" single-particle oscillation data at two beam position monitors (see Fig. 1). The algorithm may also be of use outside of beam diagnostics, and its use for orbit correction is under active investigation [3].

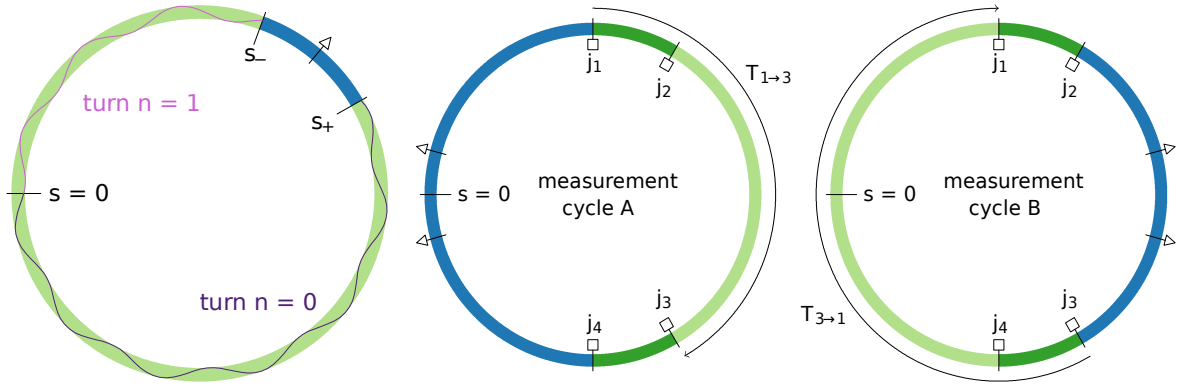

Figure 1: Working principle the first COBEA layer, taken from [1]. Left: Outside of any perturbation (blue), a closed-orbit perturbation is a free betatron oscillation. Center and Right: Using information about the ordering of monitors (boxes) relative to correctors (arrows), a one-turn transfer matrix can be generated using the two sub-matrices $\mathbf{T}_{1\to3}$ and $\mathbf{T}_{3\to1}$. These matrices are in turn generated using measured closed-orbit perturbations (response matrix). The one-turn matrix is equivalent to oscillation data obtained at the eigenfrequencies of betatron motion in the storage ring and used in subsequent steps to reconstruct beam optics parameters at the locations of all beam position monitors.

References

[1] B. Riemann, *The Bilinear-Exponential Closed-Orbit Model and its Application to Storage Ring Beam Diagnostics,* Dissertation, TU Dortmund University (2016). doi:10.17877/DE290R-17221

[2] B. Riemann et al., Proc. IPAC 2017, Copenhagen, Denmark, MOPIK066 (2017).

[3] S. Koetter, B. Riemann and T. Weis, Proc. IPAC 2017, Copenhagen, Denmark, MOPIK065, (2017).

Contributions to the Future Circular Hadron-Hadron Collider study

B. Riemann

Zentrum für Synchrotronstrahlung (DELTA), Technische Universität Dortmund

DELTA is participating in impedance and beam instability studies for the Future Circular Hadron-Hadron Collider (FCC-hh), a proposal for a storage ring with ~97 km circumference to be located in the Geneva area [1].

The diameter and temperature of the FCC-hh beamscreen in all insertion regions (main experiments, injection / extraction, rf systems, collimation systems), as well as beam-optical functions, have a strong influence on the transverse and longitudinal resistive-wall impedance [2], which, if not properly considered and limited, can be the cause of beam instabilities. Impedance computations have shown that further opening of the beamscreen aperture near the main experimental regions A (see Fig. 1) and G is indicated [2]. Updated results will be part of the upcoming FCC-hh Conceptual Design Report.

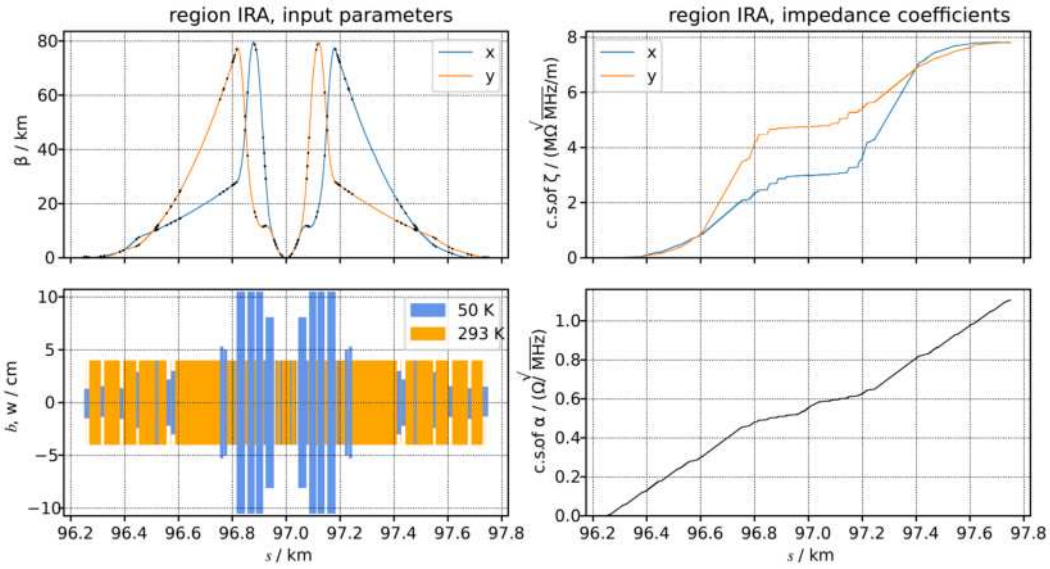

Figure 1: Impedance computation for one main experiment insertion (A) of FCC-hh with focusing setup β* = 0.3 m, taken from [2]. Top Left: Beta function input values [3] (max. ~80 km) and their effective interpolation used during integration via quadrature rules. Bottom Left: Visualization of FCC-hh beamscreen diameter [3] and assumed temperatures – the material is assumed to be copper. Top Right: Cumulative plot of transverse impedance coefficient, computed from shown beamscreen properties and (considerably large) beta functions. The final value is a significant fraction of the total ring impedance, although the insertion length is only ~1.6 km. Bottom Right: Cumulative plot of longitudinal impedance coefficient. The longitudinal instabilities are only slightly effected by the insertion, as they do not depend on the large values of beta functions.

References

[1] W. Bartmann et al., *Beam Dynamics issues in the FCC*, Proc. 57th ICFA Advanced Beam Dynamics Workshop on High-Intensity and High-Brightness Hadron Beams, Malmö, Sweden (2016).

[2] B. Riemann, *Resistive-Wall Impedance of interaction regions*, presentation at EuroCirCol meeting, Geneva, Switzerland (2017).

[3] S. Arsenyev and A. Langner, personal communication (2017).

Development of a Scanning Reflection X-ray Microscope (SRXM)

A. Schümmer[1], M. Gilbert[1], C. Jansing[1], H.-Ch. Mertins[1],
R. Adam[2], C. M. Schneider[2], L. Juschkin[3], U. Berges[4]

[1] University of Applied Sciences, Münster Stegerwaldstraße 39, 48565 Steinfurt, Germany
[2] Forschungszentrum Jülich, Wilhelm-Johnen-Straße, 52428 Jülich, Germany
[3] Rhein Westfälische Technische Hochschule Aachen, Templergraben 55, 52062 Aachen, Germany
[4] DELTA / TU Dortmund Maria-Goeppert-Mayer-Straße 2, 44227 Dortmund

Theoretical and experimental work started within a new project of a scanning reflection x-ray microscope (SRXM) designed for beamline 12 at DELTA. The operation in reflection mode will allow the study of surfaces and interfaces even of thick samples. It also will enable imaging of magnetic domains in buried layers exploiting magneto-optical reflection spectroscopy like XMLD and XMCD. Working at the DELTA beamline 12 in the extreme ultraviolet (EUV) regime, EUV synchrotron radiation near the 3p absorption edges of 3d transition metals about 50eV – 70eV, results in sufficient reflected intensities, which are about two orders of magnitude larger than those at the respective 2p5 edges due to the higher reflectivity in the EUV regime [1, 2].

The setup of our projected SRXM shown in Fig 1.It consists of a high-resolution zone plate that focuses the beam on a small spot of 250 nm diameter on the sample. For more details about the mechanical properties see Tab.1. A central beam stop (CBS) is implemented in the zone plate to block zero order radiation. In contrast to STXM the sample is illuminated in gazing incidence (Tab. 1). This angle allows magneto-optical reflection spectroscopy as T-MOKE, L-MOKE or XMLD. The contrast depends on the orientation between the light's linear polarization vector and the magnetization direction. This will enable the detection of magnetic domains of ferromagnetic and anti-ferromagnetic materials.

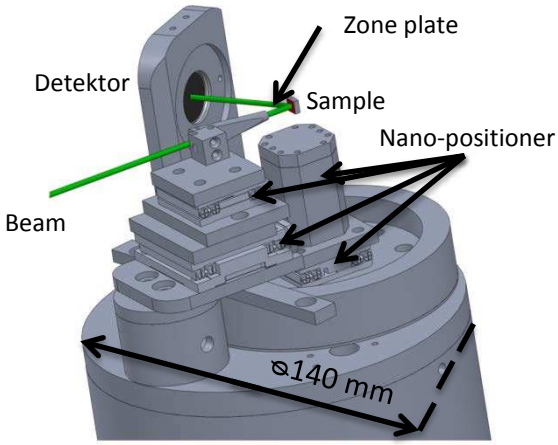

Fig. 1 Setup of SRXM

Feature	Scanning horizontal	Scanning vertical	Re focusing	Angle to surface
Value	±10 mm in 50nm Steps	±6 mm In 100 nm Steps	±10mm in 50 nm Steps	0°-60° (1°accurancy)

Tab 1 – Mechanical properties of the designed SRXM

As a first test of our setup and software a scan of a Siemensstar like test pattern was performed. For this scan a pinhole was used instead of a zone plate to create a visible spot on the test sample using the visual part of the synchrotron radiation. A comparison of a picture taken by a light microscope and the SRXM proves the capability of our mechanical setup (Fig. 3).

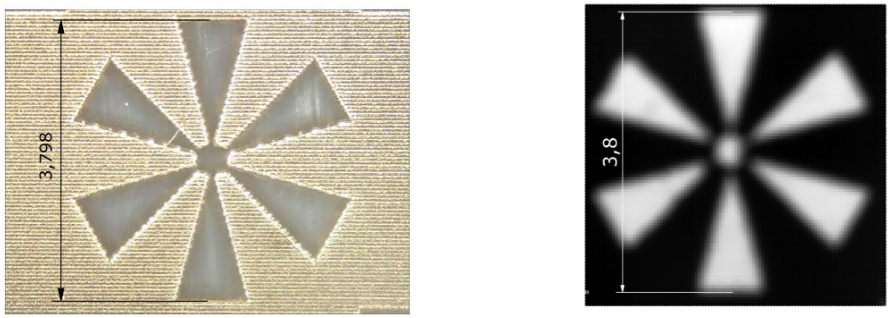

Fig. 2: Left: Picture of a Siemens star like sample taken by a light microscope
Right: Scan of a Siemens star like sample taken by the SRXM setup with pinhole optic and visible synchrotron radiation

To realize high resolution a zone plate with a resolution smaller 1.25µm will be used as EUV optic. A zone plate structure has been calculated with respect to the energy range from 40 to 70 eV and energy resolution E/ΔE of 50 according to beam characteristics of BL12. The calculating results in a zone plate of 0.26 mm diameter with a focal length of 15 mm at the energy of 60eV and an outermost zone width of 1250 nm. We optimized the fabrication process using e-beam lithography and reactive ion etching processes. This allowed the creation of an Au structure on SI3N4 or a free-standing Au structure (Fig. 4).

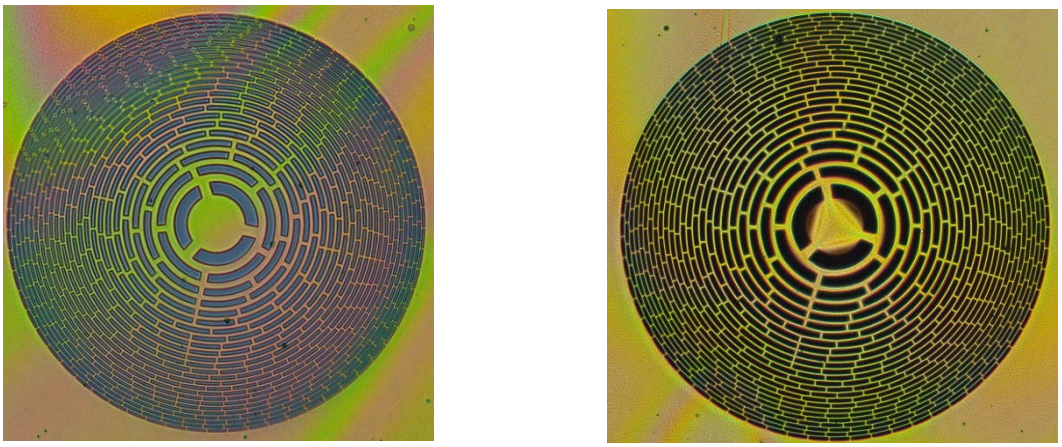

Fig. 3: Left: Picture of an Au zone plate on Si3N4 membrane taken with visual microscope
Right: Picture of an Au free standing zone plate taken with visual microscope

In the first experiments a photodiode was tested as detector. As the nano positioners use light for position detection an Al filter had to be placed in front of the Photodiode to block the infra-red light from the positioners read out system. We measured the photonflux entering the experimental chamber to a value of $2*10^{11}$ photons/s. To check the photon flux is high enough to be measured with the photodiode we measured the transmission of the zone plate ($T=7,3*10^{-3}$) and the reflectance of a test pattern ($R=6.25*10^{-4}$) consisting of gold structures grown on Si3N at an angle of 60°. The photon flux hitting the photodiode would generate a signal in the same magnitude as the dark current. Therefore another detector a micro channel plate (MCP) will replace photodiode.

The next steps in the development of the SRXM will be the integration and testing of the MCP as detector. With this new detector the zone plate can be characterized especially the resolution. When these steps are completed the final work can be started the addition of a magnetization unit to enable the SRXM to perform magnetic imaging.

[1] M. F. Tesch, M. C. Gilbert, H.-Ch. Mertins, D. E. Bürgler, U. Berges, and C. M. Schneider "X-ray magneto-optical polarization spectroscopy: an analysis from the visible region to the x-ray regime"., Applied Optics 52, 4294-4310 doi: 10.1364/AO.52.004294 (2013)

[2] H.-C. Mertins, S. Valencia, A. Gaupp, W. Gudat, P.M. Oppeneer; C.M. Schneider „Magneto-optical polarisation spectroscopy with soft X-rays" Appl. Phys. A80,1011-1020 (2005)

Soft X-ray Spectroscopy

XPS measurements of Co/Cu(100)

Nadine Heßler[(a,b)], Karim Shamout[(a,b)], Philipp Espeter[(a,b)], Peter Roese[(a,b)], Ulf Berges[(a,b)], Carsten Westphal[(a,b)]
[(a)] Experimentelle Physik 1, Technische Universität Dortmund, Germany
[(b)] DELTA, Technische Universität Dortmund, Germany

Copper is a transition metal located in the first subgroup of the periodic system with the serial number 29. The crystalline structure is face-centered cubic (fcc). Cobalt is a ferromagnetic transition metal located in the eighth subgroup of the periodic system with the serial number 27. The growth of epitaxial thin films of ferromagnetic materials on non-magnetic substrates under ultrahigh vacuum conditions has long been of interest. It offers the possibility that may exhibit new properties of a high technological interest. These layered structures may possibly find application in magnetic recordings [4]. Therefore, it is in focus of present research. The reconstruction of Cu(100) is a (1x1). Furthermore, the Co films will grow in a metastable structure which closely follows that of the Cu substrate rather than the Co bulk equilibrium phase. Thereby, the Co thickness is important, because a thickness greater than 8 ML Co forms a vertical contraction, i.e. it grows tetragonal distorted. This behavior has been reported under room temperature [1,2]. The multi-layer system Co/Cu(100) has already structurally [1, 2], electronically [3,5] and magnetically [4] studied.

This work focuses the 3p peak of Co and Cu structure. We report on a synchrotron radiation based study of Co/Cu(100) means of x-ray photoelectron spectroscopy (XPS). The experiments were performed at the U55 beamline 11 at DELTA. In Figure 1 the high resolution XPS spectrums of Cu 3p for a polar angle of Θ = 0° is displayed. The spectrum on the left side can be fitted with two peaks referring to substrate (C1) and surface (C2). The other spectrum can be fitted with one peak referring to substrate (C1). The C2 peak was left out because of its small high and influence of the fit.

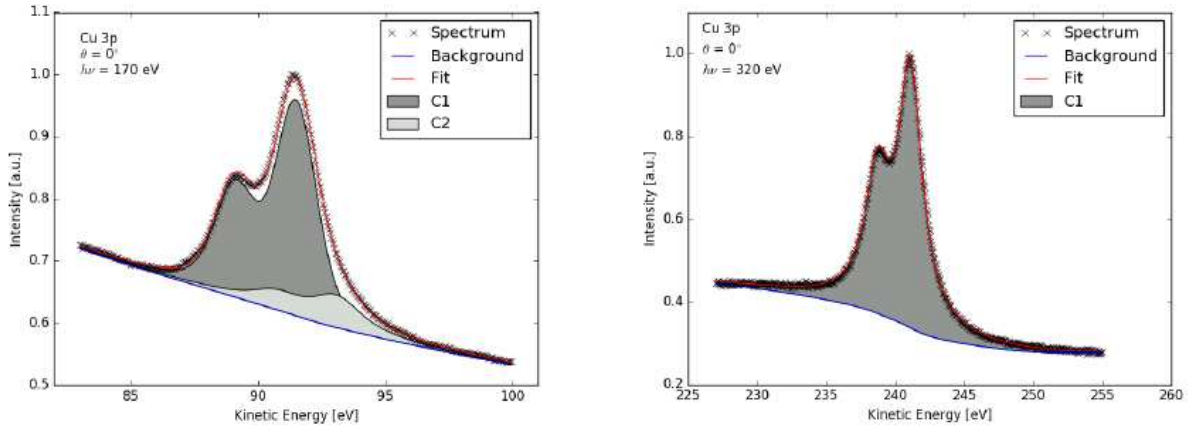

Figure 1: Cu 3p high resolution XPS spectrum by using a photon energy of hv = 170 eV (left) and by using a photon energy of hv = 320 eV (right).

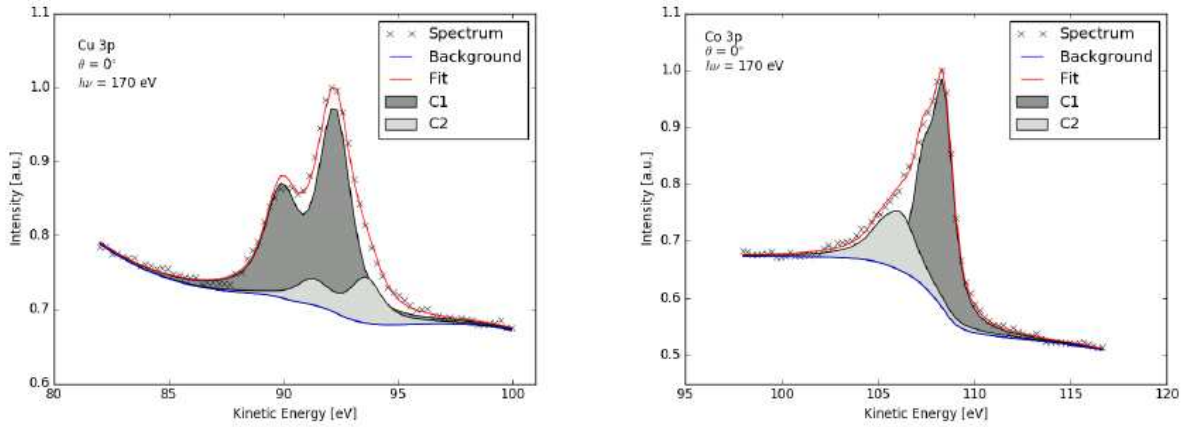

Figure 2: High resolution XPS spectrum of Co/Cu(100) for Cu 3p (left) and Co 3p (right).

The height of the C2 component changes depending on the photon energy and is stronger for surface sensitive measurements. In Figure 2 the high resolution XPS spectrum of Co/Cu(100) for a polar angle of Θ = 0° is shown. The spectrum on the left side is the Cu 3p peak and on the right the Co 3p peak, both spectra can be fitted with two components. The components are the same as before: substrate (C1) and surface (C2). The components in the Co/Cu spectra do not correspond directly to the components in the Cu spectrum, because they were recorded with different pass energies, i.e. an energy shift exists. Therefore, new measurements will be carried out.

References

[1] A. Clarke, G. Jennings, R. F. Willis, P. J. Rous and J. B. Pendry, *A LEED determination of the structure of cobalt overlayers grown on a single-crystal Cu(001) substrate*, Surface Science **187** (1987).

[2] J. R. Cerda, P. L. de Andres, A. Cebollada, R. Miranda, E. Navas, P. Schuster, C. M. Schneider and J. Kirschner, *Epitaxial growth of cobalt films on Cu(100): a crystallographic LEED determination*, Journal of Physics: Condensed Matter **5** (1993).

[3] R. Pentcheva and M. Scheffler, *Stable and metastable structures of Co on Cu(001): A ab intitio study*, Physical Review B **61** (2000).

[4] C. M. Schneider, P. Bressler, P. Schuster, J. Kirschner, J. J. de Miguel, R. Miranda and S. Ferrer, *Epitaxy and magnetic properties off cc cobalt films on Cu(100)*, Vacuum **41** (1990).

[5] J. Rajeswari, H. Illbach, C. M. Schneider, A. T. Coasta, D. L. R. Santos and D. L. Mills, *Surface spin waves of fcc cobalt films on Cu(100): High-resolution spectra and comparison to theory*, Physical Review B **86** (2012).

Acknowledgement

We would like to thank the DELTA machine group for providing synchrotron radiation.

XPS/XPD measurements of self-assembled caffeine monolayers on Ag(110)

P. Roese[1,2,*], P. Espeter[1,2], K. Shamout[1,2], U. Berges[1,2], C. Westphal[1,2]

[1] Experimentelle Physik I - Technische Universität Dortmund, Otto-Hahn-Str. 4a, D-44221 Dortmund

[2] DELTA - Technische Universität Dortmund, Maria-Goeppert-Mayer-Str. 2, D-44221 Dortmund

[*] corresponding author: peter.roese@tu-dortmund.de

In the last years there has been progress in the self-assembly of organic compounds on different surfaces. Beside the exact knowledge of the electronic and chemical properties of such systems, the structural information is of great interest. In this context polymorphism of organic compounds plays an important role in their electronic properties [1, 2] or bio-availability [3]. An example for such a molecule is caffeine. A schematic drawing of the molecule is shown in figure 1 on the left hand side. A few publications analyzed the growth of caffeine on different substrates, but they always used multilayers of caffeine on non-metallic substrates [4, 5, 6, 7, 8]. Therefore, we analyzed a monolayer of caffeine on an Ag(110) crystal surface. Because of it's flat, well reconstructed and inert surface, no strong molecule-surface interaction influences the molecule-molecule interaction during deposition.

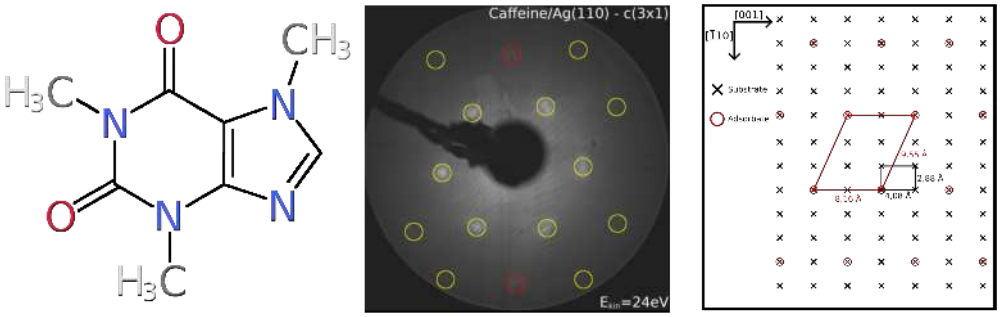

Figure 1: Left: Schematic drawing of the caffeine structure. Center: LEED image of Caffeine on Ag(110) recorded at $E_{\mathrm{kin}} = 24$ eV. Substrate spots are marked with red circles and adsorbate spots are marked with yellow circles, respectively. Right: Drawing of the corresponding structure in real space. The unit cell of the substrate is marked with a black rectangle and the caffeine unit cell is marked with a red parallelogram.

In the first step of this work one monolayer of caffeine molecules was evaporated from a commercial knudsen cell at a temperature of 120°C for five minutes onto a clean Ag(110) surface. In the center of figure 1 the corresponding LEED image at $E_{\mathrm{kin}} = 24$ eV is shown. The substrate spots and the new adsorbate spots of the caffeine superstructure are marked with red and yellow circles, respectively. The caffeine molecules form a c(3x1) superstructure on top of the silver surface, which is clearly shown in the corresponding schematic view of the real space on the right hand side of figure 1. The unit cell of the caffeine superstructure is marked with a red parallelogram. The length of the unit cell vectors leads to the conclusion that the unit cell consists of only one molecule.

With the knowledge about the long range order of the caffeine superstructure on the surface, XPS and XPD are used to determine the local order and chemical structure. Ag 3d high resolution spectra after the adsorption of caffeine molecules (not shown here) doesn't

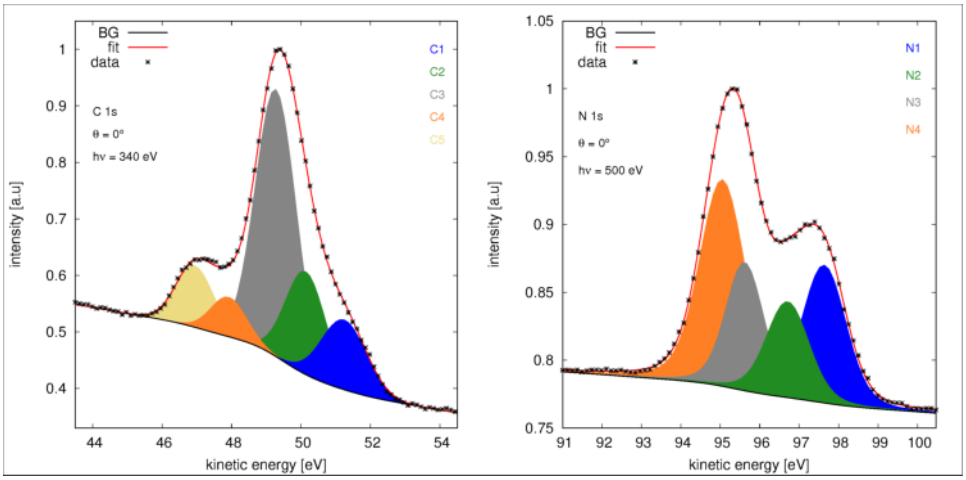

Figure 2: Left: C 1s XPS spectrum of caffeine using a photon energy of $E_{\mathrm{hv}} = 340$ eV and a polar angel of $\Theta = 0°$. Right: N 1s XPS spectrum of caffeine using a photon energy of $E_{\mathrm{hv}} = 500$ eV and a polar angel of $\Theta = 0°$. The signals are fitted with five and four Voigt-like components, respectively.

show any additional peaks or shoulders in the line shape of the signal compared to the spectrum of clean Ag(110). This is an evidence for a missing bonding between the molecules and the surface. In the next step high resolution spectra of carbon 1s, nitrogen 1s, and oxygen 1s were recorded. The C 1s and N 1s XPS spectra, shown in figure 2, were recorded at photon energies of $E_{\mathrm{hv}} = 340$ eV and $E_{\mathrm{hv}} = 500$ eV, respectively. The C 1s signal can be fitted with five and the N 1s signal with four Voigt-like components. Within each spectrum, all peaks have the same line shape. The fit parameters for both spectra are in good accordance to literature values for caffeine measured in the gas phase [9]. One can conclude that on the one hand the molecules have been non-destructive adsorbed onto the surface and on the other hand no additional, unexplainable component is visible. The last point is another evidence for the missing bonding between the surface and the molecules.

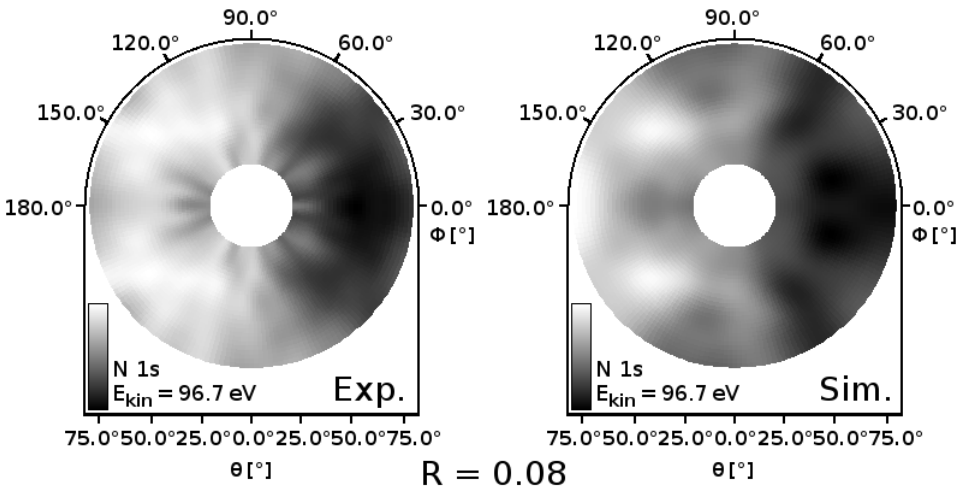

Figure 3: Left: Measured XPD pattern of the N 1s orbital of Caffeine on Ag(110). Right: Simulated XPD pattern of the best fitting structure model. The R-factor of 0.08 shows good accordance between the recorded and simulated pattern.

A XPD pattern of the N 1s orbital has been recorded to determine local order as well as the orientation of the caffeine molecules regarding to the surface. The measured XPD pattern and the simulated XPD pattern with the best R-factor are shown in figure 3. We achieved a good match between the measured and simulated pattern, proved by a R-factor of 0.08. The resulting structure is shown in figure 4. On the left hand side the structure is shown in top view. It is clearly visible, that the unit cell (marked as a parallelogram in red) only contains of one molecule. The size and shape of the unit cell is in perfect accordance to the LEED results shown in figure 1. The side view of the best simulated structure is shown on the right hand side of figure 4. Two interesting facts can be concluded from this view. First, the molecules are not flat lying on the surface and they are slightly tilted by 33.8°. Second, there is a very large distance of 2.59 $\mathring{A}$ between the molecules and the surface. This is a further evidence for the missing bonding between the surface and the molecules.

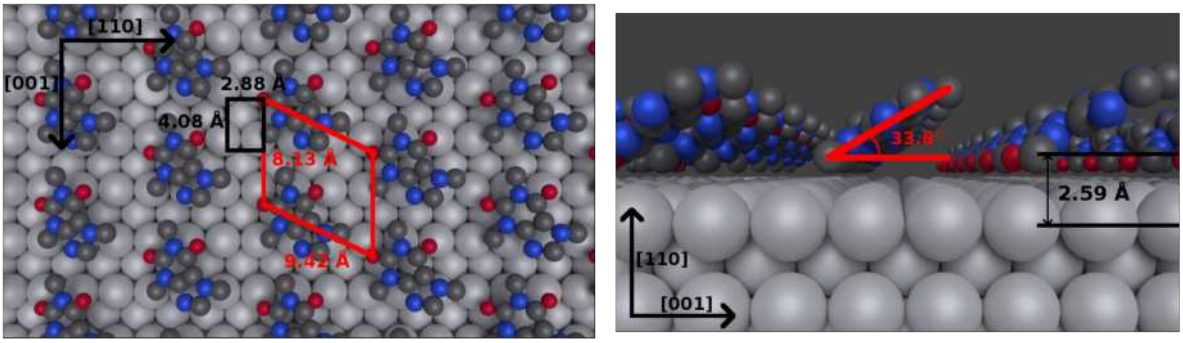

Figure 4: Resulting structure from the XPD simulation shown in figure 3. Left: Top view. The unit cell of the superstrucutre is marked in red. Right: Side view. The tilt of the molecules as well as the large substrate-adsorbate distance is visible.

References

[1] A. O. F. Jones et al., *ACS Appl. Mater. Interfaces* **7**, 1868 (2015).
[2] H. Wang et al., *Org. Electron.* **15**, 1586 (2014).
[3] D. Singhal et al., *Adv. Drug Delivery Rev.* **56**, 335 (2004).
[4] A. Safraz et al., *Cryst. Growth Des.* **12**, 583 (2012).
[5] O. Werzer et al., *Cryst. Growth Des.* **13**, 1322 (2013).
[6] J. Leiterer et al., *Langmuir* **24**, 7970 (2008).
[7] C. Röthel et al., *Cryst. Growth Des.* **15**, 4563 (2015).
[8] C. Röthel et al., *CrystEngComm* **19**, 2936 (2017).
[9] O. Plekan et al., *J. Phys. Chem. A* **116**, 5653 (2012).

Pentamer chain of silicon nano-ribbons

P. Espeter[1,2,*], C. Keutner[1,2], P. Roese[1,2],K. Shamout[1,2], U. Berges[1,2], and C. Westphal[1,2]

[1] Experimentelle Physik I - Technische Universität Dortmund, Otto-Hahn-Str. 4, D-44227 Dortmund

[2] DELTA - Technische Universität Dortmund, Maria-Goeppert-Mayer-Str. 2, D-44227 Dortmund

[*] corresponding author: philipp.espeter@tu-dortmund.de

The first compelling evidence for two-dimensional silicene on Ag(111) [1] substrate raised interest in further low-dimensional structures built from silicon atoms. The one-dimensional representative is called silicon nano-ribbon and is reported to grow on a (1×1)-reconstructed Ag(110) surface [2]. They grow perfectly aligned along the $[\bar{1}10]$ direction with all nano-ribbons having the same height of 2 Å and the same width of 16 Å. Still, the internal structure is under debate [3]. Further, these nano-ribbons are assumed to open manyfold applications in electronic circuits and spin based devices [4]. The metallic substrate is unsuitable for the assembling of electronic devices, and thus the nano-ribbons need to be transferred from the metallic silver substrate to an insulating substrate. For the development of an transfer process the understanding of the interaction between the substrate and the nano-ribbons is of utmost importance. This study provides an encompassing approach to determine the substrate-adsorbate interaction and the local order within the silicon nano-ribbons. Surface-sensitive X-ray photoelectron spectroscopy (XPS) and diffraction (XPD) are utilized to analyze the interaction and to evaluate several structure models, respectively [5].

The XPS spectra of the Ag 3d core-level recorded at a polar angle of $\Theta = 60°$ before and after growth of silicon nanoribbons are shown in figure 1. The signals corresponding to

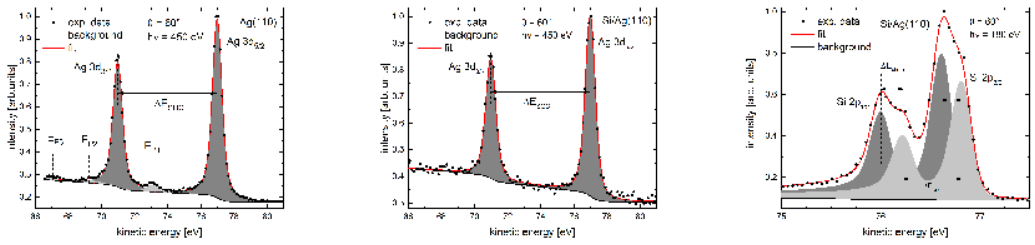

Figure 1: High-resolution XPS spectra of Ag 3d core-level before (left) and after (middle) the growth of silicon nano-ribbons. High-resolution XPS spectrum of the Si 2p core-level after the growth of the nano-ribbons (right).

three surface plasmons vanish after the growth of silicon nano-ribbons. The shape of the Ag 3d core-level itself remains unchanged. Thus, it is concluded that there is only a very weak interaction between the silver substrate and the silicon nano-ribbons.

The XPS spectrum of the Si 2p core-level signal is shown in figure 1. The Si 2p core-level signal is composed of two chemically shifted components C1 and C2 printed in light grey and dark grey, respectively. Thus, the existence of two different chemical environments of the silicon atoms can be deduced. Two XPD pattern of the Si 2p core-level signal

at incoming photon energies of $h\nu = 140\,\mathrm{eV}$ and $h\nu = 180\,\mathrm{eV}$ have been recorded and are shown in reference [5]. The evaluation of more than 30 different proposed structure models revealed that none of the proposed structure models fit to the experimental data. We present an improved structure model that perfectly matches the experimental data. The local order of the nano-ribbons can be described by a pentamer chain with two missing rows. The height and width of the pentamer chain are determined to be 2.3 Å and 15.9 Å, respectively. The large distance of 1.91Å between the pentamer chain and the silver substrate supports the conclusion of a weak interaction as deduced from the Ag 3d core-level XPS spectra. Further, silicon atoms with two chemically different environments can be identified. From a deconvolving procedure of the XPD pattern it was possible to assign the origin of the two distinct chemically shifted XPS components to the distinct silicon atoms. The silicon atoms colored in pure yellow are neighboured by three silicon atoms and correspond to the component C2. The silicon atoms colored with a black wireframe are neighboured by two silicon atoms and correspond to the component C1.
These results provide a precise framework for reliable predictions of theoretical approaches and further, enhance the interest in transferring silicon nano-ribbons from metallic to insulating substrates.

References

[1] P. Vogt, P. De Padova, C. Quaresima, J. Avila, E. Frantzeskakis, M. C. Asensio, A. Resta, B. Ealet and G. Le Lay, *Silicene: Compelling Experimental Evidence for Graphenelike Two-Dimensional Silicon*, Physical Review Letters **108**, 155501 (2012).

[2] C. Leandri, G. L. Lay, B. Aufray, C. Girardeaux, J. Avila, M. Dávila, M. Asensio, C. Ottaviani and A. Cricenti, *Self-aligned silicon quantum wires on Ag(110)*, Surface Science **574**, L9 (2005).

[3] B. Aufray, B. Ealet, H. Jamgotchian, J.-H. Hoarau, J.-P. Biberian and H. Maradj, Growth of Silico Nano-ribbons on Ag(110): State of the Art, in *Silicene: Structure, Properties and Applications*, pages 183–202, Springer, Switzerland, 1st edition, 2016.

[4] J. I. Cerdá, J. Sławińska, G. L. Lay, A. C. Marele, J. M. Gómez-Rodríguez and M. E. Dávila, *Unveiling the pentagonal nature of perfectly aligned single-and double-strand Si nano-ribbons on Ag(110)*, Nature Communications **7**, 13076 (2016).

[5] P. Espeter, C. Keutner, P. Roese, K. Shamout, U. Berges and C. Westphal, *Facing the interaction of absorbed silicon nano-ribbons on silver*, Nanotechnology **28**, 455701 (2017).

Photoemission study of the intercalation of cobalt underneath graphene on silicon carbide

R. Hönig[1,2,*], P. Espeter[1,2], P. Roese[1,2], K. Shamout[1,2], U. Berges[1,2], and C. Westphal[1,2]

[1] Experimentelle Physik I - Technische Universität Dortmund, Otto-Hahn-Str. 4a, D-44221 Dortmund

[2] DELTA - Technische Universität Dortmund, Maria-Goeppert-Mayer-Str. 2, D-44221 Dortmund

[*] corresponding author: richard.hoenig@tu-dortmund.de

The interface between graphene and ferromagnetic elements is of special interest because of its relevance for spintronics [1]. In order to realize this interface, cobalt is a highly suitable candidate due to its almost perfect lattice match with graphene [2]. In this work we use graphene on silicon carbide (SiC) as substrate and prepare the graphene/ferromagnet interface using the intercalation of deposited cobalt films by thermal annealing. In order to determine the chemical state of the sample before and after the intercalation, photoelectron spectroscopy is applied. For the interpretation of the photoelectron spectra it is worth to mention that graphene growth on the Si-terminated (0001) crystal face of hexagonal SiC is accompanied with the formation of a covalently bonded so-called bufferlayer due to the lattice mismatch between graphene and SiC [3]. We previously analyzed the atomic structure of this bufferlayer by means of photoelectron diffraction [4]. In this work we focus on the chemical state of intercalated bufferlayer samples instead of the atomic structure.

In figure 1 (left) the C 1s photoelectron spectrum of a reference sample without deposited Co is shown. A minimum of four components is necessary to fit the spectrum. The components S1 and S2 refer to the bufferlayer, the component G is the graphene component and SiC is the SiC-bulk signal [5]. From this spectrum and from complementary measurements by means of photoemission electron microscopy we conclude that most of the sample surface is covered with bufferlayer whereas only smalls parts consist of monolayer graphene. In figure 1 (right) the C 1s spectrum of an *ex-situ* intercalated sample is shown. The amount of Co deposited is 3 nm and the intercalation was triggered by annealing at 360 °C. The C 1s spectrum of this sample consists of only one component which is characteristic for monolayer graphene. Thus, it can be concluded that the bufferlayer was fully converted into graphene on this sample. The substrate component is completely suppressed due to the high amount of intercalated cobalt.

During the intercalation of graphene on SiC the bufferlayer is often decoupled by the substitution of the Si-C bonding with a bonding of Si and the intercalant [6]. Thus, we analyzed the Si 2p photoelectron spectrum to determine the chemical state of the Si atoms. A reduced amount of 0.5 nm cobalt was evaporated onto the sample *in-situ* and intercalation was triggered by annealing at 650 °C. In figure 2 (left) the Si 2p spectrum before the intercalation is shown. This spectrum is consistent with reference spectra reported in the literature [5]. The main component refers to the bulk Si-C bonding whereas the minor component is related to the bufferlayer Si-C bonding. In figure 2 (right) the Si 2p spectrum after intercalation is shown. An additional component is clearly visible in the spectrum. The binding energy of the new peak was referenced to the binding energy of the bulk SiC peak and is consistent with the binding energy of Si 2p peaks in cobalt silicide compounds [7]. Due to the small amount of evaporated cobalt, the bufferlayer component has not totally vanished yet.

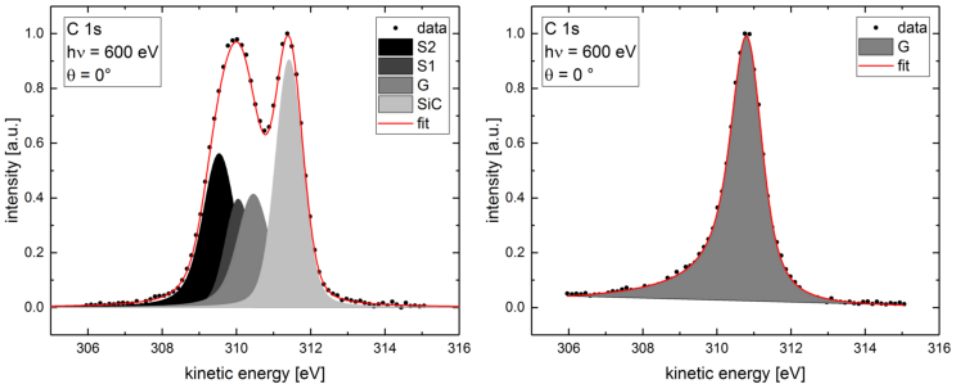

Figure 1: Left: C 1s photoelectron spectrum of a reference sample. Right: C 1s photoelectron spectrum after *ex-situ* intercalation of Co.

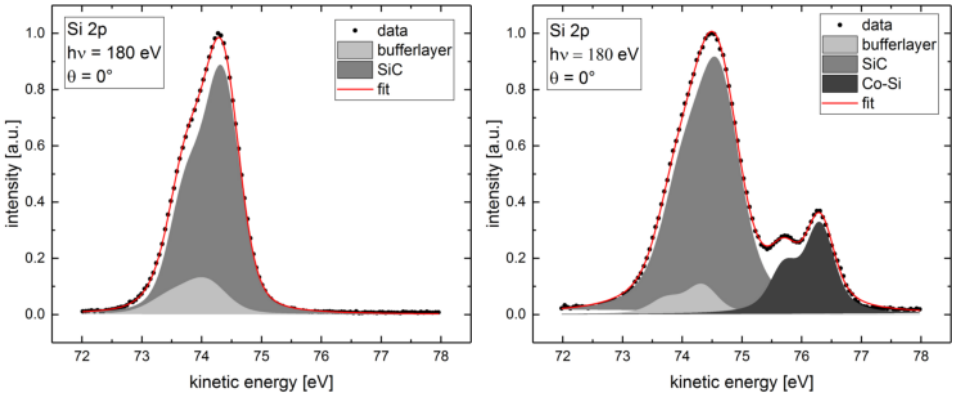

Figure 2: Left: Si 2p photoelectron spectrum recorded before intercalation of Co. Right: Si 2p photoelectron spectrum after *in-situ* intercalation of Co.

In this work we analyzed the C 1s and the Si 2p photoelectron spectra of graphene on silicon carbide before and after intercalation of cobalt. It is concluded that the covalently bonded bufferlayer is decoupled and transformed into a graphene layer. Furthermore, the Si 2p spectrum reveals the formation of cobalt silicide. These preparatory results are of high value for further studies on this sample system regarding its magnetic properties.

Acknowledgement

We would like to thank the DELTA-staff for their support.

References

[1] W. Han, R. K. Kawakami, M. Gmitra and J. Fabian, *Nat. Nanotech.* **9**, 794 (2014).

[2] V. M. Karpan, P. A. Khomyakov, A. A. Starikov, G. Giovannetti, M. Zwierzycki, M. Talanana, G. Brocks, J. van den Brink and P. J. Kelly, *Phys. Rev. B* **78**, 195419 (2008).

[3] K. V. Emtsev, F. Speck, Th. Seyller, L. Ley, and J. D. Riley, *Phys. Rev. B* **77**, 155303 (2008).

[4] L. H. de Lima, D. Handschak, F. Schönbohm, R. Landers, C. Westphal and A. de Siervo, *Chem. Commun.* **50**, 13571 (2014).

[5] C. Riedl, C. Coletti and U. Starke, *J. Phys. D: Appl. Phys.* **43**, 374009 (2010).

[6] C. Riedl, C. Coletti, T. Iwasaki, A. A. Zakharov, and U. Starke, *Phys. Rev. Lett.* **103**, 246804 (2009).

[7] G. Rangelov, T. Fauster, *Surf. Sci.* **365**, 403 (1996).

Interface sensitive structure determination of MgO/Co/GaAs(001) using photoelectron diffraction (XPD)

Karim Shamout[(a,b)], Philipp Espeter[(a,b)], Peter Roese[(a,b)], Ulf Berges[(a,b)], Carsten Westphal[(a,b)]
[(a)] Experimentelle Physik 1, Technische Universität Dortmund, Germany
[(b)] DELTA, Technische Universität Dortmund, Germany

We present a detailed investigation on the MgO/Co(bcc)/GaAs multi-layer system as a representative for insulator(IN)/ferromagnet(FM)/semiconductor(SM) systems since it can combine both, an IN/FM interface and a FM/SM interface. The first system is important for the understanding of the tunneling magnetoresistance effect (TMR). In FM/IN/FM systems, electrons can tunnel through a thin insulator layer, depending on the magnetization of the ferromagnets [1]. The second one is widely used in scope of quantum well detectors to detect the spin-polarization of tunnelled electrons [2]. We investigate this hybrid system with x-ray photoelectron spectroscopy and diffraction in order to identify its chemical and structural properties.
As a results, we present a formed Co_3Ga compound at the interface of Co(bcc)/GaAs in a rare $D0_3$ structure. The corresponding experimental XPD data and simulation are shown in Fig. 1. The resulting structure is also referred to as pseudo-Heusler alloy. We provide precise lattice sites for this structure, as shown in Fig. 3. The Co_3Ga lattice constant of 5.65 Å in [100] and [010] direction perfectly matches to the GaAs(001) bulk lattice constant. The simulation results in a lifted GaAs surface reconstruction beneath the Co(bcc) film.

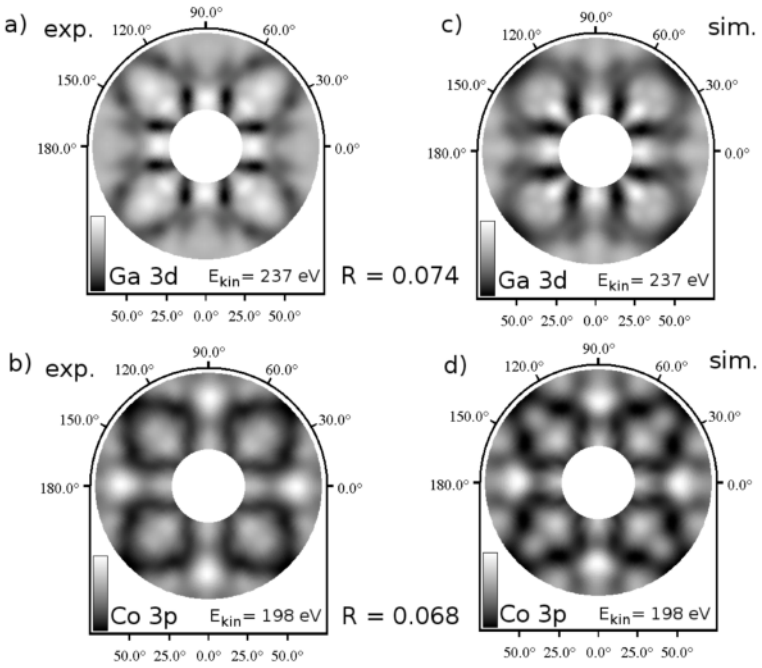

Figure 1: Measured Ga 3d (a) and Co 3p (b) XPD pattern for the Co/GaAs system at E_{Ph}=260 eV and the corresponding simulations (c) and (d). R-factors of 0.074 and 0.068 indicate a perfect match between experiment and simulation, respectively.

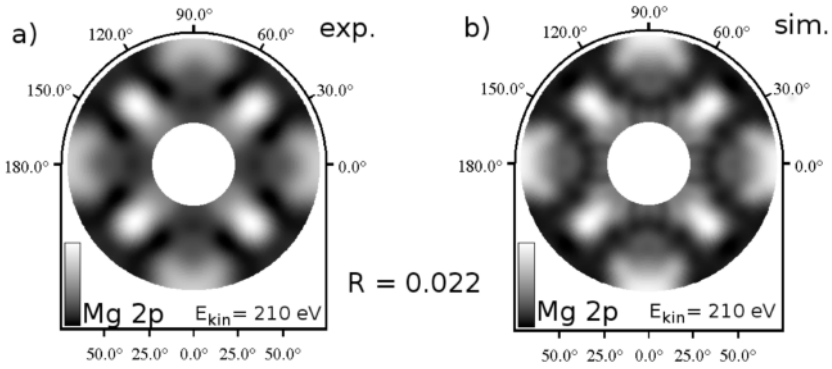

Figure 2: Measured Mg 2p XPD pattern (a) for the MgO/Co/GaAs system at E_{Ph}=260 eV and the corresponding simulation (b). An R-factor of 0.022 indicates a perfect match between experiment and simulation.

For the MgO/Co(bcc) interface, we observe only a weak bond between MgO and Co, but also a distorted MgO unit cell. The corresponding experimental XPD data and simulation is shown in Fig. 2. Moreover, there is a critical amount of MgO necessary to grow a crystalline MgO film. Again, we provide precise lattice sites for this interface, as shown in Fig. 3. A thickness below 4 ML results in an amorphous layer. At 5 ML, the MgO layer contains two epitaxially grown unit cells.

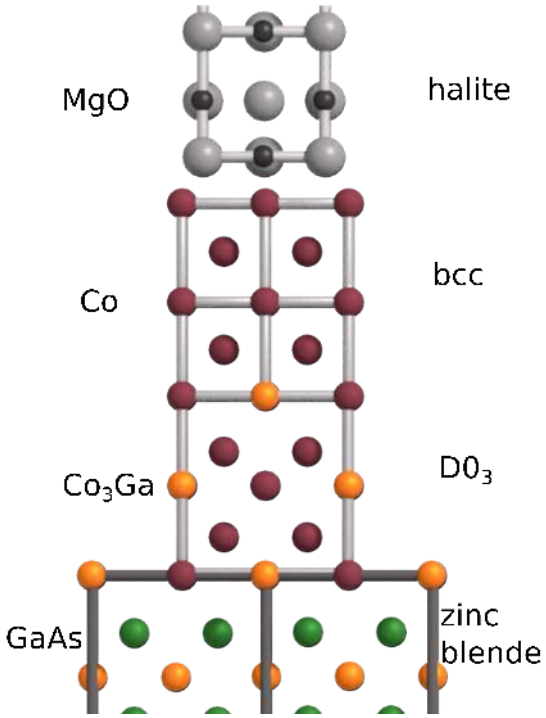

Figure 3: Resulting structure for the Co/GaAs interface after 12 ML of Co deposition and the MgO/Co interface after 5 ML of MgO deposition. For the first interface, a Co_3Ga alloy in $D0_3$ structure is formed. The Co(bcc) grows on this alloy in a heavily distorted structure. For the second interface, MgO is amorphous for a thickness below 4 ML. At 5 ML, it crystallizes in a compressed halite structure.

In all, with this work we address a broad readership that is interested in magnetic- and spin-focused materials from an experimental and theoretical point of view. With the provided lattice sites, new calculations [3] can be performed in order to match the measured TMR ratios [4] with the predicted ones and the discovery of the Co_3Ga alloy in $D0_3$ structure raises questions regarding its magnetic properties.

References: [1] C.-F. Pai, M.-H. Nguyen, C. Belvin, L. H. Vilela-Leão, D. C. Ralph, and R. A. Buhrman, Appl. Phys. Lett. 104, 082407 (2014)
[2] X. Jiang, R. Wang, R. M. Shelby, R. M. Macfarlane, S. R. Bank, J. S. Harris, and S. S. P. Parkin, Phys. Rev. Lett. 94, 056601 (2005)
[3] S. Mallik, S. Mallick, and S. Bedanta, J. Magn. Magn. Mater. 428, 50 (2017)
[4] S. Yuasa, T. Katayama, T. Nagahama, A. Fukushima, H. Kubota, Y. Suzuki, and K. Ando, Appl. Phys. Lett. 87, 222508 (2005)

X-ray Scattering

X-ray diffraction from the side planes of core-shell nanowires

A. AlHassan, D. Bahrami, U. Pietsch, University of Siegen.

R. Lewis, H. Küpers, L. Geelhaar, PDI-Berlin.

The strain field within GaAs/(In,Ga)As core-shell nanowires (NW) has been investigated by means of X-ray diffraction (XRD) at beamline 9 of DELTA. Diameter and thickness of the GaAs core and (In,Ga)As shell were kept constant, whereas the nominal indium content was varied between 20% and 60%. The onset of strain relaxation of the sample series has already been investigated [1] by XRD along the [111] NW growth axis. In that study, plastic strain relaxation was observed beyond an indium content of 40%. For interpretation of data Lewis et al. proposed a new scenario for strain relaxation, considering a part of (In,Ga)As NW shell stays coherently strained accompanied by plastically relaxed mounds grown onto the GaAs NW sidewalls. Nevertheless, the complex strain state of core-shell NWs is encoded along directions perpendicular to the growth axis. Therefore, we performed a strain investigation at the same samples series measuring along directions perpendicular to the NW hexagonal side facets and edges. In particular, we recorded 2D reciprocal space maps (RSM) in vicinity of the radial (2-20) and (22-4) Bragg reflections (see Figure below). As seen below, up to an indium content of 40%, the Bragg peak corresponding to the (In,Ga)As shell splits into 3 sub-peaks indicating elastic strain along the scanned direction (marked by B) and at neighboring facets (marked by A) inclined by 60° with respect to the scan direction. Similar behavior up to 40% Indium is found at (22-4), i.e. along the NW edges. The absence of peaks A for 50% and 60% indium indicates the onset of plastic relaxation following the scenario mentioned above. The data are interpreted in terms of an approach published in [2]. However, extensive calculations and qualitative interpretation of the details of relaxation mechanism are underway.

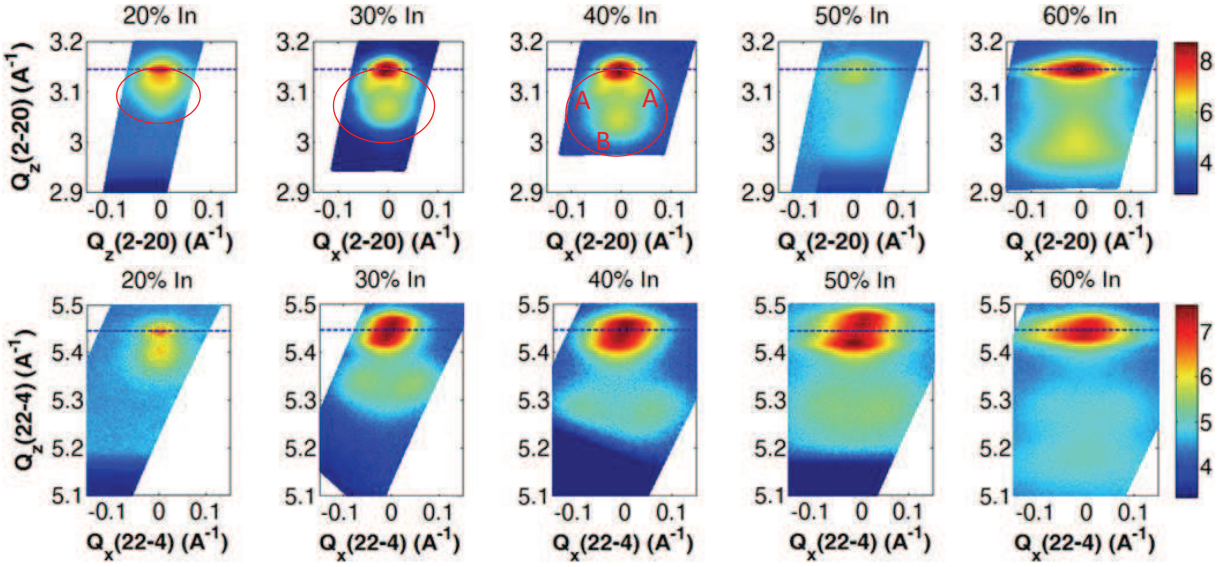

[1] R. B. Lewis, L. Nicolai, H. Küpers, M. Ramsteiner, A. Trampert, and L. Geelhaar, Nano Lett., 17, 136-142, (2017).
[2] A.AlHassan et al. Phys.Rev Materials (2017) under review

DELTA user report 2017
Proposer: Prof. Dr.-Ing. A. Ludwig
Co-Proposers: P. Decker, T. Oellers, D. Grochla, L. Banko, D. Naujoks, S. Salomon

Investigation of texture in Al-Cr-N thin films using synchrotron GI- XRD

L. Banko
Werkstoffe der Mikrotechnik, Institut für Werkstoffe, Fäkultät Maschinenbau
Ruhr-Universität Bochum, D-44801 Bochum

Five Al-Cr-N thin film samples were synthesized in an industrial type sputter chamber (*CC800/9 custom, CemeCon AG, Würselen*) at IOT Aachen (*Institut für Oberflächentechnik, RWTH Aachen*). All depositions were carried out at 350°C and the frequency of the HiPIMS discharge was set to 300, 500, 700, 1000 and 2000 Hz respectively with a constant 40 µs pulse length. For the correlation of plasma properties during synthesis and thin film properties, the samples were characterized by means of GI-XRD at BL 9 using a mar345 image plate detector with an energy of 20 keV at an incidence angle of Θ = 3°.

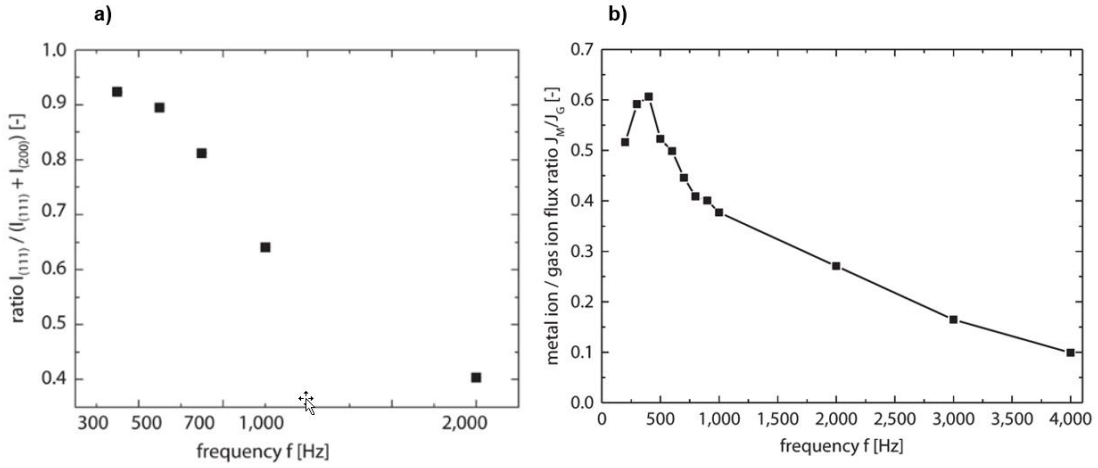

***Figure 1**: a) Texture coefficient as a function of frequency, b) metal ion to gas ion ratio as a function of frequency.*

The analysis of the GI-XRD diffraction patterns showed, that all analyzed films exhibit the fcc-CrN crystal structure. The ratio of the (111) diffraction signal and the (200) diffraction signal after azimuthal integration was calculated and used as a measure for the texture in the thin film (Figure 1 a). It was found, that the preferred growth orientation of the crystallites in the thin films varies from strong (111) texture for processes near 300 Hz to a more random distribution at 2000 Hz. Correlations were found between the texture and the metal ion to gas ion ratio during growth (Figure 1 b). The results show that a change in the ratio of the bombarding species influences the growth mode during film synthesis and results in differently textured films. The results were recently published [1].

This research is part of collaborative research within the SFB-TR 87 funded by DFG.

References

[1] K. Bobzin, T. Brögelmann, N. C. Kruppe, M. Engels, A. von Keudell, A. Hecimovic, A. Ludwig, D. Grochla, L. Banko, Fundamental study of an industrial reactive HPPMS (Cr,Al)N process, Journal of Applied Physics 122, 015302 (2017)

In-situ examination of Cr-Ni steel surfaces heat treated under N_2 by GIXRD

D. Wulff[a], B. Bornmann[b], R. Wagner[b], U. Holländer[a], D. Lützenkirchen-Hecht[b], K. Möhwald[a], R. Frahm[b], H.J. Maier[a]

a) Institut für Werkstoffkunde, Leibniz Universität Hannover, An der Universität 2, 30823 Garbsen
b) Fakultät 4 - Physik, Bergische Universität Wuppertal, Gaußstr. 20, 42097 Wuppertal

Introduction

The oxidation of different steels under air or oxygen at high temperatures has been analyzed intensively [1]. Around brazing technology the joining of components made of Cr-Ni steel is conducted under vacuum or inert gas atmospheres at temperatures above 900 °C. Especially inert gas processes in conveyor belt furnaces are likely used for the mass production because of their cost efficiency. The gas atmospheres normally consist of a carrier gas (N_2 or Ar) and a reducing agent. The reducing agent is necessary to achieve a low residual oxygen partial pressure in the atmosphere so that native oxides are reduced and an oxidation of the workpiece surface is avoided. Nevertheless only few publications deal with the oxidation of Cr-Ni steel surfaces under N_2 atmosphere [2, 3]. A deeper understanding, especially of the temperature dependent interactions between surface and process atmosphere, is thus necessary for a further development of brazing processes.

For the measurements circular stainless steel samples were used with a nominal composition of 64% Fe, 19.5% Cr, 8.6% Ni, 2% Mn, 0.9% Cu, 0.4% Si, 0.3% Mo in wt.-% and minor traces (< 0.03%) of Ti, V, P, C and S. The samples were polished to a final grading of 3 µm by diamond suspensions before the measurements to ensure reproducible starting conditions.

The in-situ GIXRD measurements were performed at BL 10 by using a high temperature heater cell [4] and a PILATUS 100K detector. The data were collected at an energy of 10 keV and a detector threshold of 8.5 keV at different temperature levels from 30 °C up to 1045 °C. The rates of heating are listed in Tab. 1. When the sample reached the measuring temperature it was aligned again to compensate the thermal expansion. At every temperature level a sequence of 12 single patterns (three incidence angles 1 °, 2 ° and 4 ° and four diffraction angles 25 °, 32.5 °, 40 ° and 48 °) were taken. A good data quality could be achieved by an integration time of 30 s per pattern.

Table 1: Rates of heating

start temperature	measuring temperature	rate of heating
30 °C	400 °C	50 °C/h
400 °C	600 °C	50 °C/h
600 °C	800 °C	30 °C/h
800 °C	900 °C	25 °C/h
900 °C	1045 °C	8 °C/h

Results

In Fig. 1, GIXRD patterns of the sample collected at an incident angle of Θ = 2 ° for the different temperature levels are presented. The patterns of the sample at room temperature show four reflexes. The reflexes at 34.9 ° (♥1) and 40.4 ° (♥2) can be clearly assigned to γ-Fe. The third and fourth reflexes belong to α-Fe or martensite (♣1& ♣2) and get less intensive when the incident angle is increased. It can be assumed that α-Fe or martensite has formed near the surface. Up to 400 °C no significant crystallographic changes can be detected except a slight shift of the peak positions induced by the thermal expansion of the lattice. With higher measuring temperature an increasing shift of these Bragg peaks take place.

At 600 °C the first three additional reflexes are observed at 26.8 ° (♦1), 43.3 ° (♦2) and 19.6 ° (♦3). These reflexes belong to Cr_2O_3 and have very small intensities but can be clearly separated from the background. With increasing incident angle these oxide reflexes get less intensive, so the oxide has formatted on top of the ground material. A couple more new reflexes are detected at 800 °C (28.1 ° (♠1), 24.0 ° (♠2), 49.0 ° (♠3), 44.7 ° (♠4), 29.4 ° (♠5) and 42.0 ° (♠6)). All of these reflexes can be assigned to Fe_3O_4 or γ-Fe_2O_3.

It is recognizable that at 800 °C the main iron oxide reflex is already more intensive than the Cr_2O_3 main reflex although its intensity increased with the higher temperature as well. Also notable is that the α-Fe or martensite reflexes (♣1 & ♣2) are missing at 800 °C and higher temperatures.

With rising temperature up to 900 °C the intensities of all reflexes of the oxide species are also increasing. So more Cr_2O_3 reflexes got visible: 28.8 ° (♦4), 31.6 ° (♦5), and 33.0 ° (♦6). When the measurements at an incident angle of 1 ° are compared with the results obtained at 2 ° it can be seen that the intensity levels of the oxide species changes. So the intensities of Cr_2O_3 gained with increasing incident angle compared to the intensities of the Fe_3O_4/γ-Fe_2O_3 reflexes. It can be concluded that a layer system grew with a covering layer rich of iron oxide and an interlayer richer of Cr_2O_3. At 1045 °C the intensities of the oxide reflexes have grown further and two Cr_2O_3 (49.8 ° (♦7) and 45.9 ° (♦8)) and one last Fe_3O_4/γ-Fe_2O_3 reflex (51.0 °(♠7)) occurred in addition. The up growth behaviors of the different oxides seem not to differ because the intensities of the reflexes of both species increased almost equally.

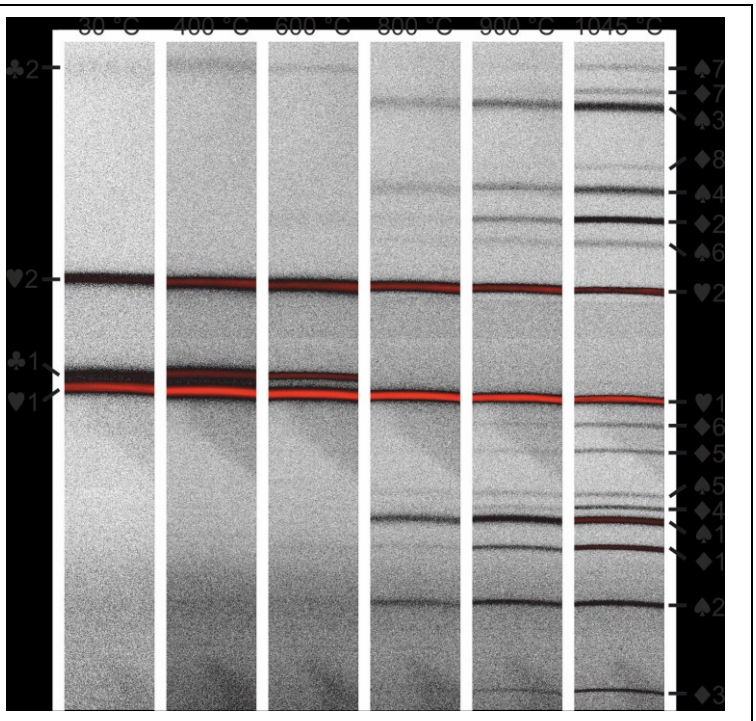

Figure 1: GIXRD patterns collected at different temperatures from 30 °C up to 1045 °C at an incident angle of Θ = 2°. The peaks have been assigned as followed: γ-Fe (♥), α-Fe or martensite (♣), Fe_3O_4 or γ-Fe_2O_3 (♠) and Cr_2O_3 (♦).

In summary the performed GIXRD in-situ measurements are appropriate to study the oxidation processes on Cr-Ni steels under N_2 atmosphere at high temperatures. In a next step the behavior under N_2/SiH_4 atmospheres will be examined.

Acknowledgements

The research has been funded by the German Research Foundation (DFG, grant numbers MA1175/48-1 and FR1388/8-1). The authors gratefully thank the DELTA machine group for providing reliably synchrotron radiation.

References

[1] R.Y. Chen, W.Y.D Yeun. Oxid. Met. 59, 2003, 433-468.

[2] D. Lützenkirchen-Hecht, D. Wulff , R. Wagner, R. Frahm, U. Holländer, H. J. Maier. J. Mater. Sci. 49 (2014) 5454-5461.

[3] D. Lützenkirchen-Hecht, D. Wulff, R. Wagner, U. Holländer, H.J. Maier, R. Frahm: J. Phys.: Conf. Ser. 712, 2016, 12047.

[4] B. Bornmann, D. Wulff, R. Wagner, D. Lützenkirchen-Hecht, K. Möhwald, R. Frahm. Commissioning of a high temperature heater cell for in-situ ReflEXAFS studies of steel surfaces under variable reductive gas atmospheres, In: Sternemann, C.; Wagner, R.; Lützenkirchen-Hecht, D. (Hrsg.): 12th DELTA User Meeting & Annual Report 2016. Dortmund, 30.11.2016, S. 11-13.

Small Angle X-Ray Scattering on Nanoporous Alumina

Mona Erfani, Stephanie Müller, Ullrich Pietsch, Holger Schönherr, Universität Siegen

In our study we investigated polymer-filled nanoporous aluminum oxide using small angle x-ray scattering (SAXS) experiment in order to obtain information on characteristic sizes and filling state inside the pores after filling with a polymer. The results can be used to find optimum condition of sample preparation.

Samples are disc-like alumina films with the diameter of 1 cm and thickness of 100 to 200 microns. The pores prepared by anodic oxidation, are arranged hexagonally and the interpore distance is either 110 nm or 65 nm with pore diameter 70 nm and 40 nm, respectively. Pores were filled with PNIPAM with concentrations of 0.1 w%, 1 w% and 3 w% in solution and are examined at filled and also empty states at room temperature. By adding water and increasing the temperature above 30°C the polymer is expected to swell changing the scattering density of the nanoporous alumina.

Data were analyzed modelling the intensity at central maximum and 2nd and 3rd local maximum [1]:

$$I_0 = \left(\frac{r}{d}\right)^2 + \left(1-\frac{r}{d}\right)^2 c_1^2 + 2\frac{r}{d}\left(1-\frac{r}{d}\right)c_1 c_2 \qquad (1)$$

$$I_m = \left(\frac{\sin\left(m\pi\frac{r}{d}\right)}{m\pi}\right)^2 (1 + c_1^2 - 2c_1 c_2) \qquad (2)$$

The model considers a gratings with material constants c_1 and c_2 and an *effective diameter ratio* $\frac{r}{d}$. We observe a change in r/d adding water but we could not measure a further change while changing the temperature. Therefore swelling of the polymer is not confirmed so far.

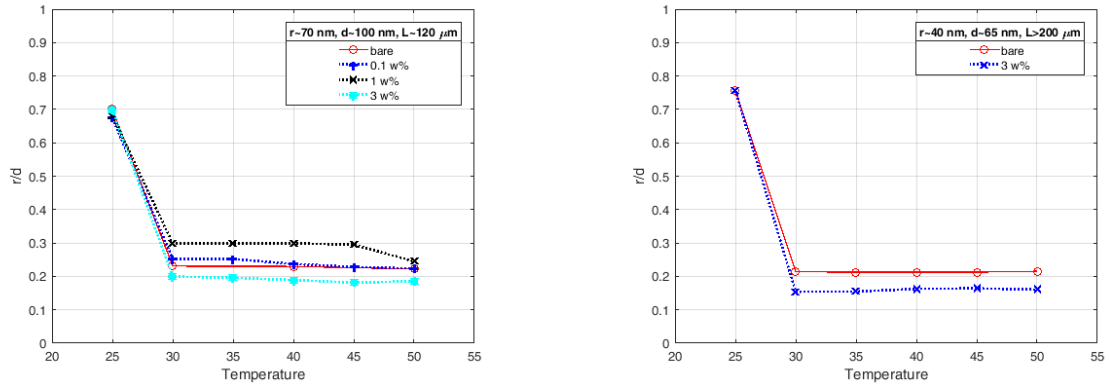

Fig.3. effective diameter ratio as function of temperature for large (left) and small (right) samples

The distribution of effective diameter ratio $\frac{r}{d}$ is also checked and the deviations from the mean values for both sample sizes are at the order of -3. However, the interpore distances are evaluated to be 101.3 nm and 67.3 nm. Having effective diameter ratio and interpore distance, pore diameters are calculated as 68.46 nm and 45.31 nm for empty samples.

[1] L. E. Ruggles, M. E. Cuneo, J. L. Porter, D. F. Wenger, and W. W. Simpson, Rev. Sci. Ins. **72**, 1218 (2001)

DELTA user report 2017
Proposer: Prof. Dr.-Ing. A. Ludwig
Co-Proposers: P. Decker, T. Oellers, D. Grochla, L. Banko, D. Naujoks, S. Salomon

Structural investigation of a Ti-Ta-Sn materials library

P. Decker
Werkstoffe der Mikrotechnik, Institut für Werkstoffe, Fäkultät Maschinenbau
Ruhr-Universität Bochum, D-44801 Bochum

Ti-Ta-based materials are promising candidates for future shape memory applications at elevated temperatures [1,2]. Upon cooling, the fcc β phase (Ti,Ta) transforms into bct α'' martensite. However, the initial formation of the α'' martensite is depending heavily on the process parameters during fabrication and the addition of other elements to the Ti-Ta base alloy [3,4].

A Ti-Ta-Sn materials library was fabricated to explore the influence of Sn addition to Ti-Ta. The materials library was deposited in a multilayer approach and annealed for 6 hours at 700°C in a vacuum atmosphere to facilitate intermixing and phase formation. Grazing incidence diffraction with an incidence angle of Θ = 3° was performed at BL 9 using a beam energy of 20 keV and a mar345 image plate detector to investigate the phase formation in the materials library. 324 individual measurement areas on the materials library were investigated.

The phase analysis revealed both metallic phases and oxides. However, the diffraction signals correlated to oxides only occurred alongside those of the metallic phases and were low in intensity, indicating that only surface oxidation occurred. Regarding the metallic phases, the β austenite phase is stable in a broad composition range (fig. 1) and the α'' martensite phase can be identified to be stable for relatively high Sn concentrations.

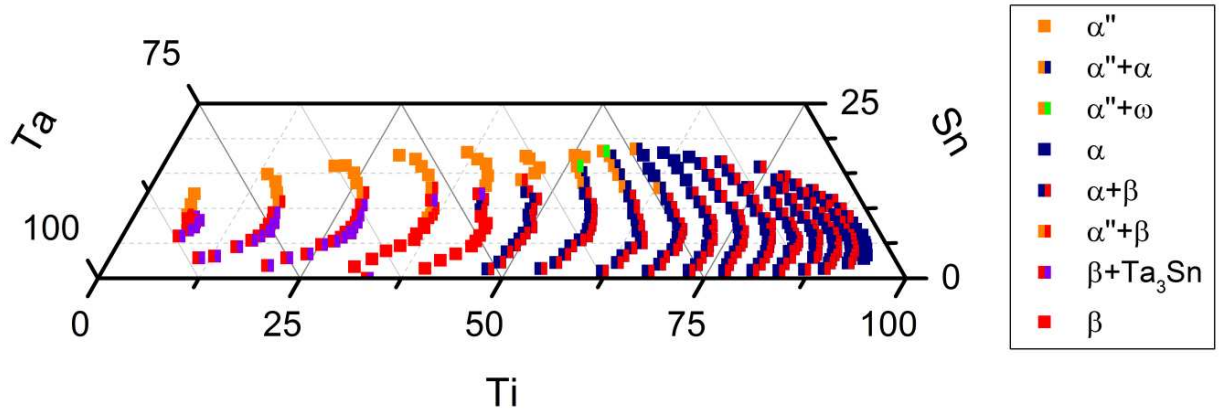

Figure 1: *Phase analysis of the Ti-Ta-Sn materials library based on the grazing incidence diffraction measurements.*

The intermetallic compound Ta_3Sn and the non-transforming low temperature modification α were found as well. A small composition region contains both the α'' and the ω phase, which eventually hinders the martensitic transformation [5].

A phase analysis was also performed for the oxide diffraction signals and compared to optical features on the materials library after the annealing process (fig. 2). This comparison shows a good correlation between specific oxide phases (colored symbols, fig. 2) and the optical features on the materials library's surface.

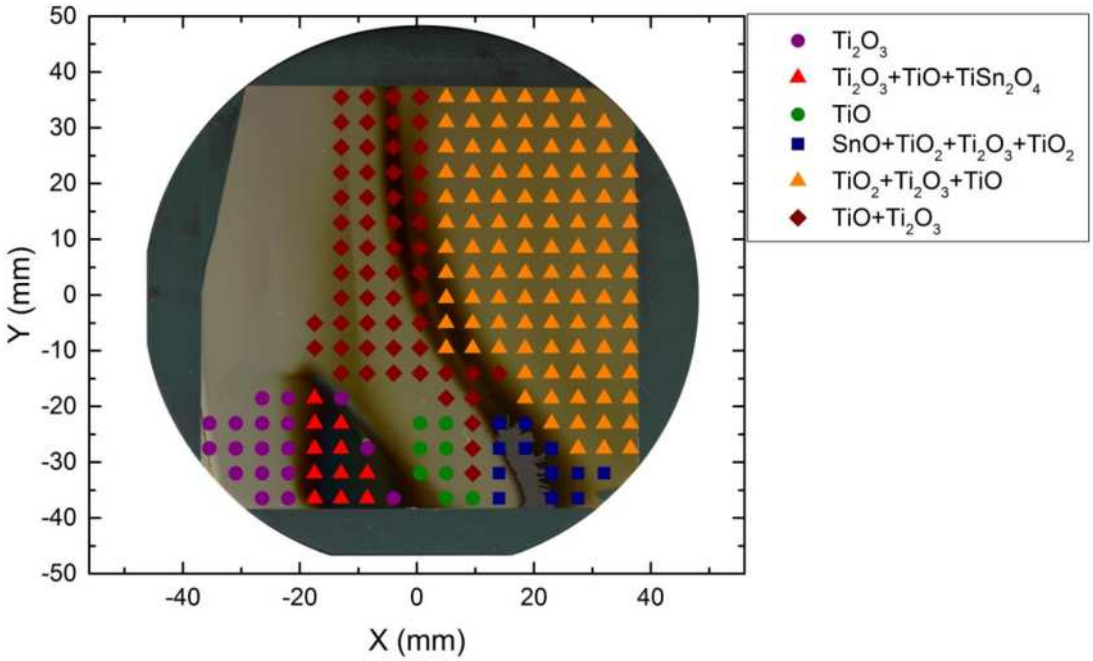

Figure 2: *Photograph of the materials library after the annealing procedure. The colored symbols indicate different forms of oxides. Their distribution fits to the optical surface features.*

References

[1] S. Miyazaki, H.Y. Kim, H. Hosoda, Development and characterization of Ni-free Ti-base shape memory and superelastic alloys, Materials Science and Engineering: A 438-440 (2006) 18–24.

[2] E. Bertrand, P. Castany, Y. Yang, E. Menou, T. Gloriant, Deformation twinning in the full-α″ martensitic Ti–25Ta–20Nb shape memory alloy, Acta Materialia 105 (2016) 94–103.

[3] P.J.S. Buenconsejo, H.Y. Kim, S. Miyazaki, Effect of ternary alloying elements on the shape memory behavior of Ti–Ta alloys, Acta Materialia 57 (2009) 2509–2515.

[4] H.Y. Kim, T. Fukushima, P.J.S. Buenconsejo, T.-h. Nam, S. Miyazaki, Martensitic transformation and shape memory properties of Ti–Ta–Sn high temperature shape memory alloys, Materials Science and Engineering: A 528 (2011) 7238–7246.

[5] B.S. Hickman, The formation of omega phase in titanium and zirconium alloys, J Mater Sci 4 (1969) 554–563.

DELTA user report 2017
Proposer: Prof. Dr.-Ing. A. Ludwig
Co-Proposers: P. Decker, T. Oellers, D. Grochla, L. Banko, D. Naujoks, S. Salomon

In-depth phase analysis on a Co-Mn-Ge-Al-Si thin film materials library by high-throughput GI-XRD experiments

S. Salomon
Werkstoffe der Mikrotechnik, Institut für Werkstoffe, Fäkultät Maschinenbau
Ruhr-Universität Bochum, D-44801 Bochum

The material Co-Mn-Ge is of current scientific interest specifically due to its magnetocaloric properties. Because it shows both a structural transition between the hexagonal CoMnGe high-temperature (HT) phase (space group P63/mmc) and the orthorhombic CoMnGe low-temperature (LT) phase (space group Pnma) and a magnetic transition between the ferromagnetic and the paramagnetic state, it can exhibit a so called giant magnetocaloric effect (GMCE) [1]. This is the case when both transitions are triggered in a similar temperature range and are therefore coupled. Liu et al. showed that this coupling occurs for a composition of $Co_{0.95}MnGe_{0.97}$ with the coupled transition taking place near room temperature [2]. For the optimization of the magnetocaloric properties of the material, which include also the hysteretic transition behavior, the addition of further elements is worth investigating. For this purpose, a Co-Mn-Ge-Al-Si materials library (ML) was deposited on a (100) Si wafer with a SiO_2 diffusion barrier (1.5 µm) by sputter deposition (*DCA Instruments, Finland*) in a multilayer approach (nominal overall film thickness of 500 nm) with programmable shutter blades to cover a large composition range around the 1:1:1 ratio between Co, Mn and Ge (similar to prior research [3]) and to include about 0.5 at.% of Al and Si each homogenously across the whole ML. The ML was annealed in Ar atmosphere at 600°C for 2 hours to facilitate diffusion and phase formation in the thin film. A preliminary phase analysis was performed based on EDX (*INCA X-act detector, Oxford Instruments*) and XRD (*X'Pert Pro, PANalytical,* Cu-K_α radiation, Bragg-Brentano geometry) mapping results.

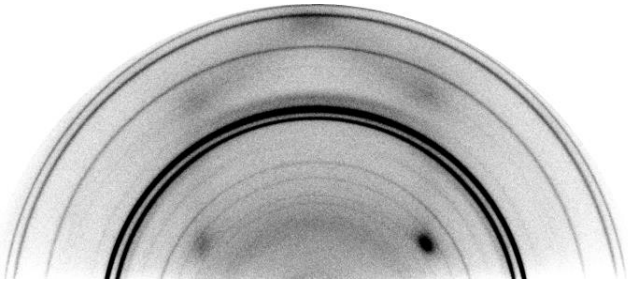

***Figure 1**: 2D diffraction pattern of a measurement region with a composition of $Co_{35}Mn_{29}Ge_{36}$. The pattern with a pentagonal appearance is caused by diffuse scattering at the substrate. The other diffraction signals show a mostly homogeneous intensity distribution along the azimuth and correlate to CoMnGe (HT&LT).*

Based on this preliminary analysis, the measurement areas for an in-depth analysis by grazing incidence XRD (GI-XRD) at BL 9 were selected to precisely identify the regions on the ML where CoMnGe (HT&LT) exists exclusively. The experiments were performed with a beam energy of 20 keV, a beam size of 1 mm x 1 mm and an incidence angle of $\Theta = 3°$ using a mar345 image plate detector.

Figure 1 shows an exemplary 2D diffraction pattern of one of the measurement areas. The pattern with pentagonal appearance is caused by diffuse scattering at the substrate. Almost all diffraction signals from the thin film show a mostly homogeneous azimuthal intensity distribution, which indicates that the thin film is polycrystalline with small crystallites and no significant preferred growth orientation. It can be inferred that the chosen measurement setup is suitable for the identification of the phases present in the ML. The measurements performed at BL 9 also exhibit diffraction signals that are not visible in the preliminary measurements and thus yield more information for a thorough phase analysis. This is particularly important to identify the measurement areas that contain the CoMnGe (HT&LT) phases exclusively.

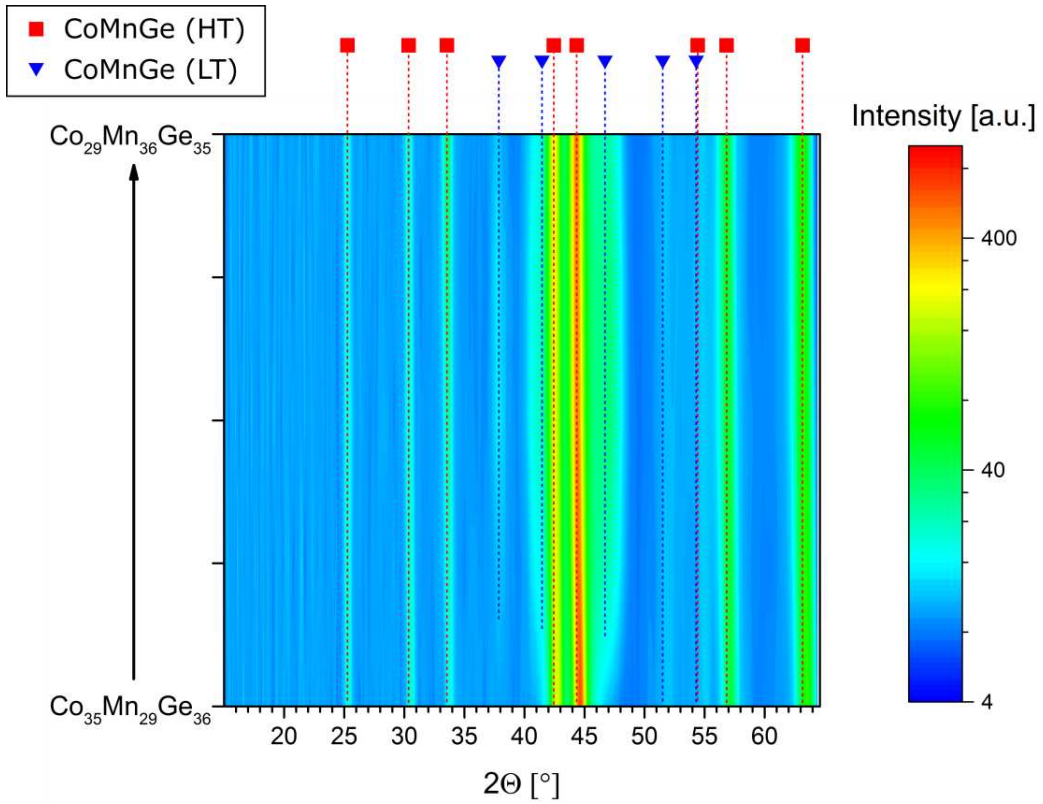

***Figure 2**: Diffraction patterns integrated along the azimuth and plotted over 2Θ (Cu-K_α) for increasing Co and decreasing Mn contents as indicated. The signal intensity is shown color-coded (logarithmic scale). The diffraction peaks were identified to correlate with CoMnGe (HT), red squares, and CoMnGe (LT), blue triangles.*

The analysis across a select area on the ML showed that both CoMnGe (HT) and CoMnGe (LT) can be identified in the thin film. They are found exclusively in a very narrow range of Ge contents around 35 at.% with decreasing Co and increasing Mn contents from $Co_{35}Mn_{29}Ge_{36}$ to $Co_{29}Mn_{36}Ge_{35}$ (see figure 2). However, it is difficult to exclude the presence of Co_2MnGe (space group Fm-3m) based on the shown measurement data, because in the measured range it is mainly characterized by the (220) diffraction signal near 44.8°, which can coincide with the (110) signal from CoMnGe (HT). Because of the low intensity of the (111) signal of Co_2MnGe near 27°, which was found in adjacent measurement areas, relative to the (220) signal, its absence is not sufficient proof for the absence of this phase. To exclude the presence of Co_2MnGe, further experiments need to be done either at BL 9 with a different measurement range or using a suitable lab XRD system to cover further possible diffraction signals from Co_2MnGe.

While most of the diffraction patterns in the composition range shown in figure 2 are very similar, the diffraction pattern for $Co_{35}Mn_{29}Ge_{36}$ shows almost negligible intensities for the diffraction signals that can be correlated to CoMnGe (LT). This might indicate that there is a change in the structural transition temperature towards higher values for an increasing Co and a decreasing Mn content. Outside of the shown composition range, the CoMnGe (HT&LT) phases were either not found or existed alongside additional phases.

This research is part of the SPP 1599 funded by the DFG.

References

[1] J. Liu, T. Gottschall, K.P. Skokov, J.D. Moore, O. Gutfleisch, Giant magnetocaloric effect driven by structural transitions, Nature materials 11 (2012) 620–626.
[2] J. Liu, K. Skokov, O. Gutfleisch, „Magnetostructural transition and adiabatic temperature change in MnCoGe magnetic refrigerants“, Scripta Materialia, 66, 642-645, 2012
[3] S. Salomon, S. Hamann, P. Decker, A. Savan, L. Meshi, A. Ludwig, Combinatorial synthesis and high-throughput characterization of the thin film materials system Co-Mn-Ge: Composition, structure, and magnetic properties, Phys. Status Solidi A 212 (2015) 1969–1974

The interaction of viral fusion peptides with model lipid membranes

Göran Surmeier, Michael Paulus, Christian Sternemann, Paul Salmen, Christian Albers, Jennifer Bolle, Fatima Mallal, Steffen Bieder, Metin Tolan, and Julia Nase

Fakultät Physik/DELTA, TU Dortmund, 44221 Dortmund, Germany

Email: goeran.surmeier@tu-dortmund.de

We investigated the interaction of viral fusion peptides with model lipid membranes by studying the pressure-dependent phase behavior of monoolein/water mixtures in absence and presence of the fusion peptide of Hemagglutinin 2 (HA2-FP). As monoolein/water mixtures form various hexagonal, cubic, and lamellar phases in an accessible pressure- and temperature range, they are a well-suited model system to examine the influence of fusion peptides on structural properties of lipid membranes. We conducted small angle x-ray scattering (SAXS) measurements in order to monitor the volume phase of the lipid system. Moreover, we investigated the near-surface behavior at a hydrophilic silicon wafer using the x-ray reflectivity (XRR) technique, as the formation of highly ordered multilayers at such a surface enables to resolve the vertical lipid layer structure. In addition, we recorded grazing incidence (GI) SAXS patterns that contain information on the orientation of lipid phases in the near-surface area and make it possible to clearly distinguish between volume- and surface effects.

We conducted all measurements at beamline BL9 at DELTA. These measurements were performed in a custom-made high hydrostatic pressure cell [1] at a photon energy of 25 keV. The beam size was 0.1 mm (vertical) × 1 mm (horizontal). Pressures between 50 and 5000 bar and a temperature of 25 °C were applied. A hydrophilic silicon wafer was introduced into the cell and the cell volume was filled with a mixture of monoolein and 40 %wt BisTris buffer solution at pH 5. The fusion peptide of Hemagglutinin 2 was added in a concentration of 2 %wt.

The SAXS data show that the monoolein lipids form cubic phases at 50 bar in absence and presence of the fusion peptide. Typically, the Pn3m phase is predominant at low pressures. For pure monoolein/water mixtures, the Im3m phase forms and a coexistence of both phases is observed when the pressure is increased. Between 2500 and 3000 bar, a phase transition into a lamellar phase occurs (*figure 1*). In contrast, the lamellar phase grows in the near-surface area already at pressures between 1000 and 2000 bar indicated by the XRR (*figure 2*) and GISAXS measurements. This effect occurs at even lower pressures once the fusion peptide is added. Already at 500 bar, a multilayer formed at the surface in presence of HA2-FP. Notably, for pressures of more than 1000 bar, lamellar structures are also detected in the volume and a coexistence of lamellar and cubic phases is observed. The cubic phase disappears between 2500 and 3000 bar and the whole systems forms lamellar structures. A detailed data analysis is still in progress.

Acknowledgments: This work is supported by the Forschergruppe 1979 (**DFG-FOR1979**). We also acknowledge the Delta machine group for providing synchrotron radiation and technical support.

References

[1] F.J. Wirkert, M. Paulus, J. Nase, J. Möller, S. Kujawski, C. Sternemann, and M. Tolan, *X-ray reflectivity measurements of liquid/solid interfaces under high hydrostatic pressure,* Journal of Synchrotron Radiation 21, 76 (2014).

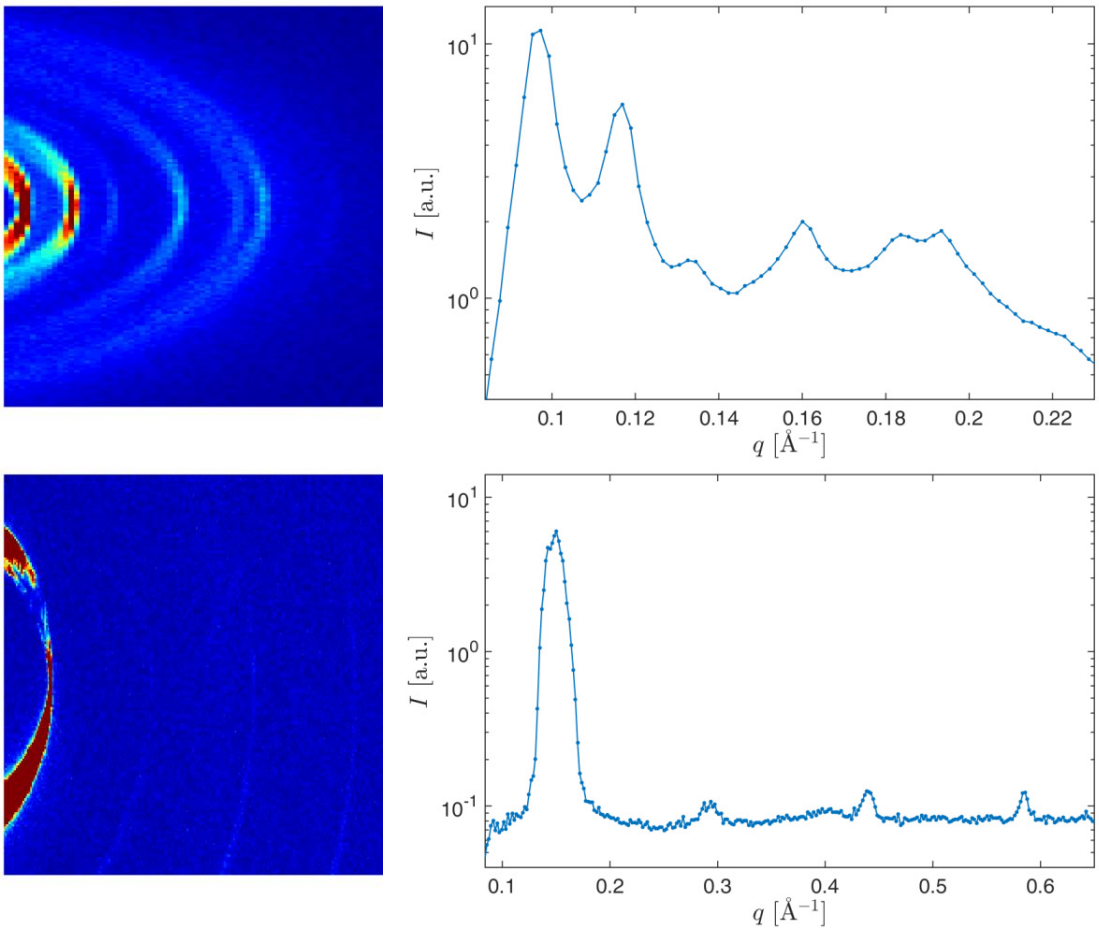

Fig. 1: Detector image and integrated SAXS data of a monoolein/water mixture in the cubic Pn3m phase (top) and in a lamellar phase (bottom).

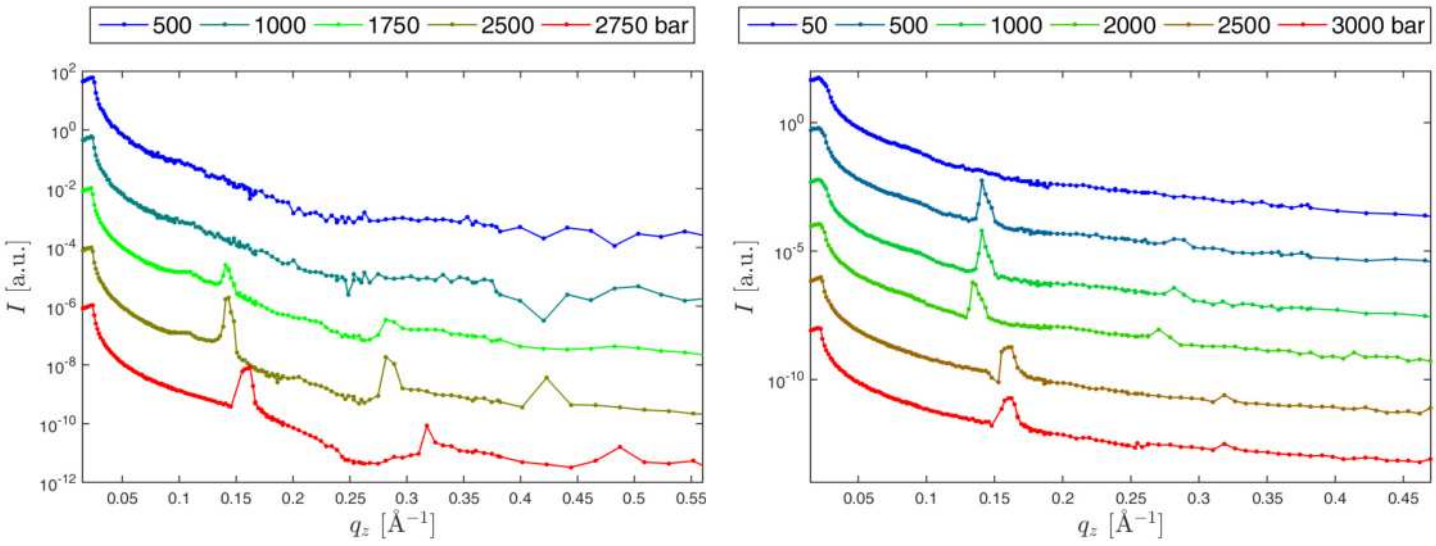

Fig. 2: Reflectivity data of a monoolein/water mixture in absence (left) and presence (right) of HA2-FP.

Compressibilities of solid-supported DMPC membranes containing cholesterol at high hydrostatic pressure

Göran Surmeier, Michael Paulus, Christian Sternemann, Susanne Dogan, Lukas Tepper, Christian Albers, Yury Forov, Steffen Bieder, Julian Schulze, Julia Nase, and Metin Tolan

Fakultät Physik/DELTA, TU Dortmund, 44221 Dortmund, Germany

Email: goeran.surmeier@tu-dortmund.de

We conducted a high energy X-ray reflectivity (XRR) study on the pressure-dependent behavior of solid-supported model lipid membranes containing different amounts of cholesterol. A lipid membrane is the basic component of cell membranes, which separates the intracellular and extracellular region and regulates the mass transfer between these regions in all living organisms. It consists mainly of a phospholipid bilayer that is interstratified by cholesterol and proteins. For our model system, we use DMPC (1,2-dimyristoyl-*sn*-glycero-3-phosphocholine) multilayers containing cholesterol concentrations between 0 and 35 mol% that are prepared at a hydrophilic silicon dioxide surface of a silicon wafer by spin coating [1].

In order to obtain information on the vertical arrangement of these membranes, we conducted high energy XRR measurements at the solid-liquid interface between silicon and an aqueous buffer solution at beamline BL9 of DELTA. These measurements were performed in a custom-made high hydrostatic pressure cell [2] at a photon energy of 27 keV. The beam size was 0.1 mm (vertical) × 1 mm (horizontal). Pressures up to 4 kbar and a temperature of 20 °C were applied.

This study is a continuation of experiments conducted at ID31 at the ESRF (European Synchrotron Radiation Facility) and at BL9 at DELTA in 2016 (see our report from 2016). In those experiments, we observed a minimum in the linear compressibility in the vertical direction of DMPC multilayers in a gel-like phase for low cholesterol concentrations. As figure 1 shows, the current measurements confirm this result. The calculation of the compressibilities is based on the observation of changes of the bilayer thickness with increasing pressure, which can be extracted from the positions of Bragg reflections in the reflectivity data.

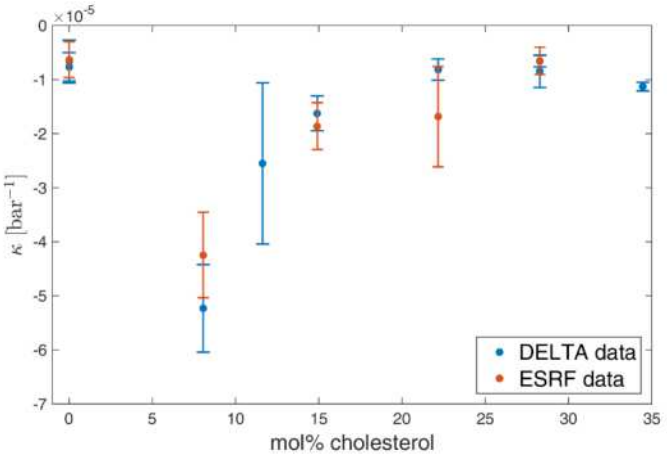

Fig. 1: Compressibilities of DMPC multilayers containing different concentrations of cholesterol.

Acknowledgments: This work is supported by the Forschergruppe 1979 (**DFG-FOR1979**) and Cluster of Excellence RESOLV (**EXC 1069**) founded by the DFG.

References

[1] B. Nowak, M. Paulus, J. Nase, P. Salmen, P. Degen, F.J. Wirkert, V. Honkimaki, and M. Tolan, *Solid supported lipid multilayers under high hydrostatic pressure,* Langmuir 32, 11 (2016).

[2] F.J. Wirkert, M. Paulus, J. Nase, J. Möller, S. Kujawski, C. Sternemann, and M. Tolan, *X-ray reflectivity measurements of liquid/solid interfaces under high hydrostatic pressure,* Journal of Synchrotron Radiation 21, 76 (2014).

S-layer-supported lipid membranes

Irena Kiesel[*], Wiebke Schnettger[*], Mridula Dwivedi[*], Mimi Gao[*], Bernhard Schuster[+]
[*] Physikalische Chemie 1, TU Dortmund
[+] Institut für Synthetische Bioarchitekturen, BOKU Wien

Scientific Background

Biomimetic model membranes have already been proven to constitute distinguished platforms for studying membrane related processes like transport in or out of cells or behavior under pressure. Solid-supported membranes are an established model system, but the solid support can hinder molecules to cross the membrane. To allow molecules to penetrate the artificial membrane, a soft cushion is needed between the membrane and the solid substrate.[1]

Surface (S)-layer proteins (SLPs) are often found as outermost cell envelope component on many bacteria and almost all archaea. Proposed function of SLPs include the stabilization of the cell membrane against pressure, e.g., in deep sea, or temperature. Bacterial SLPs self-assemble as a 2D crystal structure on solid surfaces with a thickness of 5-10 nm containing pores of a diameter between 2-8 nm.[2] As they naturally cover cell membranes, are suitable structures to be utilized as a cushion for a biomimetic solid supported model membrane (Fig. 1). Previous experiments have shown that SLPs adsorb at lipid monolayer at the liquid air interface, but do not penetrate them.[3] The latter is crucial for the fluidity of the supported membranes and therefore the ability for molecules to pass them.

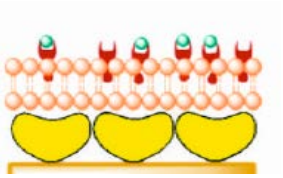

Figure 1 Scheme of S-Layer proteins (yellow) as cushion for lipid bilayer (orange), including β-linker (red) and $EuCl_3$ (green). Taken from [2].

Lipid bilayers on SLPs adsorbed on gold surfaces were already investigated with quartz crystal microbalance with dissipation monitoring and electrochemical impedance spectroscopy [2], but so far, no structural information is known about this system.

Experiment

Silicon wafers (7.6x7.6 mm^2) were cleaned with organic solvents (chloroform, acetone and ethanol) under sonication and 5 min under oxygen atmosphere. Cleaned wafers were stored in MilliQ water until usage. Further sample preparation has been performed during the experiment. S-Layer proteins were allowed to recrystallize on the silicon surface under rotation for at least 3 h (crystallization has been proofed with AFM measurements previously). Vesicles were formed via solvent evaporation, dehydration, freeze/thaw cycles and extrusion. After the activation of the protein surface with EDC (1-ethyl-3-(3-dimethyl-aminopropyl)carbodiimide), vesicles (1 mg/mL in 2mM glucose) were injected and allowed to bind for 1 hour. The usage of 1% β-linker in the vesicles, which form a 2:1 complex with $EuCl_3$ (0.26 mg/mL 200mM glucose) was intended to help bilayer formation. Further details to the preparation protocol can be found in literature.[2]

Reflectometry measurements were carried out at each step of the preparation: 1) Silicon in glucose, 2) with SLP, 3) with vesicles in solution, 4) after applying the $EuCl_3$ solution and removing not adsorbed vesicles. Several different preparation procedures, different solution concentrations, increased temperature (55°C) and applying pressure (using the high pressure sample cell), were tested in order to

find a way to prepare a lipid bilayer on the SLP-coated silicon wafers. Reflectometry measurements were performed at beamline BL9 at DELTA with the 27 keV high pressure reflectometry setup. [4,5]

Results and Discussion

The measured reflectivities shown in Figure 2 are multiplied with q^4 to enhance the visibility of small changes. Several preparation steps are shown. Beside the last sample, in which we included all preparation components at the same time, no significant change has been observed in the reflectivity curve. For SLPs, the reason could be either a close electron density of the protein layer, an inhomogeneous protein layer or a high roughness. The fact that no fringes are visible in the case of vesicles indicates either that no bilayer is formed, probably because the vesicles did not open on the protein layer, or that the roughness is in the order of the bilayer or that the layer is inhomogeneous. As vesicles do not open easily on soft cushions, different preparation protocols were tested. One idea has been that the exchange of liquids within the sample cell was not sufficient, so samples were prepared outside. Other approaches have been an increase of concentrations (vesicles, EDC, $EuCl_3$), increased temperature (55°C) and the application of pressure. In none of those cases a bilayer formation has been observed. Only in the case, in which all components were put together into the sample cell simultaneously, a change in the reflectivity curve has been observed. Unfortunately, the analysis of this approach is not possible, as neither a pure bilayer nor a bilayer on top of the protein layer refines the measured data. In conclusion, further work needs to be done to prepare successfully a lipid bilayer on SLPs. One promising approach is the usage of the Langmuir-Blodgett/Langmuir-Schaefer technique instead of vesicle fusion.

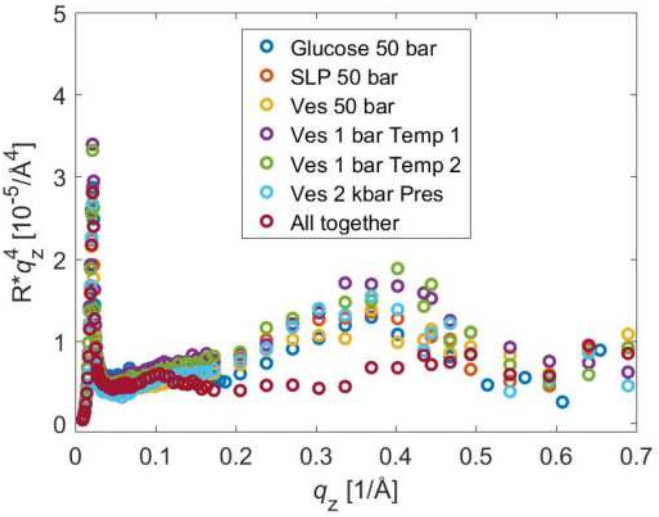

Figure 2 Reflectivity measurements, multiplied by q^4 to enhance visibility of small changes, of several steps of the preparation.

References

[1] W. Knoll, R. Naumann, M. Friedrich, J. W. F. Robertson, M. Lösche, F. Heinrich, D. J. McGillivray, B. Schuster, P. C. Gufler, D. Pum, et al., *Biointerphases* **2008**, *3*, FA125.

[2] S. Damiati, A. Schrems, E.-K. Sinner, U. B. Sleytr, B. Schuster, *Int. J. Mol. Sci.* **2015**, *16*, 2824–2838.

[3] M. Weygand, B. Wetzer, D. Pum, U. B. Sleytr, N. Cuvillier, K. Kjaer, P. B. Howes, M. Lösche, *Biophys. J.* **1999**, *76*, 458–468.

[4] M. Paulus, D. Lietz, C. Sternemann, K. Shokuie, F. Evers, M. Tolan, C. Czeslik, R. Winter, *J. Synchrotron Radiat.* **2008**, *15*, 600–605.

[5] F. J. Wirkert, M. Paulus, J. Nase, J. Möller, S. Kujawski, C. Sternemann, M. Tolan, *J. Synchrotron Radiat.* **2013**, *21*, DOI 10.1107/S1600577513021516.

Acknowledgement:
We would like to thank DELTA for the awarded beamtime. Furthermore, we are thankful for support at beamline BL9 by P. Salmen and with the high pressure setup by G. Surmeier. IK thanks the Cluster of Excellence RESOLV (EXC 1069) and BS the Austrian Science Fund (FWF) project P 29399-B22 for financial support.

Supramolecular structures of mixtures of 4M3H and 2E1H at low temperature

Jennifer Bolle, Christian Sternemann, Christian Albers, Göran Surmeier, Fatima Mallal, Robin Sakrowski and Metin Tolan
Fakultät Physik/DELTA, Technische Universität Dortmund, 44221 Dortmund, Germany

Monohydroxy alcohols (MAs) have been scrutinized as a model of hydrogen bonded fluids. These hydrogen bonds are essential for the understanding of the microscopic structure of water, aqueous solutions and alcohols [1]. Mediated by hydrogen bonds the MAs can create ring or chain like supramolecular structures. In this experiment mixtures of 4M3H (4-methyl-3-heptanol) and 2E1H (2-ethyl-1-hexanol) have been studied in order to reveal structural information of supermolecular arrangements. From e.g. dielectric spectroscopy it is known that 4M3H is a ring former whereas 2E1H is a chain former. In our studies we used X-ray diffraction (XRD) at the Beamline 9 of DELTA. In order to obtain information about typical length scales in the liquids. The XRD pattern of MAs and their mixtures show two distinct peaks. The mainpeak at higher momentum transfer (q) is predominant due to the carbon-carbon correlations in the liquid. The prepeak at lower q originates from supramolecular arrangements with typical length scales larger than a single molecule. Its position reflects typical distances owing to oxygen-oxygen correlations.

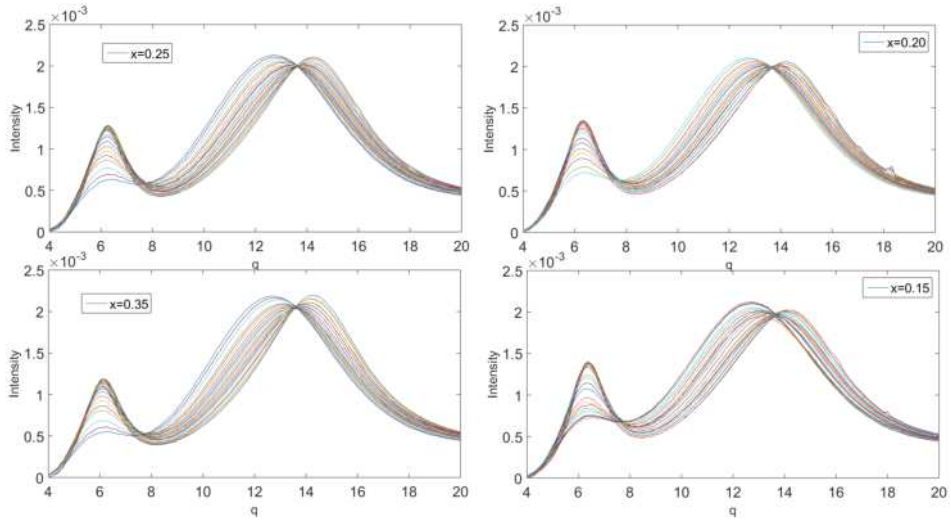

Figure 1: Diffraction patterns of $(2E1H)_x(4M3H)_{1-x}$ mixtures with x=0.15, 0.20, 0.25, 0.35 measured at different temperatures in the range from 175 K to 405K

Our measurements are inspired from the dielectric experiments by S. Bauer et al. [2]. They calculated the Kirkwood factor from dielectric spectroscopy studies of 4M3H/2E1H mixtures at low temperature. The Kirkwood factor quantifies to the angle between different dipole vectors of molecules in the liquid [3]. If the Kirkwood factor is below 1, the dipoles of a supramolecular arrangement have anti-parallel orientation, as present in ring structures of the MAs. Is the Kirkwood factor above 1 the MAs form chains. In this case the dipoles have parallel orientation. Some mixtures exhibit a transition from $g_K > 1$ to $g_K < 1$ with changing the temperature. The corresponding transition temperatures shift with increasing concentration to higher values, indicating a change in the dominated species from rings to chains. Using XRD we aim to observed indications of structural crossover.
The MAs were filled in 2 mm borosilicate capillaries and were measured at an energy of 25 keV. The capillaries were cooled with a 700 Series Cryosteam Cooler. The temperature was decreased in steps of 10 K from 295 K to 175 K. Afterwards the temperature was increased from 295 K to 405 K. At each temperature diffraction patterns were recorded.

The figure 1 shows the diffraction patterns of the mixtures $(2E1H)_x(4M3H)_{1-x}$ with the molar concentrations x=0.15, 0.20, 0.25, 0.35 . For a detailed analysis of the main- and prepeak a linear background was subtracted. Then the peak was fitted with a pearson VII-function. The figure 2 shows the peakposition of the different concentrations in the temperature range 175 - 405 K. Because of the connection between the prepeak position and the typical distances

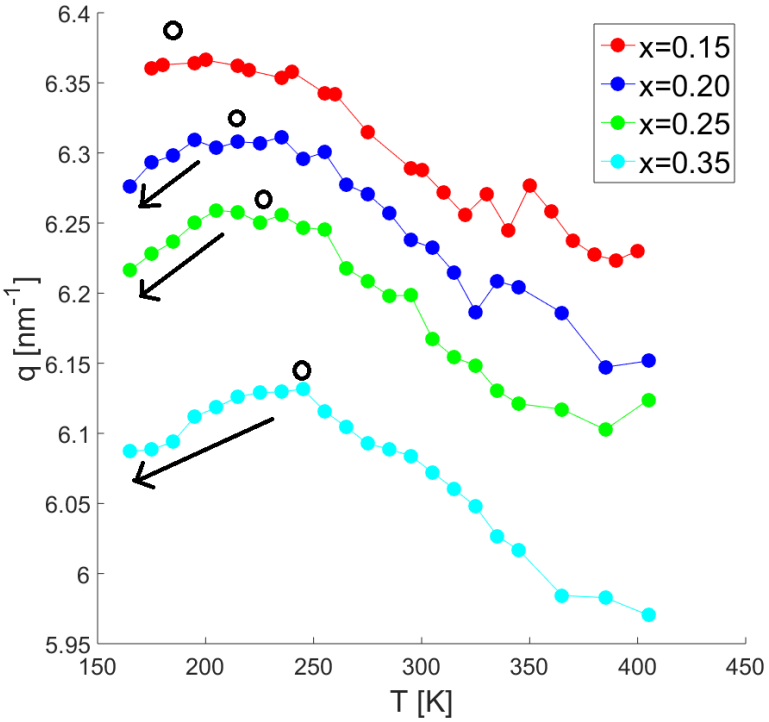

Figure 2: Prepeakposition of the mixtures $(2E1H)_x(4M3H)_{1-x}$ with the molar concentrations x=0.15, 0.20, 0.25, 0.35 at temperatures from 175K to 405K

between supramolecular arrangements, the peakposition gives a hint for the structural change. The progression of the peak positions changes with increasing concentration. The mixtures with higher concentration tend to shift towards lower q (Fig. 2 black arrows) with decreasing temperature. After the maximum (indicated by circles in Fig. 2) q decreases with rising temperature. This maximum shifts with increasing x to higher temperature. This is similar to the results of the dielectric studies [2]. The decrease of q indicates an increase of the intermolecular distance of supramolecular arrangement in agreement of chain formation [4]. Further insights could be gained by measurements with higher 2E1H concentrations. A detailed analysis is in progress.

References

[1]Kaatze, U., Behrends, R., & Pottel, R. (2002). Hydrogen network fluctuations and dielectric spectrometry of liquids. Journal of Non-Crystalline Solids, 305(1), 19-28. [2] S Bauer et al. “Broadband dynamics in neat 4-methyl-3-heptanol and in mixtures with 2-ethyl-1-hexanol”. In: The Journal of chemical physics 139.13 (2013), p. 134503. [3] Roland Böhmer, Catalin Gainaru, and Ranko Richert. “Structure and dynamics of monohydroxy alcohols Milestones towards their microscopic understanding, 100 years after Debye”. In: Physics Reports 545.4 (2014), pp. 125–195. [4] Bierwirth, S. P., Büning, T., Gainaru, C., Sternemann, C., Tolan, M., & Böhmer, R. (2014). Supramolecular X-ray signature of susceptibility amplification in hydrogen-bonded liquids. Physical Review E, 90(5), 052807.

Acknowledgement

We would like to thank the Deutsche Forschungsgemeinschaft (DFG-FOR1979) for funding and DELTA for providing synchrotron radiation and technical support.

XRD measurments from 2E1H and halogen-substituted 2-ethyl-1 chloride and 2-ethyl-1 bromide

Jennifer Bolle, Christian Sternemann, Florian Otte, Robin Sakrowski, Catalin Gainaru, Roland Böhmer and Metin Tolan
Fakultät Physik/DELTA, Technische Universität Dortmund, 44221 Dortmund, Germany

Hydrogen bonds are important for the structure formation and dynamics of monohydroxy alcohols. Due to their properties monohydroxy alcohols have been established as a model of hydrogen bonded fluids [1]. In these measurements 2-ethyl-1-hexanol (2E1H) is mixed with the halogen-substituted 2-ethyl-1 chloride (2E1Cl) and 2-ethyl-1 bromide (2E1Br). They have been studied in order to investigate the suppression of hydrogen bonding and its consequences for structure formation in the mixtures. Additional mixtures of n-bromobutan and n-butanol ($(\mathrm{BuOH})_x$ $(\mathrm{BuBr})_{x-1}$) are also studied for comparison with results of Hennous et al [2]. Their MD simulations suggest formation of n-butanol nanodomains embedded in large n-bromobutane regions at a critical concentration of $x_c = 0.5$, that manifests in a shift of the prepeak to smaller q accompanied by a peaksplitting.
The mixtures were filled in 2 mm borosilicate capillaries and were measured at BL 9 with an energy of 10 keV. The XRD patterns are normalized by their integral within the q range from 3 to 9 nm^{-1}. Figure 1a shows the diffraction patterns after the background subtraction. The black circles mark the positions of the prepeak maxima. For further analysis the diffraction patterns

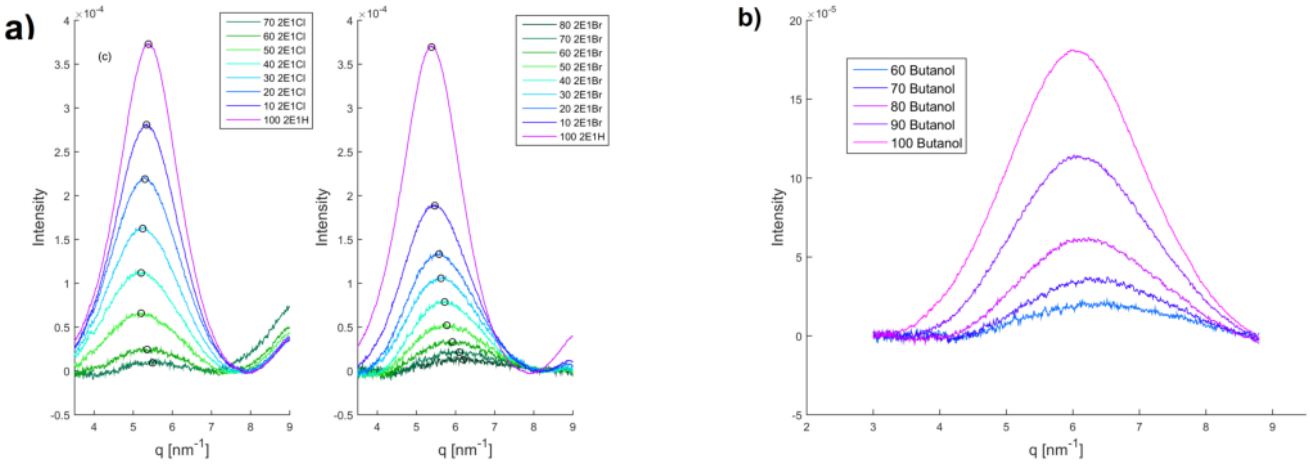

Figure 1: a) XRD patterns of $(2\mathrm{E1H})_x(2\mathrm{E1Cl})_{x-1}$ and $(2\mathrm{E1H})_x(2\mathrm{E1Br})_{x-1}$, b) XRD patterns of $(\mathrm{BuOH})_x$ $(\mathrm{BuBr})_{x-1}$ (x given in % within the legend)

are fitted with a pearson VII-function. The results are represented in figure 2. The intensity of the prepeaks decrease with higher halogen alkane concentration, which hints at the hindrance of hydrogen bonding by the halogen alkane. The intensity vanished at a molar concentration for x<0.30 and x=0.5 for 2E1H and BuOH halogen alkane mixtures, respectively. 2E1Br and BuBr hinder the hydrogen bonding in a more effective way than 2E1Cl. The peakpositon of $(2\mathrm{E1H})_x(2\mathrm{E1Cl})_{x-1}$ hardly changed and the peakposition of the $(2\mathrm{E1H})_x(2\mathrm{E1Br})_{x-1}$ mixture decreases with increasing x. The FWHM of the prepeak does not change over the entire concentration range. Both observations are in contrast to the characteristics of nanodomain formation. The overall behavior of the prepeak is in agreement with behavior of the Debye-process as observed by dielectric spectroscopy.

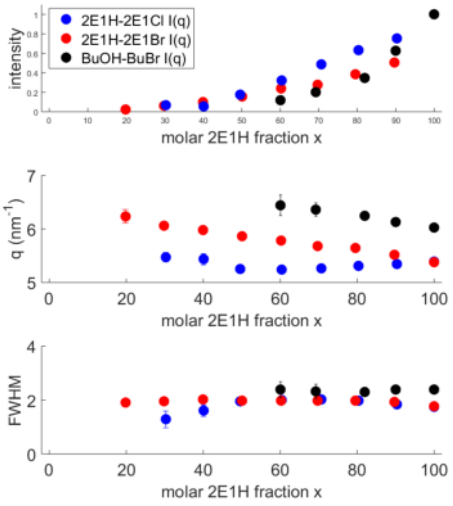

Figure 2: Intensity, position and FWHM of the prepeak for $(2E1H)_x(2E1Cl)_{x-1}$, $(2E1H)_x(2E1Br)_{x-1}$ and $(BuOH)_x(BuBr)_{x-1}$ mixtures (x is given in %)

Reference

[1] Kaatze, U., Behrends, R., & Pottel, R. (2002). Hydrogen network fluctuations and dielectric spectrometry of liquids. Journal of Non-Crystalline Solids, 305(1), 19-28.
[2] Hennous, L., Hamid, A. R. A., Lefort, R., Morineau, D., Malfreyt, P., & Ghoufi, A. (2014). Crossover in structure and dynamics of a primary alcohol induced by hydrogen-bonds dilution. The Journal of chemical physics, 141(20), 204503.

Acknowledgement

We would like to thank the DELTA machine group for providing synchrotron radiation and technical support.

Microstructure-Dependent Charge Carrier Transport of P3HT Ultrathin Films Transistors

Lukasz Janasz,[2] Marzena Gradzka,[2] Tomasz Marszalek,[1,2,4] Wojciech Zajaczkowski,[1] Adam Kiersnowski,[3] Wojciech Pisula[1,2,*]

[1] Max Planck Institute for Polymer Research, Ackermannweg 10, 55128 Mainz (Germany)
[2] Department of Molecular Physics, Faculty of Chemistry Lodz University of Technology, Zeromskiego 116, 90-924 Lodz (Poland)
[3] Faculty of Chemistry, Wroclaw University of Science and Technology, Wybrzeze Wyspianskiego 27, 50-370 Wroclaw (Poland)
[4] Organisch-Chemisches, Institut Ruprecht-Karls-Universitat Heidelberg, Im Neuenheimer Feld 270, 69120 Heidelberg (Germany)
* Email: pisula@mpip-mainz.mpg.de

Since the interfacial order of conjugated polymers plays an essential role for the performance of field-effect transistors, comprehensive understanding on the charge carrier transport in ultrathin semiconducting films below thicknesses of 10 nm is required for the development of transparent and flexible organic electronics. Therefore, in this study, ultrathin films based on poly(3-hexylthiophene) as conjugated polymer model system with a thickness range from single monolayer up to several multilayers were investigated in terms of microstructure evolution and electrical properties of different molecular weights. Investigated films exhibited a significant rise of mobility (from approx. $3x10^{-3}$ to $2.1x10^{-2}$ cm^2/Vs) above the thickness of around 8 nm (4 monolayers). Since such a dramatic change of semiconducting properties occurs between films thinner and thicker than 8 nm, one could expect also a meaningful difference in morphology and crystallinity of the samples. These results have been recently published in Langmuir.[1]

AFM investigation showed that films which showed higher mobility also exhibited a morphology consisting of aggregates larger than their thinner and worse semiconducting counterparts. To investigate the polymer alignment within the P3HT films, and correlate it with electrical and microscopic measurements, GIWAXS experiments were performed for the layers fabricated from P3HT with two different molecular weights - 34 and 94 kDa. Special attention was put to the investigate films with thicknesses directly before and after mentioned rise of the charge carrier mobility. corresponding patterns for the samples are given in Figures 1 and 2. First of all, the measurements proven the high degree of edge-on orientation of polymer chains for all studied samples, despite of the molecular weight of P3HT, or sample thickness. Such observation is important in case of films used as active layers in OFETs, since edge-on orientation of organic molecules favors the charge transport within the conductive channel of the device. Surprisingly, no clear correlation between crystallinity of the samples and charge carrier mobility was observed. Films fabricated from P3HT with lower molecular weight occurred to exhibit a higher degree of crystalline order despite the fact, that those samples had worse charge transporting properties. Furthermore, especially for the films with higher Mw, the difference in crystallinity of the samples, that differed in thickness, was almost negligible.

Those two unexpected results proved that, in the case of ultrathin samples made of P3HT, the degree of crystalline order does not determine the resulting semiconducting properties. Some previous works suggested that, in the case of conjugated polymers, the main driving force for high mobility might be the length of the polymeric chains and short-range aggregation, rather than overall crystallinity of the film. Our results experimentally proved these claims for ultrathin P3HT films.

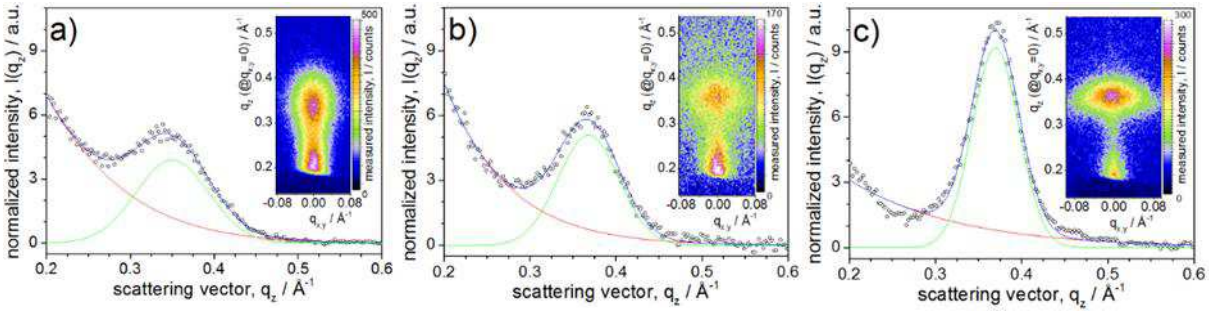

Figure 1. 1D normalized GIWAXS profiles and experimental 2D GIWAXS patterns (insets) of a) 2.6, b) 6.3, and c) 7.2 nm thick $P3HT_{34}$ films (thickness determined by AFM). Hollow circles show the averaged experimental intensity, lines represent the double-Gaussian fit of the experimental points.

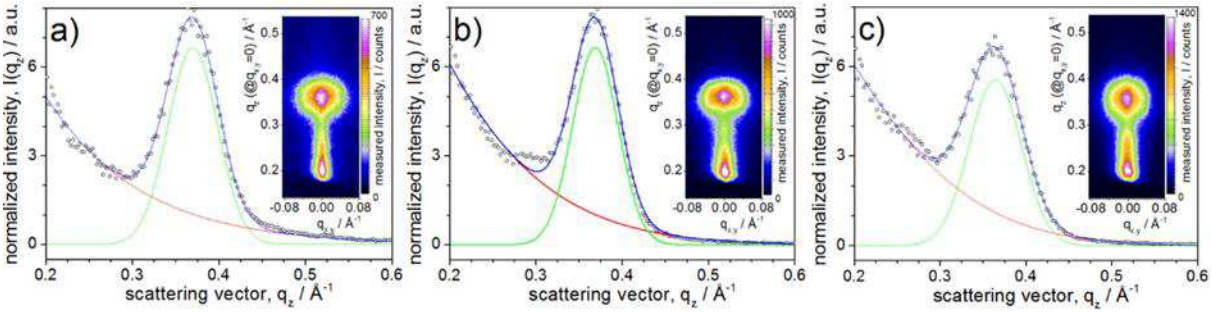

Figure 2. 1D normalized GIWAXS profiles and experimental 2D GIWAXS patterns (insets) of a) 8.1, b) 9.1 and c) 11.0 nm thick $P3HT_{94}$ films (thickness determined by AFM). Hollow circles show the averaged experimental intensity, lines represent double-Gaussian fit of the experimental points.

Acknowledgement

The work was supported by the Polish National Research Centre under the project code UMO-2015/18/E/ST3/00322 (Sonata Bis). The researchers involved in this project express their gratitude to Dr. Christian Sternemann and Dr. Michael Paulus for their help in the experiments.

References

1. Janasz, L.; Gradzka, M.; Chlebosz, D.; Zajaczkowski, W.; Marszalek, T.; Kiersnowski, A.; Ulanski, J.; Pisula, W., Microstructure-Dependent Charge Carrier Transport of Poly(3-hexylthiophene) Ultrathin Films with Different Thicknesses. Langmuir 2017, 33 (17), 4189-4197.

Unraveling the like-charge attraction between microtubules by high hydrostatic pressure SAXS

Mimi Gao[1], Melanie Berghaus[1], Nelli Erwin[1], Marius Herzog[1], Christian Sternemann[2], Roland Winter[1]

[1]Physical Chemistry I - Biophysical Chemistry, Faculty of Chemistry and Chemical Biology, TU Dortmund University, Otto-Hahn Street 4a, 44227 Dortmund, Germany.
[2]Fakultät Physik / DELTA, Technische Universität Dortmund, Maria-Goeppert-Mayer-Str. 2, D-44227 Dortmund, Germany.

The essential eukaryotic cytoskeleton is a dynamic and protein-composed framework that allows spatial and temporal organization of the cells by providing them with structure, shape, dynamics and mechanical resistance. It consists of three main kinds of filaments, which are actin filaments, microtubules and intermediate filaments. Microtubules are the largest among those filaments and are composed of α- and β-tubulin (αβ-tubulin) heterodimers which form linear protofilaments in a head-to-tail fashion and 10-15 of them then associate laterally to form a hollow cylinder.[1] *In vivo*, myriads of accessory binding proteins and signaling pathways for tubulin are known to regulate their formation, their non-equilibrium dynamics and thus to assist to fulfill their manifold cellular activities and functions.[2] Further, microtubule-associated proteins like tau and MAP2 are involved in inducing bundle formation of microtubules in order to grow and maintain neuronal projections.[3] *In vitro*, like-charge attraction between the negatively charged microtubules and formation of tightly packed hexagonal bundles have been observed in the presence of multivalent counterions (electrostatic condensation) and concentrated solutions of polymers (depletion attraction). [4,5] However, the chemical nature of the microtubule-microtubule interactions, which determines the size, the morphology and the mechanical resistance of the microtubule bundles, as well as the pressure stability of such bundles are largely unknown. In order to probe those microscopic interactions and their functional consequences, we carried out SAXS experiments and studied the quaternary structure of microtubule bundles as a function of pressure and crosslinking agent.

Pressure-dependent SAXS experiments were performed at the beamline BL9 of DELTA in a home-built pressure cell with diamond windows of 1 mm thickness (type IIa quality, Drukker, Cuijk, The Netherlands).[6] At BL9, the X-ray energy was 10 keV, which corresponds to a wavelength, λ, of 0.12 nm, and the sample-detector distance was 1.103 m (calibrated with a silver behenate control), covering a momentum transfer (q) range between 0.02 and 0.55 Å-1. The scattering curves were recorded using a MAR345 imaging plate (D = 345 mm with 100 µm pixel size) and the exposure time was 15 min.

Figure 1A shows that both, electrostatic and depletion forces, are able to induce the formation of microtubule bundles, which are packed into a hexagonal lattice as indicated by the Bragg peaks. The tightness of the hexagonal bundles increases with the valence of the counterion as well as the crowding density. When applying pressure, we observed a direct dissociation of the bundles into denatured oligomers of tubulin with the exception of spermidine-induced bundles, indicating that the pressure stability of the bundle phase is predominantly determined by the pressure limits of taxol-stabilized microtubules (Fig. 1B). In case of spermidine, pressurization up to 90 MPa induces a gradual dissociation of the bundles into individual microtubules, before those disintegrate completely at 150-165 MPa (Fig. 1C). This can be explained by the weakening effect of pressure on electrostatic interactions. In contrast, the charge density of the tetravalent cation spermine seems to be high enough to overcome the electrostrictive effect and to maintain the electrostatic condensation of the microtubules up to 150-165 MPa, where pressure causes complete disintegration of taxol-stabilized microtubules. Further, we found that the crowding effect induced by PEG elevates the pressure stability of microtubules to 180-195

MPa. In addition, pressure does not modulate the packing tightness before complete disintegration of the bundles into denatured oligomers.
Hence, our results clearly show that actin filaments and microtubules, as the most important components of the eukaryotic cytoskeleton, exhibit not only differences in the morphology and function, but also in the pressure stability. At 150 MPa, the upper limit of the physiologically relevant pressure range, when the microtubules and their bundles are completely disintegrated, actin filaments start to deform, and their dissociation is completed beyond 400 MPa only.[7]
Overall, the measurements carried out were very successful. A publication has already been submitted.

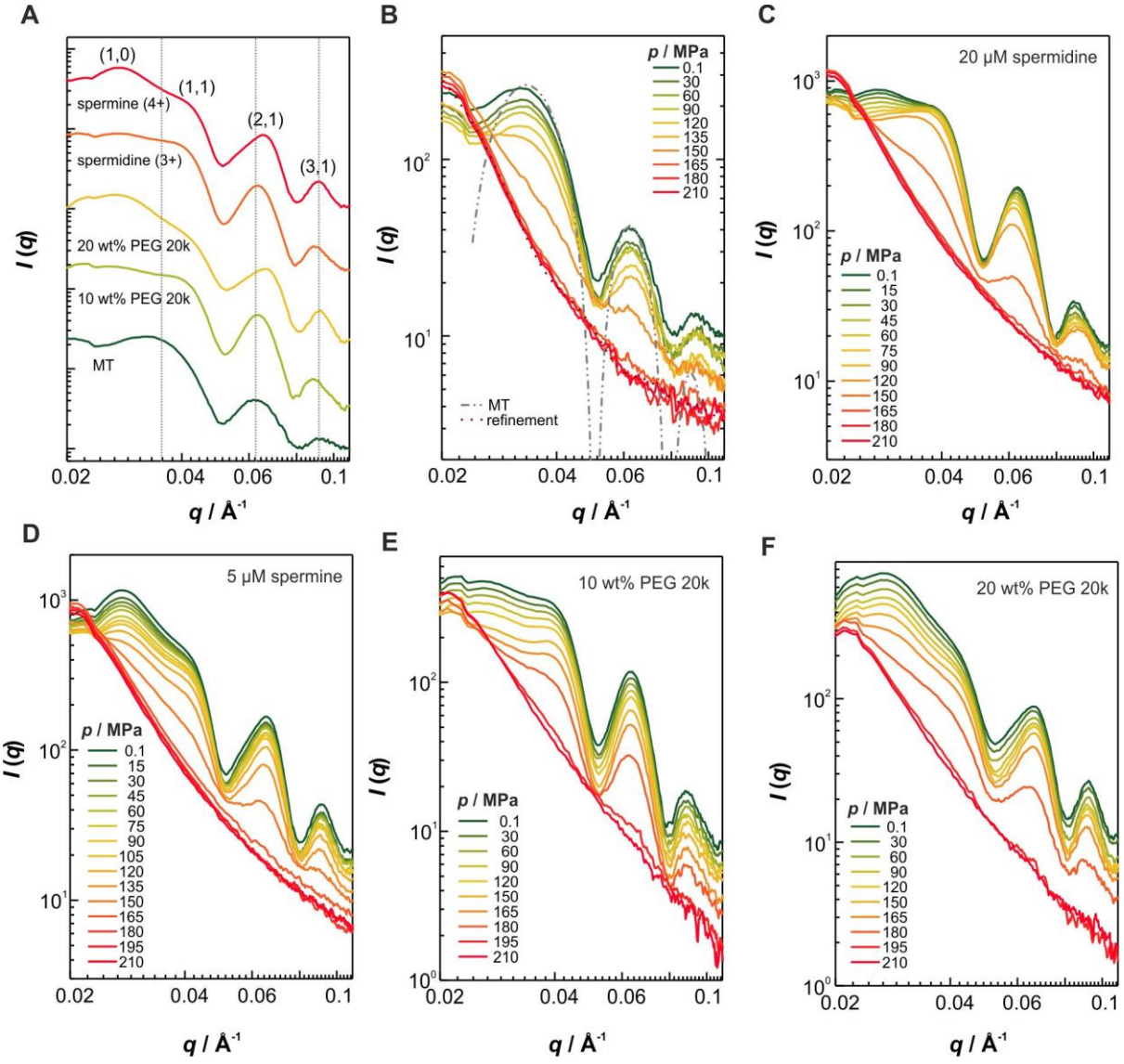

Figure 1: Pressure stability of microtubule bundles. (A) Synchrotron SAXS data of various bundle types of taxol-stabilized microtubules at 25 °C and atmospheric pressure. Pressure-dependent scattering profiles of (B) microtubules (MT) and their bundles induced by (C) 20 µM spermidine, (D) 5 µM spermine, (E) 10 wt% PEG 20k, and (F) 20 wt% PEG 20k.

[1] A. Desai, T. J. Mitchison, *Annu. Rev. Cell Dev. Biol.* **1997**, *13*, 83–117. [2] J. Howard, A. A. Hyman, *Curr. Opin. Cell Biol.* **2007**, *19*,31-35. [2] J. Howard, A. A. Hyman, *Curr. Opin. Cell Biol.* **2007**, *19*,31-35. [3] C. Conde, A. Cáceres, *Nat. Rev. Neurosci.* **2009**, *10*, 319–332. [4] D. J. Needleman, M. a Ojeda-Lopez, U. Raviv, H. P. Miller, L. Wilson, C. R. Safinya, *Proc. Natl. Acad. Sci. U. S. A.* **2004**, *101*, 16099-16103. [5] D. J. Needleman, M. A. Ojeda-Lopez, U. Raviv, K. Ewert, J. B. Jones, H. P. Miller, L. Wilson, C. R. Safinya, *Phys. Rev. Lett.* **2004**, *93*, 198104. [6] C. Krywka, C. Sternemann, M. Paulus, N. Javid, R. Winter, A. Al-Sawalmih, S. Yi, D. Raabe, M. Tolan, *J. Synchrotron Radiat.* **2007**, *14*, 244–251. [7] C. Rosin, M. Erlkamp, J. von der Ecken, S. Raunser, R. Winter, *Biophys. J.* **2014**, *107*, 2982-2992.

Temperature induced phase transition of polyethylenimine coated sodium borohydride for hydrogen storage

Robin Sakrowski[1], Christian Sternemann[1], Georgia Sourkouni[2], Wolfgang Maus-Friedrichs[2], Christos Argirusis[3], Jennifer Bolle[1], Jan Latarius[1], Florian Otte[1] and Metin Tolan[1]

[1] Fakultät Physik/DELTA, TU Dortmund, 44221 Dortmund, Germany
[2] Institut für Energieforschung und Physikalische Technologien, TU Clausthal, 38678 Clausthal-Zellerfeld, Germany
[3] School of Chemical Engineering, National Technical University of Athens, Zografou 15780, Athens, Greece

Native sodium borohydride ($NaBH_4$) does not meet all the requirements necessary for the industrial use as hydrogen storage material. The release rate of H_2 is to low and the cyclic reversibility is not always given [1]. Therefore, we prepared $NaBH_4$ powder samples with polyethylenimine (PEI) coating [2, 3] containing different catalysts like 5 wt% TiO_2 (nano, CV15 or CV16 Kronos®) and Ag with the aim to achieve a higher H_2 release rate at mild conditions around 100°C and a better. The aim of this experiment was the investigation of a temperature range of stability of $NaBH_4$ under vacuum conditions. Native $NaBH_4$ forms H_2 and stable $NaBO_2$ for temperatures above 290°C hence the influence of PEI and its catalysts is part of this study.

In this experiment, we used a 20 keV x-ray diffraction setup of BL9 with a MAR345 image plate detector and 350mm sample-detector distance. Heating the sample under vacuum (about 0.1mbar) was realised with the domed hot stage DHS 1100 by Anton Paar. The powder samples (1cm x 0.5cm x 0.5cm) were placed in the centre of rotation on top of a 1mm thin silver plate and heated from 30°C to 565°C. Five samples of $NaBH_4$ were investigated. Four of the samples were coated with PEI, three of those with additives. Quantitative phase analysis was performed with Rietveld refinement using MAUD© software by L. Lutterotti.

The results of a $NaBH_4$ sample with PEI + TiO_2 + Ag with respect to stability of $NaBH_4$ are shown in Fig. 1. The stabilizing effect of PEI coating could be demonstrated and the influence of different catalysts was analysed. All PEI coated samples showed a shifted temperature of decomposition about 35°C to 50°C towards higher temperatures. The most promising results are shown below where the sample was stable up to 340°C and showed just weak indication of oxidation at higher temperature regimes.
These results have to be combined with H_2 release rate data on additional methods like mass spectroscopy.

Reference:
[1] J. Mao and D. Gregory, *Recent Advances in the Use of Sodium Borohydride as a Solid State Hydrogen Store*, Energies 8.1, S.430-453 (2015).
[2] G. Sourkouni, F. Voigts, J.C. Namyslo, S. Dahle, W. Maus-Friedrichs, C. Argirusis, *Interaction mechanism of hydrogen storage materials with layer-by-layer applied protective polyelectrolyte coatings*, International Journal of Hydrogen Energy 39.27, S. 14834-14842 (2014).
[3] S. Dahle, J. Meuthen, M. Marschewski, A. Schmidt, W. Maus-Friedrichs, G. Sourkouni, Chr. Argirusis, *The influence of protecting polyelectrolyte layers on the temperature behaviour of $NaBD_4$*, RSC Adv. 4, S.2628-2633 (2014).

Acknowledgement

We would like to thank the DELTA machine group for providing synchrotron radiation and technical support.

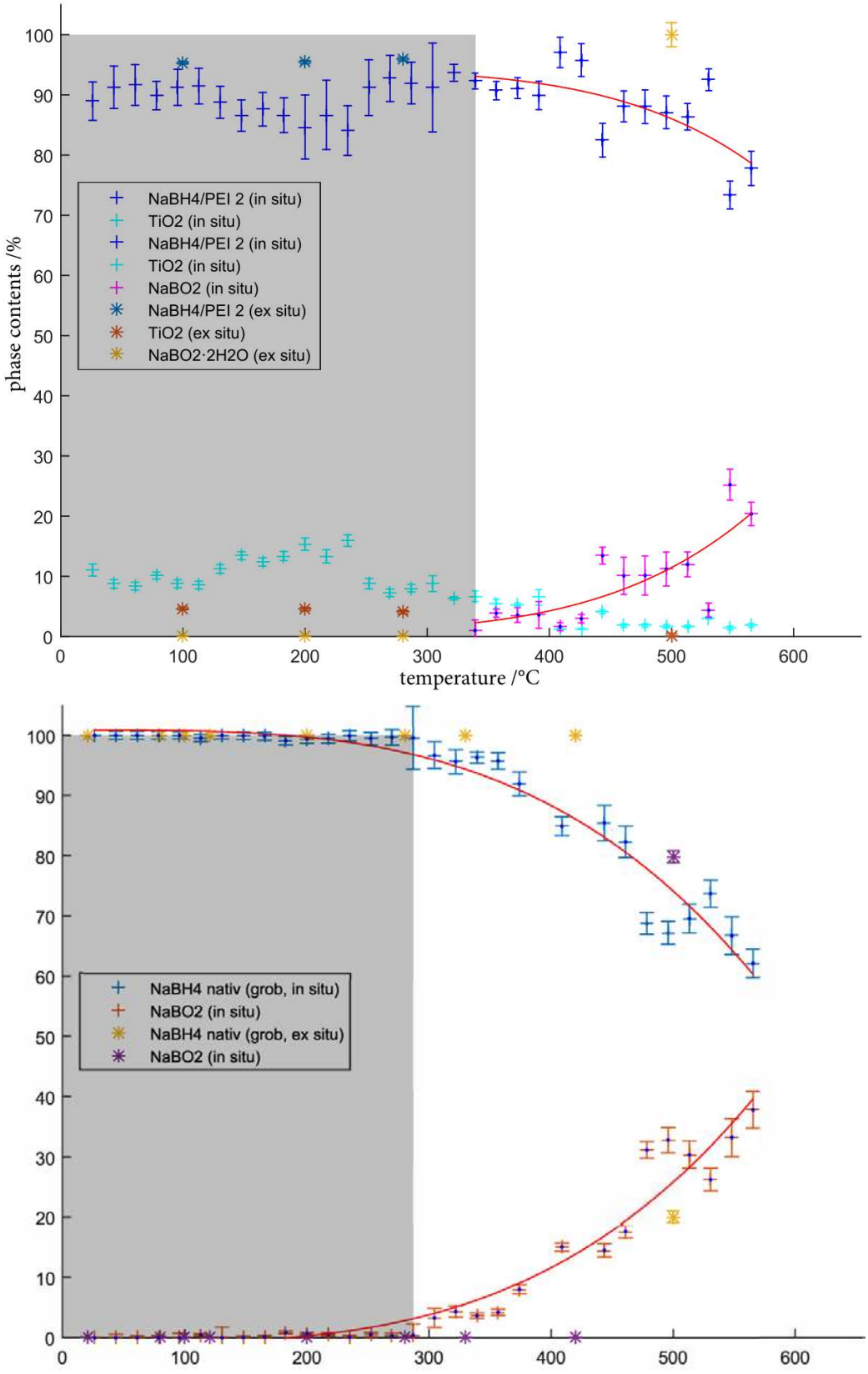

Fig.1 Top: Phase contents of $NaBH_4$ + PEI + TiO_2 (CV 16 Kronos®) + Ag. In situ data was measured in this experiment. No traces of Ag could be found. The grey box shows the temperature range where no $NaBO_2$ was detected. Bottom: For comparison the native $NaBH_4$ sample decomposes earlier and faster.

High pressure study of calmodulin-ligand interactions using small-angle X-ray scattering

Samy R. Al-Ayoubi,[a] Süleyman Cinar,[a] Christian Sternemann,[b] Claus Czeslik,[a] and Roland Winter[a]

[a] Department of Chemistry and Chemical Biology, TU Dortmund University, D-44221 Dortmund, Germany.

[b] Fakultät Physik / DELTA, Technische Universität Dortmund, D-44221 Dortmund, Germany.

Calmodulin (CaM) is a Ca^{2+} binding protein and involved in various signaling pathways, where it transforms a Ca^{2+} signal into protein activity. [1] Ca^{2+} bound CaM (holo-CaM) has a dumbbell shape, where the two lobes are connected by a flexible linker. Upon ligand binding, these lobes wrap around the ligand molecule to form a globular complex. One of the numerous binding partners of CaM is the protein KRas4B. The binding of KRas4B to CaM is mediated by its so called hypervariable region (HVR). This terminal peptide sequence contains 8 lysine residues, which are positively charged at neutral pH, as well as a hydrophobic farnesyl residue. In this study we used the HVR of KRas4B consisting of 12 amino acids. The second ligand used is the inhibitor trifluoperazine (TFP). In general, the binding of ligands to CaM is based on electrostatic and hydrophobic interactions. Both interactions are affected by pressure, consequently pressure application is a useful tool to obtain insights into the binding affinity of these ligands.

To this end we performed small angle x-ray scattering measurements at Beamline 9 of the DELTA synchrotron. The high pressure cell used was provided by the DELTA staff. [2] The raw data were integrated and converted to the wavevector transfer, Q, using the Fit2D program package.[3] Calibration was performed using a silver behenate standard. The data were corrected for the scattering from the pure buffer solution, which was measured at all pressure conditions. For data analysis the ATSAS software package was used. [4]

Selected results are depicted in figure 1. The pressure dependent development of $p(r)$ reveals small structural changes of holo-CaM upon pressurization, indicating a swelling of the lobes due to the penetration of water molecules. The symmetric pair-distance distribution function of the holo-CaM-TFP complex is characteristic for a globular shape. This complex structure is essentially unaffected by pressure application up to 3000 bar. The pair distance distribution function of the holo-CaM-KRas4B-peptide complex is also symmetric, the radius of gyration and the maximum diameter, however, are considerably larger than those of the holo-CaM-TFP complex. The holo-CaM-KRas4B complex is pressure stable up to 2400 bar. At 3000 bar however, structural changes are visible in the pair distance distribution, indicating a dumbbell like shape of the protein. A possible explanation of these findings is the formation of a dimeric complex at ambient pressure, which dissociates at 3000 bar. Similarly, a 2:2 dimer has been postulated previously for the CaM/calcineurine peptide complex. To this end we calculated scattering curves using crystal structure data of the dumbbell shaped holo-CaM, a globular shaped complex of holo-CaM with a myristoylated peptide and the calcineurine

dimer. As shown in figure 2, the experimental data can nicely be overlaid with the calculated SAXS curve of the dimer.

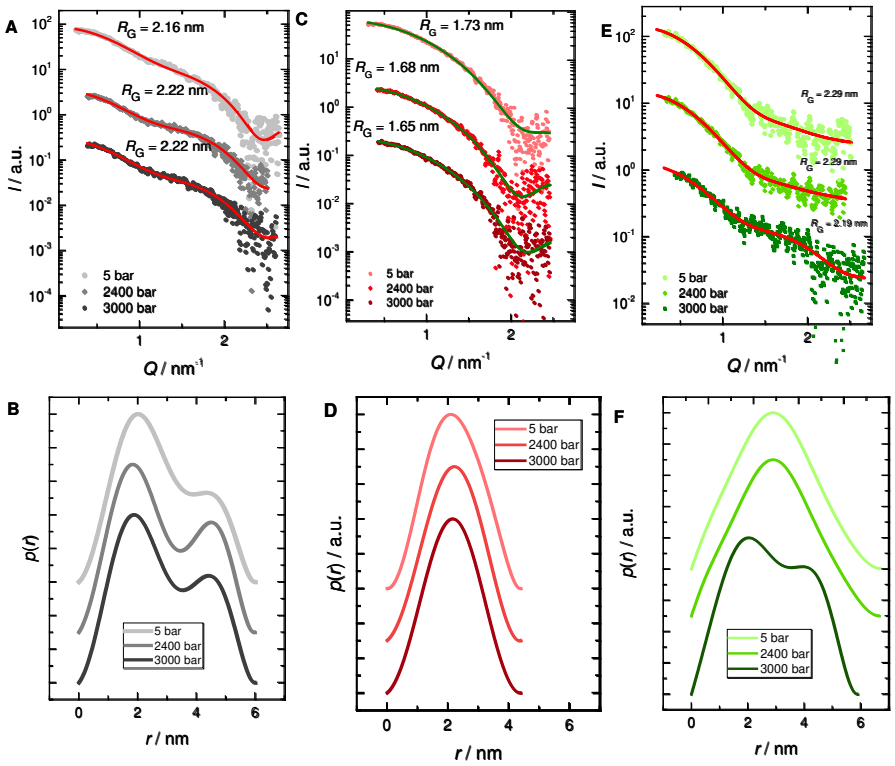

Fig.1: Background-corrected scattering patterns of 1 wt.% holo-CaM (A,B), holo-CaM + TFP (molar ratio: 1:5)(C,D) and holo-CaM + KRas4B (molar ratio: 1:1.5)(E,F), at selected pressure points. The solid lines represent fits, obtained by FT of the corresponding pair distance distribution functions shown below.

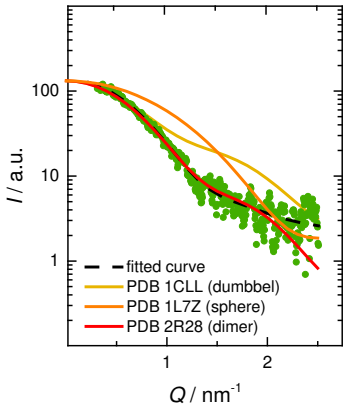

Fig. 2: Comparison of the experimental SAXS intensity of the holo-CaM/HVR complex at 5 bar with SAXS intensities calculated from PDB data of different crystal structures, using the program CRYSOL of the ATSAS package (solid lines).

[1] A. Kessel and N. Ben - Tal, Introduction to Proteins , CRC Press, Boca Raton, 2011.[2] C. Krywka, C. Sternemann, M. Paulus, M. Tolan, C. Royer and R. Winter, ChemPhysChem , 2008, 9 , 2809 - 2815 .[3] A. P. Hammersley, S. O. Svensson and A. Thompson, Nucl. Instr. and Meth . in Phys. Res. A , 1994, 346 , 312 - 321.[4] D. Franke, M. V. Petoukhov, P. V. Konarev, A. Panjkovich, A. Tuukkanen, H. D. T. Mertens, A. G. Kikhney, N. R. Hajizadeh, J. M. Franklin, C. M. Jeffries and D. I. Svergun, J. Appl. Cryst. , 2017, 50 , 1212 - 1225.

Tetrafluoroterephthalates (tF-BDC^{2-}) of composition M(II)tF-BDC · nH$_2$O with n = 0 for M(II) = Co, Zn and n = 2 for M(II) = Ni

C. Stastny, M. Werker and U. Ruschewitz*

Department für Chemie, Universität zu Köln, 50939 Köln, Germany

**email: uwe.ruschewitz@uni-koeln.de*

The dianion of terephthalic acid (1,4-benzenedicarboxylate, BDC^{2-}) is one of the linker ligands that is very frequently used for the synthesis of coordination polymers and well-known MOFs (metal-organic frameworks) like MOF-5[1] and MIL-53[2]. The formal replacement of hydrogen by fluorine in these linkers, i.e. formation of 2,3,5,6-tetrafluoroterephthalate ≡ tF-BDC^{2-}, should lead to coordination polymers and MOFs with new and exciting properties with respect to gas adsorption and separation. Already very early we have started to use tF-BDC^{2-} for the construction of new coordination polymers.[3-6] Using lanthanide cations as knots compounds with interesting luminescence properties were obtained.[5,6] As the knots of MOF-5 consist of Zn_4O^{6+} cores we also attempted to synthesize a possible perfluorinated MOF-5 analogue starting from different Zn^{2+} salts. But only the hydrate [Zn(tF-BDC)(H$_2$O)$_4$] was obtained, in which chain-like structural units of interconnected ZnO$_6$ octahedra were found.[4] However, the DTA/TGA data reveal a step-like mass loss, from which the formation of an anhydrous coordination polymer with composition [Zn(tF-BDC)] was concluded.[4] As isostructural hydrates with Co^{2+} and Ni^{2+} were obtained,[4] similar anhydrous coordination polymers with these 3d cations were also expected.

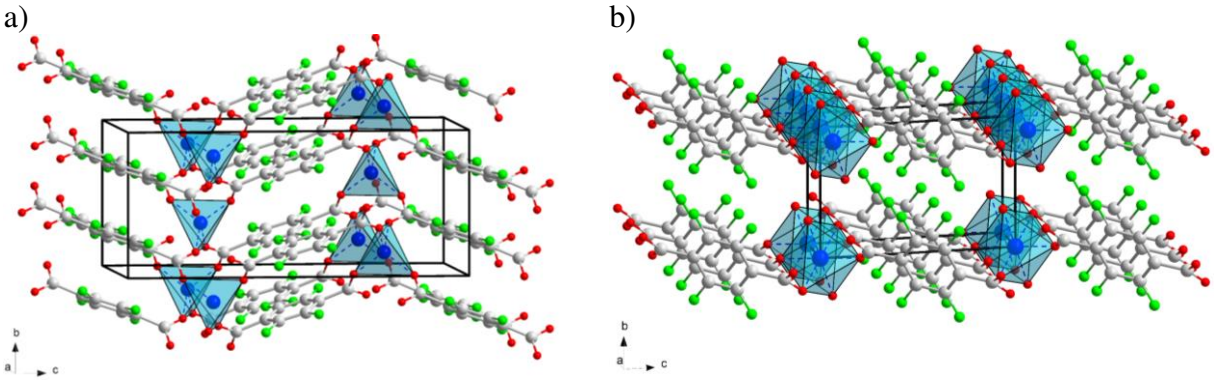

Figure 1: *a) Crystal structure of [Zn(tF-BDC)][4]; b) crystal structure of [Ni(tF-BDC)(H$_2$O)$_2$].*

To elucidate the crystal structure of [Zn(tF-BDC)] well resolved synchrotron powder diffraction data were recorded at BL9 with the *Pilatus100K* detector. Using real space methods[7] its crystal structure was solved and refined (Figure 2a)).[8] It is a remarkable feature of the crystal structure of [Zn(tF-BDC)] (*C*2/*c*, *Z* = 4) that the octahedral ZnO$_6$ coordination in [Zn(tF-BDC)(H$_2$O)$_4$] is changed to a tetrahedral ZnO$_4$ polyhedron (Figure 1a)). These ZnO$_4$ tetrahedra are interconnected by the tF-BDC^{2-} linkers to form a 3D framework structure. However, a van der Waals representation of the crystal structure reveals that [Zn(tF-BDC)] is

not porous. Upon heating slightly pink [Co(tF-BDC)(H_2O)$_4$] is transformed to a deep bluish compound (Figure 2b)), which turned out to be an isostructural analogue, namely [Co(tF-BDC)]. This colour change can be directly correlated to the changing coordination sphere, as confirmed by UV/vis spectra recorded in cooperation with Prof. Glaum, University of Bonn.

For [Ni(tF-BDC)(H_2O)$_4$] only a slight deepening of its green colour upon heating was observed. Again synchrotron powder diffraction data were recorded at BL9, from which the crystal structure could be solved and refined. Here, the dihydrate [Ni(tF-BDC)(H_2O)$_2$] ($P\bar{1}$, Z = 1) is formed, in which NiO_6 octahedra are connected by the tF-BDC^{2-} linkers to form a layer-like polymeric anion. Further heating leads to a decomposition of the coordination polymer, probably due to decarboxylation of the linker ligand. Thus, with decreasing water contents an increasing dimensionality of the resulting polymeric units is observed: 1D chains for [M(II)(tF-BDC)(H_2O)$_4$] with M(II) = Co, Ni, Zn; 2D layers for [Ni(tF-BDC)(H_2O)$_2$] and a 3D framework for [M(II)(tF-BDC)] for M(II) = Co, Zn.

a) b)

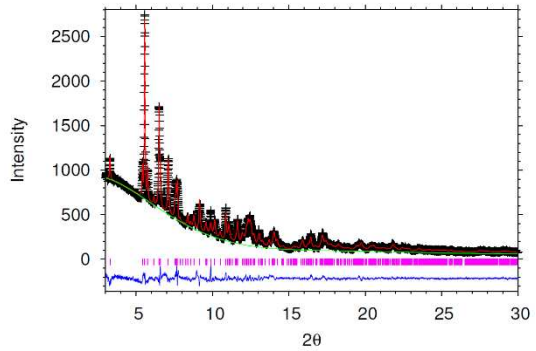

Figure 2: *a) Rietveld refinement of [Zn(tF-BDC)]; b) colour change of slightly pink [Co(tF-BDC)(H_2O)$_4$] to bluish [Co(tF-BDC)] upon heating.*

References

[1] H. Li, M. Eddaoudi, M. O'Keeffe, O. M. Yaghi, *Nature* **1999,** *402*, 276-279.

[2] T. Loiseau, C. Serre, C. Huguenard, G. Fink, F. Taulelle, M. Henry, T. Bataille, G. Férey, *Chem. Eur. J.* **2004,** *10*, 1373-1382.

[3] A. Orthaber, C. Seidel, F. Belaj, J. H. Albering, R. Pietschnig, U. Ruschewitz, *Inorg. Chem.* **2010**, *49*, 9350-9357.

[4] C. Seidel, R. Ahlers, U. Ruschewitz, *Cryst. Growth Des.* **2011**, *11*, 5053-5063.

[5] C. Seidel, C. Lorbeer, J. Cybinska, A.-V. Mudring, U. Ruschewitz, *Inorg. Chem.* **2012**, *51,* 4679-4688.

[6] M. Sobieray, J. Gode, C. Seidel, M. Poß, C. Feldmann, U. Ruschewitz, *Dalton Trans.*, **2015**, *44*, 6249-6259.

[7] Endeavour, version 1.7g, **2015**, Crystal Impact GbR.

[8] a) A. C. Larson, R. B. v. Dreele, *Los Alamos Laboratory, Rep. No. LA-UR* **1987**, *86*, 748; b) B. H. Toby, *J. Appl. Crystallogr.* **2001**, *34*, 210–213.

Tailoring Supramolecular Self-Assembly Prosperities of π-Systems by Conjugation with Oligoproline

Wojciech Zajaczkowski,[1] Tomasz Marszalek,[1,4,3] Urszula Lewandowska,[2] Helma Wennemers,[2] Klaus Müllen,[1] Wojciech Pisula[1,3,*]

[1] Max Planck Institute for Polymer Research, Ackermannweg 10, 55128 Mainz, Germany

[2] Laboratory of Organic Chemistry, ETH Zurich, Vladimir-Prelog-Weg 3, 8093 Zurich (Switzerland)

[3] Department of Molecular Physics, Faculty of Chemistry Lodz University of Technology, Zeromskiego 116, 90-924 Lodz (Poland)

[4] Organisch-Chemisches, Institut Ruprecht-Karls-Universitat Heidelberg, Im Neuenheimer Feld 270, 69120 Heidelberg (Germany)

* Email: pisula@mpip-mainz.mpg.de

During our beam time at the BL9 of the DELTA electron storage ring in Dortmund in 2016-2017 we continued investigation on the effect of structural modifications on the self-assembly of oligoprolines conjugated with sterically demanding chromophores (alkynylated perylene monoimides - PMI) (Figure 1). Spectroscopic (UV–vis and fluorescence) and microscopic (TEM) studies revealed hierarchical supramolecular self-assemblies with increasing length of the conjugate in H2O/THF mixtures, from worm-like threads via bundles of fibrils to nanosheets. The combination of wide-angle X-ray scattering (WAXS), UV–vis, and fluorescence spectroscopy of the nanostructures revealed J-aggregate formation by a ladder-like arrangement of the PMIs within the nanosheets. Additional small changes within the length and the stereochemistry of the peptide backbone have significant influence on the supramolecular self-assemblies of oligoprolines-PMI conjugates. Elongating the peptide chain beyond nine proline residues or introducing structural "errors" and significantly lowered the efficacy of self-assembly. These results have been recently published in Angew Chem Int Edit[1], Chemistry - A European Journal[2] and Nature Chemistry[3]

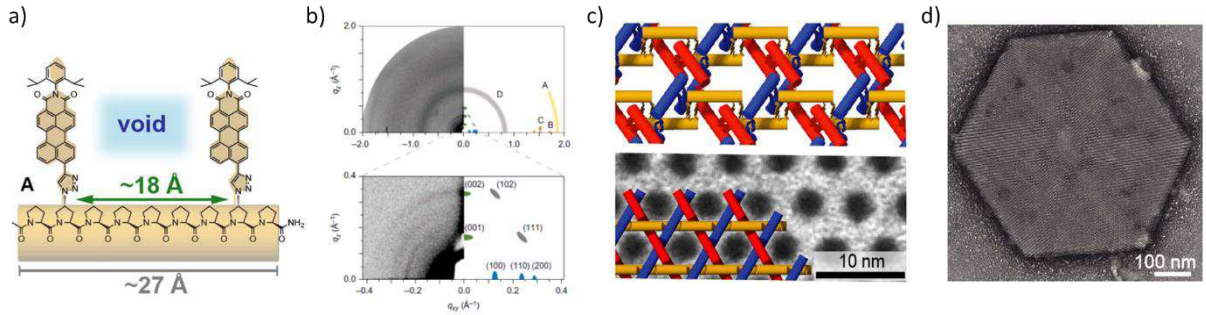

Figure 1. a) Structure of oligoproline-PMI conjugate A, b) GIWAXS pattern, c, d) TEM micrographs of the supramolecular assemblies deposited from THF/H2O (30:70) solutions.[3] Copyright 2017 Nature Publishing Group.

Based on previous observations of self-assembly properties of oligoproline-PMI conjugates, we extended the use of those conjugates to advanced topologies (Figure 1a). We noticed that getting rid one of the chromophores cause the system to retain the ability to undergo π–π stacking of the PMIs and to assemble into threads with alternating up-and-down voids at defined intervals. Initial spectroscopic (UV-vis) studies with modified conjugate, demonstrate self-assembles into a triaxial weave structure (Figure 1c,d). The self-assembly, which forms by a cooperative process in solution, extends into the micrometer regime and endows the nanoscopic material, similar to macroscopic woven materials, with mechanical strength and stability. Grazing incidence wide-angle X-ray scattering

(GIWAXS) provided a detailed insight into the molecular arrangement of conjugate within the superstructures (Figure 1b). Characteristic reflections distribution pbserved at small angle range confirm well-ordered trihexagonal network with a_{hex} = 56.4 Å. Wide-angle range, reflections at d-spacing of 3.70 Å and 3.41 Å, which are comparable to those previously observed for other oligoproline-PMI self-assemblies[1-2], arise from π-stacked chromophores that are perpendicular to the surface. Additional scattering maxima at the d-spacing of 4.11 Å is indicative of CH-π interactions between pairs of π-stacked chromophores from neighbouring strands at an angle of 60°. These additional weak CH-π interactions between the π-stacked PMI pairs help to establish the triangular structure of the connection points within the more advance network.

Acknowledgement

We are grateful for financial support by the VW foundation. The researchers involved in this project express their gratitude to Dr. Christian Sternemann and Dr. Michael Paulus for their help in the experiments.

References

1. Lewandowska, U.; Zajaczkowski, W.; Chen, L.; Bouilliere, F.; Wang, D. P.; Koynov, K.; Pisula, W.; Mullen, K.; Wennemers, H., Hierarchical Supramolecular Assembly of Sterically Demanding pi-Systems by Conjugation with Oligoprolines. Angew Chem Int Edit 2014, 53 (46), 12537-12541.
2. Lewandowska, U.; Zajaczkowski, W.; Pisula, W.; Ma, Y.; Li, C.; Mullen, K.; Wennemers, H., Effect of Structural Modifications on the Self-Assembly of Oligoprolines Conjugated with Sterically Demanding Chromophores. Chemistry 2016, 22 (11), 3804-9.
3. Lewandowska, U.; Zajaczkowski, W.; Corra, S.; Tanabe, J.; Borrmann, R.; Benetti, E. M.; Stappert, S.; Watanabe, K.; Ochs, N. A. K.; Schaeublin, R.; Li, C.; Yashima, E.; Pisula, W.; Mullen, K.; Wennemers, H., A triaxial supramolecular weave. Nat Chem 2017, 9 (11), 1068-1072.

Effect of tetramethylamine-chloride on lysozyme solutions

J. Latarius, J. Schulze, M. Paulus, M. Tolan

Fakultät Physik/DELTA, TU Dortmund, 44221 Dortmund, Germany

The influence of pressure on the protein-protein interaction potential in dense protein solutions was in the focus of scientific interest in recent years. Previous studies revealed a non-linear pressure dependence of the attractive part of the pair interaction potential $V(r)$ of lysozyme [1]. The addition of Trimethylaminoxid (TMAO) causes a shift of the minimum of the attractive part to higher pressures, while urea causes only a reduction of the protein-protein-attraction [2]. In order to gain a better understanding of the underlying mechanisms, we chose the salt tetramethylamine-chloride (TMACL) for comparison in our study.

Small-angle X-ray scattering (SAXS) is an ideal and well known technique for the investigation of non-crystalline solutions. In SAXS measurements, the scattered intensity I in dependence of the wave vector transfer $q=4\pi/\lambda \sin(\vartheta)$, with the scattering angle ϑ and the wavelength λ of the incoming beam, is detected. For low protein concentrations (e.g. 1 wt.% at moderate pH), the scattered intensity $I(q)$ corresponds to the form factor $P(q)$ of the particles. At high concentrations, the interaction between the proteins has to be considered and the structure factor $S(q)$ has to be multiplied with the form factor. In general, an increase of $S(q)$ at small q correspond to an attractive particle-particle interaction, while a decrease corresponds to an repulsive potential.

The pressure dependent SAXS experiments were performed at beamline BL 9 of DELTA with a photon energy of 10 keV with a custom-built high pressure cell.

Pressures between 50 and 4000 bar were applied to a solution containing 10 wt.% lysozyme and different concentrations of TMACL. Furthermore, 0.1 M BisTis buffer was used to stabilize the pH of the solution at high pressures.

Figure 1 shows the scattered intensity for different concentrations of TMACL at ambient pressure. The data is shifted for a better distinction. Especially at small q-values one can see the impact

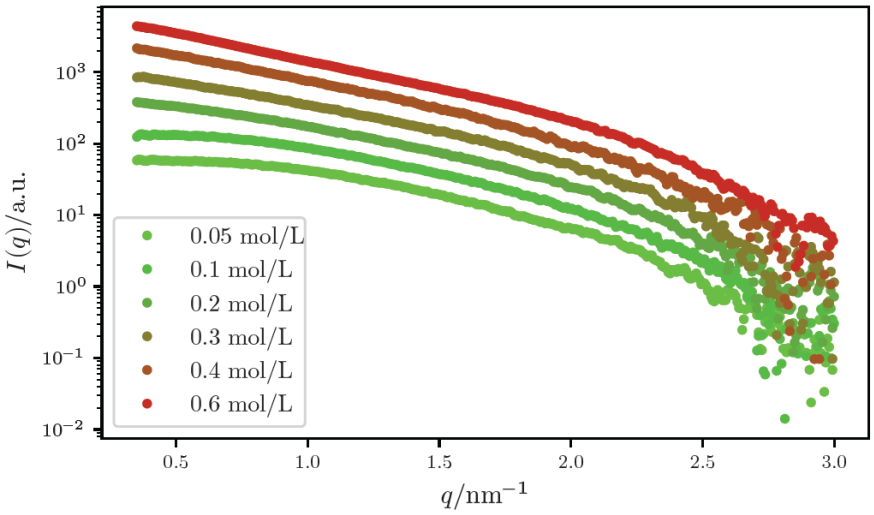

Figure 1. Scattered intensity for 10 wt.% lysozyme solution with different concentrations of TMACL. For a better distinction, the data is vertically shifted.

of increasing TMACL concentration. Adding TMACL leads to an increased scattered intensity at low *q*. One explanation might be a growing attractive interaction potential: the ions arrange around the proteins and screen the coulomb repulsion, leading to a protein-protein attraction. But, especially at very high ionic strengths, proteins tend to aggregate, also resulting in an increased scattering at low *q*. To verify one of the explanations or maybe determine the critical TMACL concentration, where aggregation can be observed, a careful analysis of the data has to be done. For instance, the analysis of form factors for different TMACL concentrations is in progress. Afterwards, the pressure dependent interaction potentials for different TMACL concentrations can be determined for all non-aggregated samples.

We would like to thank the DELTA machine group for providing synchrotron radiation and technical support.

References:

[1] Schroer, M.A. ; Markgraf, J. ; Wieland, D.C.F.; Sahle, Ch.J. ; Möller, J ; Paulus, M. ; Tolan, M. ; Winter, R.: Phys. Rev. Lett., 106(17), 2011, 178102.

[2] Schroer, M. A.; Zhai, Y.; Wieland, D. C. F.; Sahle, C. J.; Nase, J.;Paulus, M.; Tolan, M. and Winter, R.: Angew. Chemie , 50(48), 2011, 11413–11416.

A complex polymophism of polyquaterthiophene (PQT) thin films

S. Grigorian, [a], S. Escoubas, [b] D. Ksenzov, [a] D. Duche, [b] M. Aliouat, [b] J.-J. Simon, [b] B. Bat-Erdene, [a] S. Allard, [c] U. Scherf, [c] U. Pietsch, [a] O. Thomas [b]

[a.] *Department of Physics, University of Siegen, Walter-Flex-Strasse 3, D-57072 Siegen, Germany.*

[b.] *Aix-Marseille Université, Université Toulon, CNRS, IM2NP, Avenue Escadrille Normandie Niemen - Case 142, F-13397 Marseille, France*

[c.] *Macromolecular Chemistry and Institute for Polymer Technology, Bergische Universität Wuppertal, Gauss-Strasse 20, 42119 Wuppertal, Germany*

The organic semiconductors are the subject of intense research due to their wide range of low cost and environmentally friendly applications. Among them the most important trends are the organic light emitting diodes (OLEDs), organic solar cells and organic field effect transistors (OFETs) providing enhanced optoelectronic properties and improved current characteristics. The conjugated polymers are conducting macromolecules with large number of repeating units and in contrast to small molecules being easy soluble in most of common solvents. Therefore, the devices based on the conjugated polymers can be a low cost processed from solution or by printing technologies.

A favourable class of a thiophene-based conducting polymer providing relatively higher environmental stability is the poly(dedocylquaterthiophene) (PQT-12). The PQT-12 is one of the promising solution-processable organic polymers required for a high performance of the organic semiconductor material and designed to provide excellent solution process-ability as well as ability to self-assemble [1, 2]. Moreover, the PQT-12 provides a reasonable high field-effect mobility and a stability under ambient conditions [2] which can be further improved the substrate surface treatment and thermal annealing [3].

In the current work we present in situ studies of the PQT-12 films upon thermal annealing [4]. Two circles with different thermal budget were applied: during the first the PQT-12 film was step-wise heated up 90°C and back to the room temperature and revealed rather reversible changes. For the second circle with a higher thermal budget up to 140°C irreversible changes were monitored. These irreversible changes are related with modifications of two polymorphs existing in PQT-12. The behaviours of polymorphs are directly correlated to the electrical and the optical properties measured on same conducting channel as a function of the temperature.

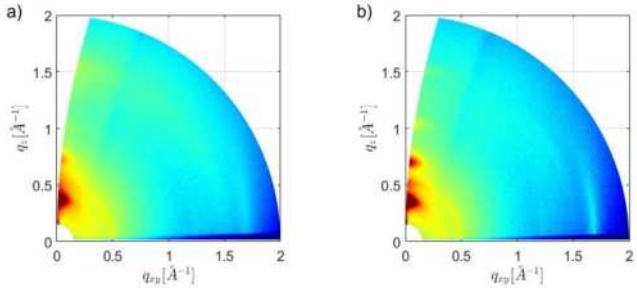

Fig.1. 2D GIXD patterns of the initial state at room temperature a) and annealed at 90°C of a drop-cast PQT-12 film.

In order to separate different types of thermal transitions we have applied two temperature circles for the PQT-12 film. During the first one, the sample was first heated step wise to 90°C and cooled down to the room temperature (RT). The 2D GIXD patterns for the first circle are shown in Figure 2; initial RT a), at 90°C b). A pronounced enhancement of the structure was found at the 90° C which mostly preserves after cooling back to RT. The second annealing circle has been applied to the sample right after first one when the sample reached the RT. Here the PQT-12 film was fast heated until 90°C, than further annealed with the similar steps of 10° C up to the melting temperature of 140°C. After keeping at melting temperature for 8 minutes, the sample was cooled back to the RT (the second thermal annealing cycle). Interestingly, the fast annealed film at the 90° C shows two distinguished polymorphs with the similar features to the film annealed at the 90° C and cooled back to RT after a first circle.

We found a complex correlation between the charge transport and the $\pi-\pi$ stacking performing in situ experiment [4]. The first thermal cycle improves both the conductivity and conjugation length. For the second thermal cycle at higher temperatures the induced disorder can significantly reduce the electric current. At the same time the second polymorph is almost melted at these temperatures. Further annealing cases a strong misorientation accompanied with decrease of the main form as well as two orders of magnitude reduction of the current. These findings support that that enhancement of the charge carrier is closely correlated with complex interplay between of two PQT polymorphs.

The report is based on ref. [4].

References:

[1] B. S. Ong, Y. Wu, Y. Li, P. Liu, and H. Pan, Chem. Eur. J. 14, 4766 (2008)

[2] B. S. Ong, Y. Wu, P. Liu and S. Gardner, J. Am. Chem. Soc. 126, 3378 (2004)

[3] L. Jimison, A. Salleo, M. Chabinyc, D. Bernstein, and M. Toney. Phys. Rev. B, 78, 125319 (2008).

[4] S. Grigorian, S. Escoubas, D. Ksenzov, D. Duche, M. Aliouat, J.-J. Simon, S. Allard, U. Scherf, U. Pietsch, O. Thomas, J. Phys. Chem C, DOI: 10.1021/acs.jpcc.7b02489 (2017)

The adsorption of lysozyme at the titanium dioxide - water interface

Yury Forov[1], Christian Albers[1], Irena Kiesel[2], Wiebke Schnettger[2], Tobias Gahlmann[3], Michael Paulus[1] and Metin Tolan[1]

[1]Fakultät Physik/DELTA, TU Dortmund, 44221 Dortmund, Germany
[2]Fakultät Chemie, TU Dortmund, 44221 Dortmund, Germany
[3]Bergische Universität Wuppertal, 42119 Wuppertal, Germany

The investigation of solid-liquid interfaces is one of the important areas of modern research. In particular, the adsorption of proteins and nanoparticles at liquid and solid surfaces is in the focus of actual research [1, 2]. Interfaces between liquids and solids, the solid-liquid interfaces, occur for example on implants in the body or in production facilities in the food industry. Especially in the case of the dental medicine, titanium with a TiO_2 layer on top is used as a preferred implant material. The study of the adsorption of proteins is in so far important as adsorbed proteins can initiate the formation of biofilms, which is usually resulting in unwanted consequences [3]. A biofilm on an implant surface may support the growth of bacteria, so that the risk of an inflammatory reaction rises [4]. Here, the use of high energy x-rays allows the analysis of buried interfaces and thin films in-situ by reflectivity measurements.

We measured the adsorption of lysozyme at the titanium dioxide - water interface as a function of different thermodynamic parameters. We varied the temperature between 20°C and 80°C, the pressure between 50 bar and 5000 bar and the pH-value between 2 and 12, respectively. The experiment was performed at beamline BL 9 using the high energy x-ray reflectivity setup and a temperature cell described in [2] as well as a high pressure cell described in [5]. The titanium dioxide surfaces were prepared by coating of silicon wafers with TiO_2 layers on top, gained by atomic layer deposition from $TiCl_4$ and H_2O. Afterwards, lysozyme was diluted in a phosphate buffer solution for the temperature and pH-value measurements as well as in a BisTris buffer solution for the pressure dependent measurements in a concentration of 1 mg/ml and given into the sample cell.

The temperature and pressure dependent reflectivity data and the corresponding electron density profiles, obtained by a refinement of the XRR data, are shown in figure 1 as a function of temperature. The electron density profiles demonstrate the adsorption behavior of lysozyme at the 75 Å thick TiO_2 layer, resulting in an additional layer above 75 Å. With rising temperature, the amount of adsorbed lysozyme increases significantly. To clarify this result, volume fraction profiles, also for the pressure and pH-value dependent measurements, have been calculated from the electron density profiles and are shown in figure 2.

Figure 2 shows the surface coverage as a function of the layer height. For increasing temperatures, the surface coverage increases from 13.9 % at 20°C to 15.85 % at 60°C. Further temperature increase leads to a creation of a second lysozyme layer. Since the denaturation temperature of lysozyme is at 71°C, the formation of a second lysozyme layer can be explained by denaturized lysozyme. However, the overall adsorption of lysozyme on TiO_2 is smaller than on SiO_2 (see reference [2]), which may be described by the higher surface charge of SiO_2 at a pH-value of 7. The analysis of the pH-value dependent measurements, which is still in progress, may support this thesis. Pressure dependent measurements show a desorption of lysozyme with rising pressures, which is almost

reversible by releasing pressure down to 50 bar again. Further analysis of this data is in progress.

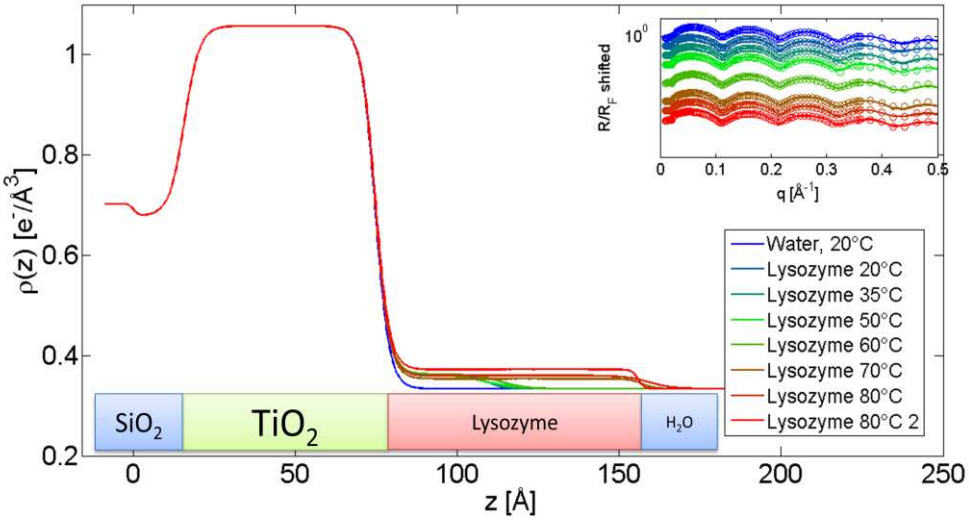

Figure 1: Electron density profiles of lysozyme on TiO_2 as a function of temperature. The XRR data is shown as inset in the figure.

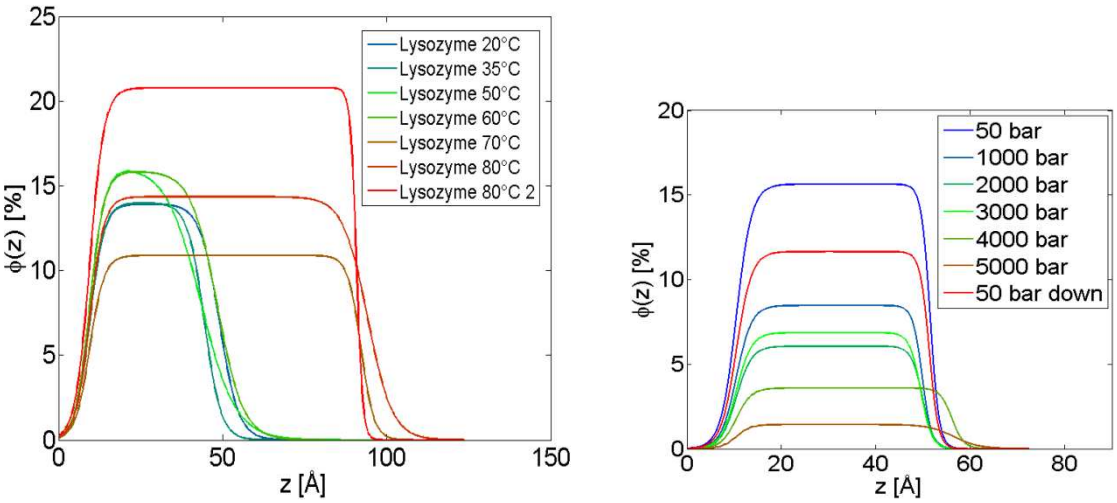

Figure 2: Volume fraction profiles as a function of temperature (left) and pressure (right) describing the covered wafer surface by lysozyme.

Acknowledgment:

The authors thank the DELTA machine group for providing synchrotron radiation. This work was supported by the Cluster of Excellence RESOLV (EXC 1069) funded by the Deutsche Forschungsgemeinschaft. PS acknowledges the DFG Forschergruppe 1979 for funding.

References:

[1] T. Brenner et al., J. Colloid Interface Sci., **374**, 287–290 (2012).
[2] I. Kiesel et al., Langmuir **30**, 2077 (2014).
[3] C. Czeslik, Chem. Unserer Zeit, **40** (4), 238–245 (2006).
[4] P. S. Stewart and J. W. Costerton, Lancet **358** (9276), 135–138 (2001).
[5] F. J. Wirkert et al., Journal of Synchrotron Radiation **21**, 76 (2014)

Hard X-ray spectroscopy

Sulfur K-edge XANES investigations of different rubber materials with and without aging

N. Hojdis[a], R. Wagner[b], A.-L. Dreier[a], F. Fleck[a], S. Balk[b], D. Lützenkirchen-Hecht[b]

[a]*Continental Reifen Deutschland GmbH, Jädekamp 30, 30419 Hannover, Germany*

[b]*Faculty 4 - Physics Department, Bergische Universität Wuppertal, Gauss-Str. 20, D-42119 Wuppertal, Germany*

Sulfur crosslinked rubber is used in a broad variety of applications, like seals, conveyer belts, O-rings or tires. For tire manufactures it is important to produce a long lasting product to survive in the competitive market. For further developments of tires it is thus crucial to understand the aging phenomena of rubber compounds in more detail. It is well known that the ratio between accelerator and sulfur determines the length of the sulfur chain building the crosslinks in the polymer network. A long chain length, the so called conventional vulcanization (CV), is produced by an excess of sulfur, while a short chain length (efficient vulcanization, EV), by an excess of accelerator, respectively. A semi efficient vulcanization (SEV) results from a sulfur/accelerator ratio close to 1. During the aging of the vulcanized polymer network, several processes are running in parallel. Beside chain scission by oxidation or radical reaction, the sulfur atoms of a crosslink are reorganized along the polymer chains. CV systems are going over SEV systems and EV systems. Macroscopically the rubber is getting hard and brittle. By conventional chemical methods of the rubber industry it is possible to determine the distance between crosslinks and observe the hardening effect during aging, but the structure (CV, SEV, EV) of the crosslinks cannot be measured directly. Therefore the investigation of reaction mechanisms during the aging process and the development of new anti-degradants is difficult. However recent work has shown, that X-ray absorption spectroscopy gives valuable information on the aging process of the formed structures during vulcanization processes [1, 2]. The main goal of this feasibility study was to reproduce the effects shown in previous experiments using the low-energy set-up of DELTA beamline 8 [3]. Making use of the InSb (111) monochromator and a windowless in-vacuum setup, unfilled natural rubber samples and a carbon black filled natural rubber sample, both vulcanized, have been investigated here by both transmission and fluorescence mode XANES spectroscopy at the S K-edge (2472 eV). Several spectra each of typically 15 minutes total integration time were averaged in order to obtain spectra of acceptable quality. To evaluate if the energy resolution is good enough to differentiate the sulfur chain length, two silanes have been measured, Bis [3-(triethoxysilyl) propyl] tetrasulfide and Bis [3-(triethoxysilyl) propyl] disulfide with four and two sulfur atoms, respectively. In addition the effect of three different aging conditions have been investigated: 2 days at 100 °C under air and under nitrogen atmosphere, as well as a mechanical aging procedure by cyclic deformation. This was done for the carbon black filled natural rubber compound with CV and EV systems.

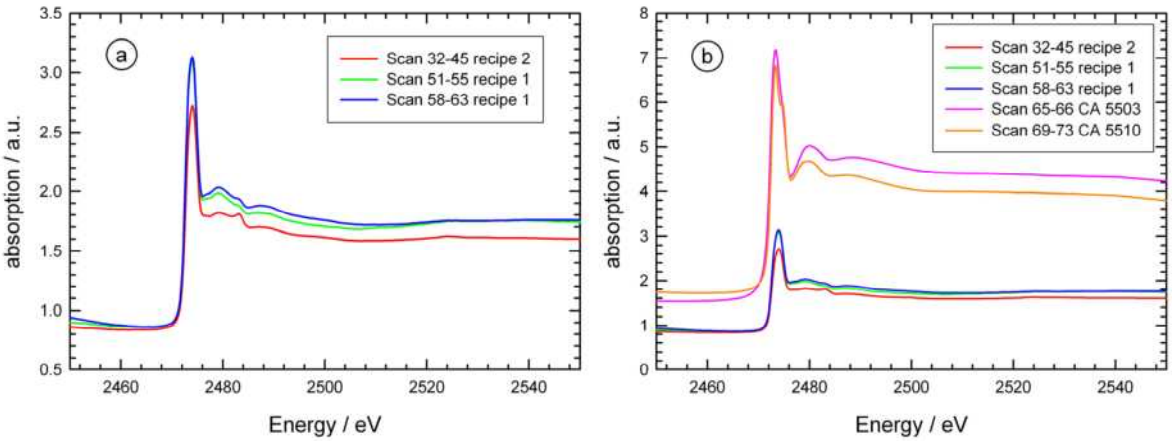

Fig. 1: (a) S K-edge XANES spectra of unfilled natural rubber compound (recipe 1) and a carbon black filled rubber compound with SEV system (recipe 2). (b) Comparison of the S K-edge XANES spectra of recipe 1 and 2 with pure Bis [3-(triethoxysilyl) propyl] tetrasulfide (sample CA 5503) and Bis [3-(triethoxysilyl) propyl] disulphide (sample CA 5510).

The measured XANES spectra from the first rubber samples in Fig. 1(a) are comparable to the reference sample 895 from ref. [1]. They show a pronounced white-line peak above the sulfur edge at around 2474 eV and

smaller peaks in the range from 2480 to 2500 eV, where several oxidation states of sulfur are expected. The spectra of Bis [3-(triethoxysilyl) propyl] tetrasulfide and Bis [3-(triethoxysilyl) propyl] disulfide in Fig. 1(b) also show a pronounced peak at the sulfur edge at around 2474 eV as expected. The silane structure with only two sulfur atoms shows an approaching shoulder at slightly larger photon energy which is in agreement with Fig. 4(a) from ref. [1] where the shoulder is only detectable for a single sulfur atom. As a consequence, the equipment at beamline 8 is able to reproduce the literature data [1], although the energy resolution provided by the InSb (111) monochromator is slightly larger compared to the instrumentation used in ref. [1], yet sufficient to conduct a reasonable interpretation of the measured X-ray absorption spectra. Thus a second sample set of samples consisting of two rubber compounds equipped with CV and EV systems respectively, aged under different conditions was investigated (Fig. 2).

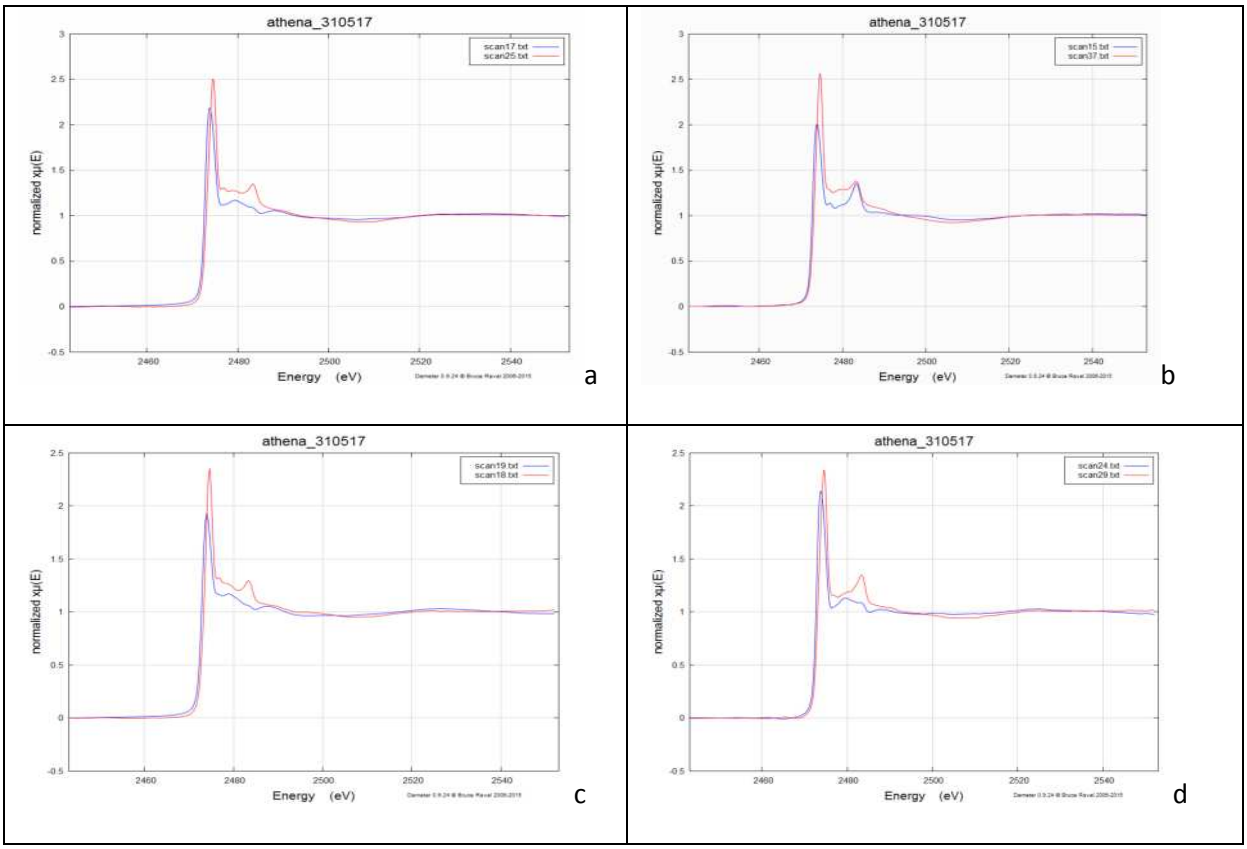

Fig. 2: XANES spectra of rubber samples aged under different conditions as indicated. Blue lines: CV system, red lines: EV system. (a) unaged samples, (b) samples aged 2 days under air, (c) samples aged 2 days under nitrogen, and (d) mechanically conditioned rubber samples.

All EV system samples (red curves) are slightly shifted towards higher absorption edge energies. This is in good agreement with figure 4a from [1] and supports the hypothesis that EV systems have shorter sulfur chains inside a crosslink compared to CV systems. All EV adsorption curves show a pronounced peak at around 2484 eV, which might be due to the oxidation of sulfur. In contrast the CV adsorption curves have this peak only visible for the sample aged under air, which further supports the presence of an oxidation effect. Also the unaged sample of the EV system shows oxidation effects – this is an interesting result which needs further investigation.

Acknowledgement

We gratefully acknowledge the DELTA machine group for providing synchrotron radiation reliably.

References

[1] H. Modrow, R. Zimmer, F. Visel, J. Hormes, Kautsch. Gummi. Kunstst. 53 (2000) 328.
[2] W. Pattanasiriwisawa, J. Siritapetawee, O. Patarapaiboolchai, W. Klysubun, J. Synchrotron Rad. 15 (2008) 510.
[3] D. Lützenkirchen-Hecht, R. Wagner, U. Haake, A. Watenphul, R. Frahm, J. Synchrotron Rad. 16 (2009) 264

EXAFS investigations of sol-gel derived GeO_2-nanoparticles

P. Rothweiler, R. Wagner, R. Frahm, D. Lützenkirchen-Hecht

Fakultät 4-Physik, Bergische Universität Wuppertal, Gaußstr. 20, 42097 Wuppertal, Germany

In recent years, nanoparticles of various different compositions have been prepared by hydrolysis of metal-organic compounds, in particular isopropoxides and alkoxides. For example, TiO_2, ZrO_2 and GeO_2 have been successfully synthesized [1, 2]. Usually, the precipitates obtained obey amorphous structures directly after hydrolysis, and thus a heat treatment is required to grow nanocrystalline materials, with typical temperatures ranging between 400 and up to 1000 °C [1-4]. GeO_2 is of particular interest because it is known to crystallize in various different crystal structures depending on pressure and temperature. Even at room temperature, two different stable modifications have been observed, i.e. the β-quartz type [5] and a rutile type [6], while for increasing temperatures the α-quartz phase exists [7, 8]. In addition, a so-called quartz-like phase also occurs [9]. In this contribution, we will address the structure of GeO_2-nanoparticles obtained by hydrolysis from Ge-isopropoxide $Ge(OCH(CH_3)_2)_4$. Hydrolysis was generally performed in de-ionized water at room temperature, and the obtained particles were investigated by EXAFS and XRD directly after drying as well as after a heat treatment in air at temperatures between 400 °C and 1000 °C for up to 24 h [10]. For comparison, samples were also prepared in conventional drinking water.

Ge K-edge EXAFS of the synthesized GeO_2 particles were measured in transmission mode at DELTA beamline 10 using a Si(111) channel-cut monochromator and ionization chambers as detectors [11]. The samples were homogeneously distributed on self-adhesive tape, and several tapes were stacked in order to obtain a sufficient absorption at the Ge-edge. The spectra were energy-calibrated to the edge of a Ge-reference sample (E = 11103 eV) which was simultaneously measured between the second a third ionization chamber. Several reference samples with well-defined structures, i.e. a Ge(111) single crystal, liquid $Ge(OCH(CH_3)_2)_4$ used for the hydrolysis and a GeO_2-sample were measured for comparison [10]. In Fig. 1, X-ray absorption near edge spectra of several Ge reference compounds as well as spectra of some selected samples are compared. As can be directly seen by comparison of the measured edge positions, all the synthesized Ge-nanoparticle samples obey a +4 valence state. Furthermore, in agreement with X-ray diffraction experiments, all the nanoparticles obtained from the hydrolysis showed a structure which is very similar to that of the crystalline GeO_2 reference directly after the hydrolysis. The crystallite size calculated from the width of the diffraction peaks is in the order of 30-50 nm, and was confirmed by scanning electron microscopic investigations. In contrast, previous investigations of GeO_2 nanomaterials prepared by sol-gel synthesis have shown that the particles are generally amorphous without a prolonged heat treatment to at least 675 - 770 °C [2]. However, the concentrations of the Ge-isopropoxide and the water were different in the latter study and may explain the observed differences.

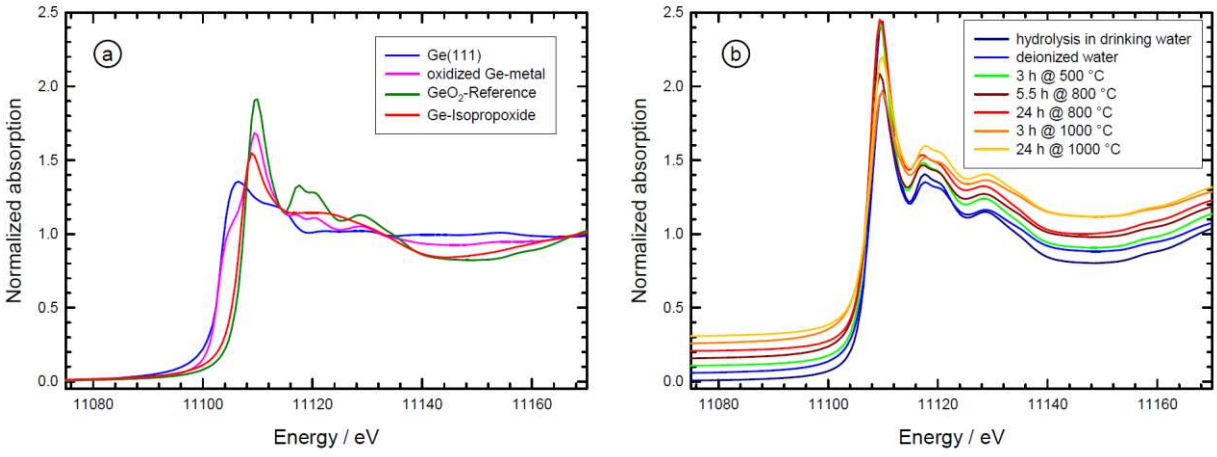

Fig. 1: (a) XANES spectra of Ge-reference samples, i.e. a Ge(111) single crystal, an oxidized polycrystalline Ge sample, GeO_2 and liquid Ge-isopropoxide $Ge(OCH(CH_3)_2)_4$. (b) Comparison of the Ge K-edge XANES spectra of some selected Ge-nanoparticle samples derived by hydrolysis as indicated.

The excellent quality of the EXAFS data obtained at beamline 10 allowed a detailed EXAFS analysis of the investigated Ge-nanoparticles. As can be seen in Fig. 2, almost noise-free EXAFS fine structure oscillations $\chi(k)*k^3$ could be measured up to k > 16 $Å^{-1}$, corresponding to a photon energy of about 1100 eV above the Ge K-edge. The magnitude of the Fourier-transform of the k^3-weighted EXAFS fine structure oscillations shows two prominent peaks at about 1.4 Å and ca. 2.8 Å, which are related to the first Ge-O and Ge-Ge coordinations in GeO_2 at 1.74 Å and 3.15 Å, respectively.

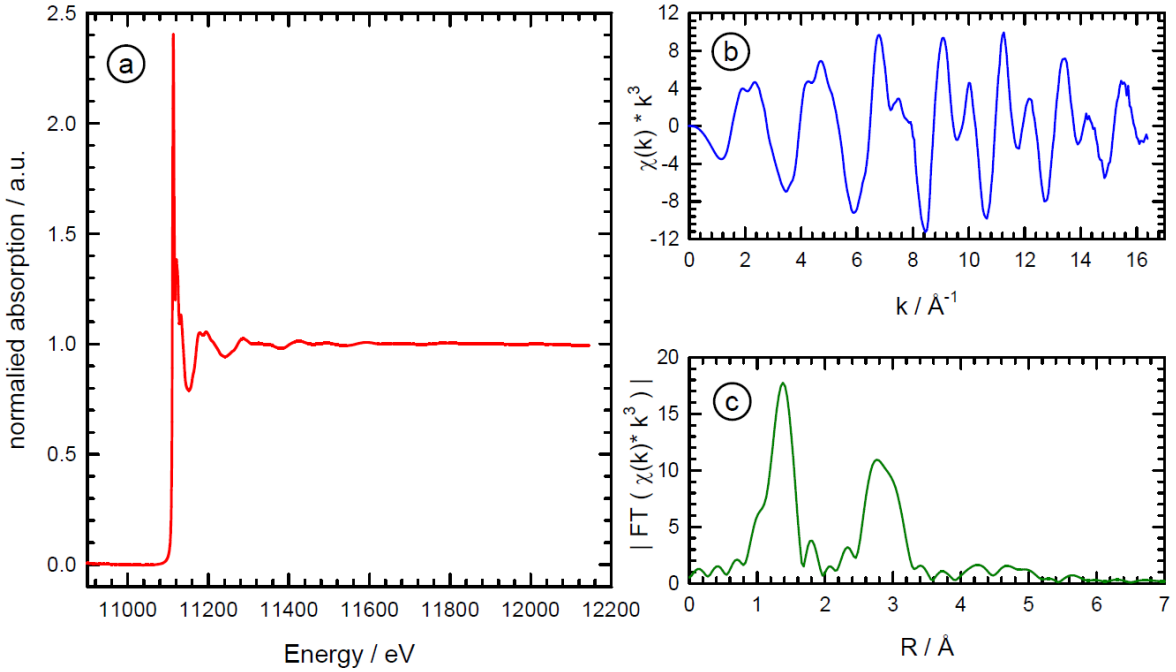

Fig. 2: Normalized Ge K-edge EXAFS spectrum of Ge-oxide nanoparticles obtained by hydrolysis of Ge-isopropoxide directly after drying but without any heat treatment. The extracted k^3-weighted EXAFS fine structures as well as the magnitude of the Fourier-transform | FT (c(k)* k^3) | are also displayed.

A more detailed evaluation of the XRD data and a modelling of the EXAFS may provide quantitative results for the different phases within the prepared nanosized Ge-materials [10]. The results of both techniques agree nicely, showing that contributions of the low-temperature β-quartz decrease substantially with increasing annealing temperature, while those of α-quartz and the quartz-like GeO_2 are increasing. In parallel, the size of the β-quartz particles decreased during annealing, while those of the two other phases show an increase with increasing annealing temperatures. However, no evidence for the rutile type GeO_2-phase were found in any of the samples.

Acknowledgement

We gratefully acknowledge the DELTA machine group for providing synchrotron radiation reliably.

References

[1] S. Mahshid, M. Askari, M. Sasani Ghamsari, J. Mater. Process. Technol. 189 (2007) 296.
[2] O. Yamaguchi, K. Kotera, M. Asano, K. Shimizu, J. Chem. Soc. Dalton Trans. (1982) 1907.
[3] S.J. Pfleiderer, D. Lützenkirchen-Hecht, R. Frahm, J. Sol-Gel Sci. Technol. 64 (2012) 27.
[4] M.Z.C. Hu, M.T. Harris, C.H. Byers, J. Colloid Interface Sci. 198 (1998) 87.
[5] J. D. Jorgensen, J. Appl. Phys. 49 (1978) 5473.
[6] A.W. Laubengayer, D.S. Morton, J. Amer. Chem. Soc. 54 (1932) 2303.
[7] W.H. Zachariasen, Z. Krist. 67 (1928) 226.
[8] J. Glinnemann, H.E. King, H. Schulz, T. Hahn, S.J. la Placa, F. Dacol, Z. Krist. 198 (1992) 177.
[9] G. S. Smith, P. B. Isaacs, Acta Cryst. 17 (1964) 842.
[10] P. Rothweiler, Bachelor-thesis. Bergische Universität Wuppertal (2017).
[11] D. Lützenkirchen-Hecht, R. Wagner, S. Szillat, A.K. Hüsecken, K. Istomin, U. Pietsch, R. Frahm, J. Synchrotron Rad. 21 (2014) 819.

EXAFS investigations of atomically dispersed Fe/B/N-doped porous carbon for oxygen reduction reactions

K. Yuan[a,b] S. Sfaelou[c], U. Polnick[c], X. Zhuang[c,e], D. Lützenkirchen-Hecht[d], T. Hu[a], Y. Chen[a], U. Scherf[b], X. Feng[c]

[a]*College of Chemistry/Institute of Polymers, Nanchang University, 999 Xuefu Avenue, Nanchang 330031, China.*
[b]*Macromolecular Chemistry Group and Institute for Polymer Technology, Bergische Universität Wuppertal, Gauss-Str. 20, D-42119 Wuppertal, Germany.*
[c]*Center for Advancing Electronics Dresden (cfaed) and Department of Chemistry and Food Chemistry, Technische Universität Dresden, Mommsenstrasse 4, 01062 Dresden, Germany.*
[d]*Faculty of Mathematics and Natural Sciences-Physics Department, Bergische Universität Wuppertal, Gauss-Str. 20, D-42119 Wuppertal, Germany*
[e]*Shanghai Key Laboratory of Electrical Insulation and Thermal Ageing, School of Chemistry and Chemical Engineering, Shanghai Jiao Tong University, Dongchuan Road 800, 200240 Shanghai, China*

Electrocatalysts based on noble metals such as gold and platinum and alloys such as PtAu exhibit a prominent activity for the oxygen reduction reaction (ORR) [1, 2]. However, their use in large-scale applications is hampered by their extremely high cost and scarcity [3]. Furthermore, noble-metal-based electrocatalysts are sensitive to CO poisoning and may suffer from crossover induced deactivation as well as from insufficient durability caused by dissolution, migration, detaching and leaching [4]. Therefore, noble-metal-free electrocatalysts are of fundamental importance for realizing practical and large-scale applications of fuel cells and metal-air batteries, not only because of economical reasons. In this context, both transition metal as well as carbon based materials have attracted increasing interested in the past few years [5-7].

Recent studies have shown that carbon materials such as graphene and carbon nanotubes doped with nitrogen could be an efficient, low-cost alternative to Pt for the ORR [8, 9], and co-doping those nitrogen doped carbon materials with a second heteroatom such as boron, phosphorus or sulphur can further boost the ORR activity [10, 11]. Furthermore, introducing transition metals like Fe and Co into N-doped carbon materials may additionally improve the performance for the ORR, because the incorporated metal and nitrogen atoms could form highly active catalytic sites M-N-C (M=Fe, Co) that significantly facilitate oxygen adsorption and reduction [12, 13].

In this contribution, we want to elucidate the structure of Fe, N and B co-doped FeBNC catalysts. The catalyst samples were obtained by adding a pyrrole monomer into a boric acid (H_3BO_3) solution (0.5 mM in ethanol/water). The iron source was a solution of $FeCl_3$ dissolved into a second boric acid solution. Both solutions were quickly mixed together under cooling to temperatures below 5 °C. After aging for 24 h, the obtained polypyrrole (PPy) hydrogel was purified with deionized (DI) water and freeze-dried, followed by annealing in an argon atmosphere for 2h at a heating rate of 5 °C/min. The subsequent pyrolysis was tested at various temperatures between 600 °C and 1000 °C in order to identify the optimum preparation conditions for the Fe-, B- and N- co-doped porous carbon (FeBNC) catalysts. The pyrolyzed products were finally leached in 1 M H_2SO_4 solution for 8 h at 80 °C, washed with deionized water, and then dried under vacuum. For the preparation of a Fe- and N-doped carbon catalyst, the hydrogel was prepared in water/ethanol mixtures, i.e. without using boric acid. In this report, we will focus on two samples, namely FeBNC-800 and FeNC-800. The samples contained a total trace amount of iron of about only 0.1 at. %.

X-ray absorption spectroscopy (XAS) experiments were carried out at the wiggler beamline BL10 at the DELTA storage ring (Dortmund, Germany) operated with 80-130 mA of 1.5 GeV electrons [14]. Fe K-edge spectra were collected using a Si(111)-channel cut monochromator and gas-filled ionization chambers as detectors for the incoming and the transmitted intensities, and a large area photodiode for the fluorescence photons. The powder samples were homogeneously distributed on self-adhesive tape, and several tapes were stacked in order to obtain a sufficient absorption at the Fe-edge, so that transmission mode experiments were feasible despite the small concentration of the element of interest. For comparison, a metal Fe-foil as well as several Fe-reference compounds such as Fe α-Fe_2O_3 (hematite), α-FeOOH (goethite), FeO, Fe_3O_4 (magnetite), $Fe(OH)_2$, FePc (Fe-phthalocyanine $C_{32}H_{16}FeN_8$) and Fe_3C were measured.

In Fig. 1(a), the X-ray absorption near edge structure (XANES) data obtained for the two Fe-containing samples are compared to reference spectra of FePc, Fe_3C and an iron foil. As can be seen, the edge position for the

FeBNC-800 and FeNC-800 are substantially different, indicating that the chemical valence of Fe and accordingly the local atomic environment around Fe in the two samples is non-equivalent. While the FeBNC-800 sample is similar to FePc, the FeNC-800 sample more behaves like oxidized iron or FeO. Similarly, also the radial distribution function in Fig. 1(b) is different for the two samples. Both samples show contributions of Fe-N at about 1.5 Å in the FT, Fe-Fe-contributions at about 2.4 Å, and Fe-C-contributions at about 3 Å as indicated by dashed vertical lines in Fig. 1(b). However, the intensities of the individual contributions differ substantially, i.e. the FeBNC-800 provides substantially more Fe-N bonds in comparison to FeNC-800, while the Fe-Fe signals are much larger for FeNC-800. The reduction of Fe-Fe bonds indicate that dispersion of the iron species in the FeBNC-800 sample is higher compared to the FeNC-800 sample, and furthermore a higher level of catalytically active Fe-N_x species is contained in the porous carbon framework of FeBNC-800 accordingly.

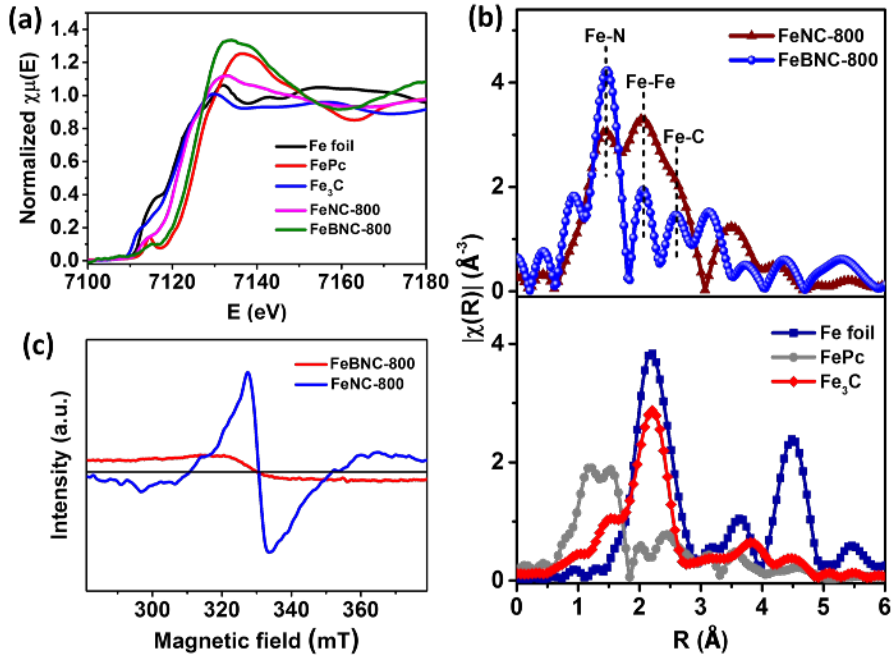

Fig. 1: (a) Fe K-edge X-ray absorption near edge structure (XANES) spectra for FeBNC-800 and FeNC-800 samples, and FePc, Fe_3C and an iron foil for comparison. (b) Magnitude of the Fourier transforms of the k^2-weighted EXAFS fine structure oscillations |FT (χ(k)*k^2)| for FeBNC-800 and FeNC-800 samples in comparison to FePc, Fe_3C and an iron foil. (c) Room temperature (273 K) EPR measurements for FeBNC-800 and FeNC-800 samples.

Acknowledgement

We gratefully acknowledge the DELTA machine group for providing synchrotron radiation reliably.

References

[1] M.S. Chen, D.W. Goodman, Catal. Today 111 (2006) 22.
[2] J. Zhang, K. Sasaki, E. Sutter, R.R. Adzic, Science 315 (2007) 220.
[3] M. Li, Z. Zhao, T. Cheng, A. Fortunelli, C.Y. Chen, R. Yu, Q. Zhang, L. Gu, B.V. Merinov, Z. Lin, E. Zhu, T. Yu, Q. Jia, J. Guo, L. Zhang, W.A. Goddard, Y. Huang, X. Duan, Science 354 (2016) 1414.
[4] Z. H. Xia, L. An, P. K. Chen, D. G. Xia, Adv. Energy Mater. 6 (2016) 1600458.
[5] J. Zhang, Z. Xia, L. Dai, Sci. Adv. 1(2015) e1500564.
[6] M. Zhou, H.L. Wang, S. Guo, Chem. Soc. Rev. 45 (2016) 1273.
[7] C. Tang, Q. Zhang, Adv. Mater. 29 (2017) 1604103.
[8] Y. Li, W. Zhou, H. Wang, L. Xie, Y. Liang, F. Wei, J.-C. Idrobo, S. J. Pennycook, H. Dai, Nature Nano 7 (2012) 394.
[9] H. Cui, Z. Zhou, D. Jia, Mater. Horiz. 4 (2017) 7.
[10] Y. Meng, D. Voiry, A. Goswami, X. Zou, X. Huang, M. Chhowalla, Z. Liu, T. Asefa, J. Am. Chem. Soc. 136 (2014) 13554.
[11] Z.X. Pei, H.F. Li, Y. Huang, Q. Xue, Y. Huang, M.S. Zhu, Z.F. Wang, C.Y. Zhi, Energy Environ. Sci. 10 (2017) 742.
[12] A. Zitolo, V. Goellner, V. Armel, M.T. Sougrati, T. Mineva, L. Stievano, E. Fonda, F. Jaouen, Nature Mater. 14 (2015) 937.
[13] U.I. Kramm, I. Herrmann-Geppert, J. Behrends, K. Lips, S. Fiechter, P. Bogdanoff, J. Am. Chem. Soc. 138 (2016) 635.
[14] D. Lützenkirchen-Hecht, R. Wagner, S. Szillat, A.K. Hüsecken, K. Istomin, U. Pietsch, R. Frahm, J. Synchrotron Rad. 21 (2014) 819.

Effect of lanthanide-doping on induced crystallization in ZBLAN glass

M. Al Humadi, U. Pietsch – Uni Siegen; C. Rimbach, St. Schweizer FH Soest

Owing to the non-crystalline structure of glass forming materials, their physical properties are less predictable but need extensive investigations of structure-to-property relations. It is well-known that the thermodynamic properties of pure glass can be scaled in terms of local structure and topology. Application of these concepts to glass ceramics is less known and it will be interesting to investigate whether the topology of glass phase can influence size and distribution of the diluted crystallites. In this study we made first investigation to improve the understanding of structure-to-property relations in ZBLAN glasses and glass ceramics and their impact on quantum efficiency of glass ceramics. The glasses are additionally doped with one, two trivalent lanthanides ions for optical activation. The main question to be answered is whether the lanthanide ions are diluted within or outside the thermally-induced crystallites. Lanthanide ions within the crystallites will be affected by a stronger crystal field as compared to those diluted within the glass matrix. Both will differently affect the absorption and emission properties of the lanthanide ions, namely the energy transfer between the host (glass / glass ceramics) and the lanthanide ion as well as the energy transfer from one lanthanide ion to another. To do so we performed preliminary EXAFS and XRD diffraction experiments at 3 different glass samples doped with 0.5 mol% Tb_4O_7, (sample A), with 1.0 mol% Eu_2O_3 (B) and 0.5 mol% Dy_2O_3 (C). For EXAFS measurements in transmission we used the setup of University of Wuppertal at BL10. XRD measurements have been performed at same station using the diffraction setup of Uni Siegen and a PILATUS100 detector. In order to prepare for XRD a small piece of glass was grinded to a powder and deposited between two kapton foils. For EXAFS we used a thin piece of compact glass.
Fig. 1 shows exemplarily the raw EXAFS data of samples A. As found for the other two samples it demonstrates well resolved spectra ready for further data analysis

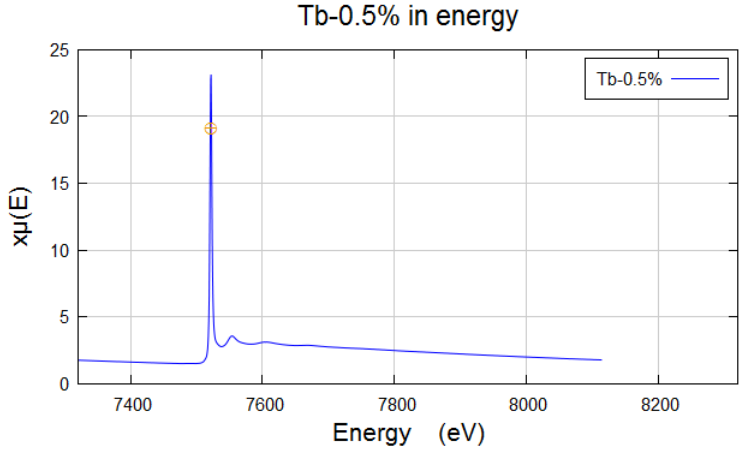

Fig.1 Raw EXAFS spectrum of ZBLAN Glass doped with Tb

At same time the XRD pattern did not show any Bragg peak confirming the amorphous phase of the samples. The data are currently under evaluation by a Master student. Both partners (FH Soest and FKP at University of Siegen) have submitted a common DFG project. Based on this ongoing collaboration the experiments at DELTA BL10 will be continued.

Chlorine speciation and co-ordination in Na_2O-Al_2O_3-SiO_2 glasses

Stephanie M. Thornber, Martin C. Stennett, and Neil C. Hyatt

NucleUS Immobilisation Science Laboratory, Department of Materials Science and Engineering, The University of Sheffield, Mappin Street, Sheffield, S1 3JD, UK.

Scientific motivation

The UK holds a stockpile of more 120 tons of separated civil plutonium, which will increase to over 140 tons at the end of nuclear fuel reprocessing in 2020. Up to 10% of this stockpile is likely to be declared as waste since it is unsuitable for fabrication as mixed $(U,Pu)O_2$ fuel for use in light water reactors (due to contamination by Fe, Cr, Am, Cl). We are currently developing glass-ceramic materials for immobilisation of this waste plutonium. In these materials, a crystalline ceramic phase, $CaZrTi_2O_7$ – zirconolite, incorporates Pu in solid solution by crystallisation from an aluminoborosilicate glass phase (which incorporates the contaminants). The glass phase in our glass-ceramic materials is based on the albite composition: $Na_2Al_2Si_6O_{16}$. The glass-ceramic material is typically 30wt% glass. A significant quantity of waste plutonium is contaminated by chlorine (up to 3 wt%, from degradation of PVC packaging) which poses a challenge for immobilisation in glass ceramic materials due to the limited solubility in alumina-borosilicate glass (typically <1 mol%). Above the solubility limit, we observe separation of a water-soluble chloride-salt phase, which can incorporate Pu and Am. Clearly, this is not desirable for geological disposal. Using EPMA, we have determined that the Cl solubility limit is strongly dependent on glass composition and have confirmed that that Cl is incorporated only within the glass phase.

We wish to use Cl K-edge X-ray Absorption Spectroscopy to understand how Cl solubility is controlled by speciation and local environment, as a function of chlorine loading This knowledge will enable us to construct a molecular model of chlorine incorporation within the glass structure which will provide evidence to support a future safety case for production of plutonium glass-ceramics, by defining the limit of chlorine concentration in the feed material (to avoid exceeding the Cl solubility limit and formation of water soluble chloride salts).

Experimental

All samples were batched with the same starting formulation, comprising 30 wt% glass with composition $Na_2Al_2Si_6O_{16}$, and 70 wt% ceramic forming oxides. Chlorine additions (as NaCl) were made to the batches on a wt% basis. Powder samples were prepared by milling the starting precursors which were then calcined at 600 °C before being packed into stainless steel cans and hot isostatically pressed (HIPed). Representative material was recovered from the HIP cans, powdered, and prepared into fluorescence samples for measurement at the Cl L_3 absorption edge. The powdered material was dispersed into a polyethylene glycol matrix and cold uniaxially pressed to yield thin but strong pellets; the exact quantity of specimen powder to achieve one absorption length was used. Data was also acquired on a range of standard materials to assist in finger-printing of the Cl oxidation state and coordination environment. This process was performed in an argon atmosphere glovebox to prevent hydration of the standards. Analysis was performed using the Athena

program. The X-ray absorption near edge structure (XANES) was analysed to qualitatively identify and compare characteristic features to infer the average Cl oxidation states and co-ordination environment.

Results

The Cl K-edge XANES data compared with the standards are shown in figure 1. The edge positions for all the samples are consistent with the Cl being present in the structure as a anion (Cl^-) however subtle changes are evident from inspection of the oscillations in the XANES region. At low levels of Cl incorporation the shape of the XANES is similar to that of $CaCl_2 \bullet 2H_2O$ and anhydrous $CaCl_2$. As the level of chlorine incorporation increases the shape changes to resemble that of the mineral Marialite and above 3.0 wt% NaCl. This suggests changes in the local structural environment from three cation nearest neighbours in trigonal bipyramid geometry at low Cl concentration (as in $CaCl_2$), to four cation nearest neighbours in tetrahedral geometry (as in Marialite). Above 3.0 wt% loading the XANES features of NaCl are present at 2835.5 which may indicate some precipitation of a NaCl structured phase where the Cl is bonded to six next nearest neighbour cations. The presence of free NaCl was not observed in the SEM images although this needs to be revisited with a more sensitive microstructural probe.

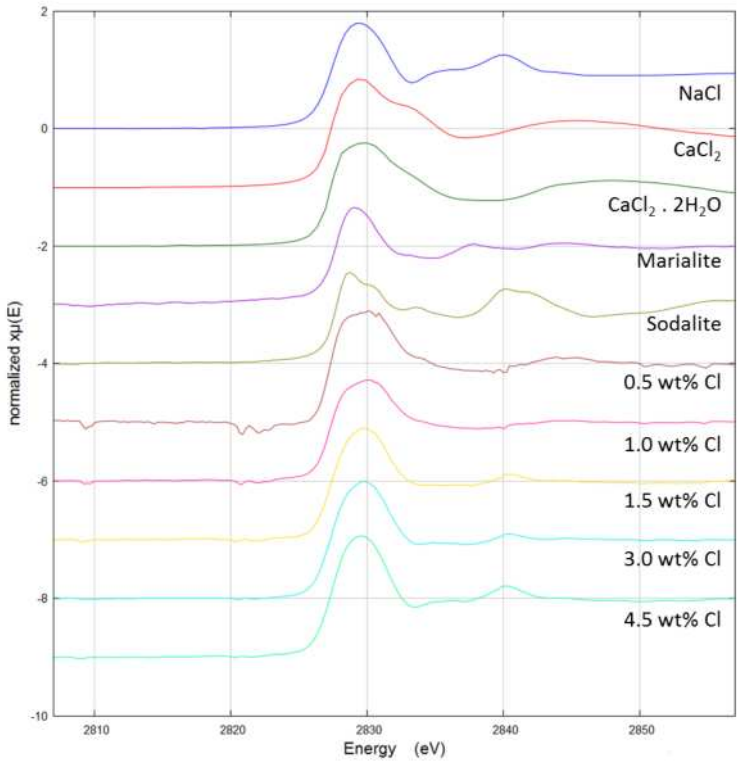

Figure 1: Cl K edge spectra from glass ceramic samples given in Table 1 and reference standards.

Scientific output

We expect that the experiment will produce at least one full good quality journal paper (e.g. submitted to J. Nucl. Mater. or Int. J. Appl. Glass Sci.). This experiment will contribute data to the PhD thesis of co-experimenter Ms. Stephanie Thornber, who has fabricated and characterised the samples to be studied.

Study of the local atomic structure of bromide ions in polymerized ionic liquids

Mirko Elbers[1], Christian Sternemann[1], Ralph Wagner[2], Metin Tolan[1] and Catalin Gainaru[1]

[1]Fakultät Physik/DELTA, TU Dortmund, 44221 Dortmund, Germany

[2]Bergische Universität Wuppertal, 42119 Wuppertal, Germany

Understanding the structural foundation governing the charge transport is the key for any rational design of electrochemical materials with large energy storage and transport capabilities. In this respect, amorphous conductors such as ionic liquids (ILs) and polymer electrolytes are well investigated [1,2,3]. However, information on the strongly emerging class of materials formed by polymerized ionic liquids (PolyILs) is sparse, largely due to the fact that these compounds are still not yet commercially available. At variance with other materials, PolyILs are prepared through direct covalent bonding of functional monomers containing IL fragments [4], hence combing the benefits of ILs in terms of high charge density with those of polymers in terms of mechanical stability. PolyILs are interesting not only from engineering perspectives: Considering the striking difference between the mobilities of their anions and cations, PolyILs are regarded as model systems in which only one type of ions (here Br) governs the conductivity. In other words, they are perfect testing grounds for many phenomenological and theoretical approaches.

In a recent work we analyzed the ionic diffusivity in several PolyILs by employing dielectric spectroscopy combined with nuclear magnetic resonance and differential scanning calorimetry [5]. Based on the results from these dynamical methods, we propose a new approach to estimate the single-ion diffusivity from the conductivity relaxation spectra directly, without any adjustable parameters. This model connects the elementary diffusion step of the ions with structural details such as the interionic distance and local charge coordination number. Thus, several ionic liquids and PolyILs with different chain lengths were investigated by extended x-ray absorption fine structure (EXAFS) measurements, which provide an insight into the local environment of the bromide ions.

We performed the EXAFS measurements at beamline BL10 of DELTA in transmission and fluorescence geometry simultaneously utilizing an ionization chamber and a wide angle PIN diode, respectively. In order to measure the Br K-edge, a Si(111) channel cut monochromator was used to scan the energy in a range from 13.274 keV to 14.394 keV. The PolyILs were measured in a custom-made sample holder with a beam size of 1x1.5 mm^2 (v x h). For the monomer ionic liquids 0.7mm thick capillaries and a beam size of 0.7x2.5 mm^2 were used. All samples were measured with an acquisition time of approximately 4.5 hours.

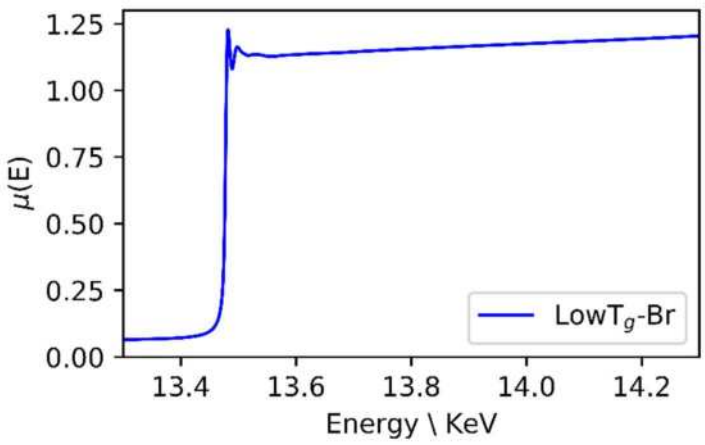

Figure 1: Raw EXAFS fluorescence spectrum for the LowT$_g$-BR PolyIL

A raw spectrum of the PolyIL with the longest chain length *LowTg-Br,* recorded with the wide angle PIN diode in fluorescence geometry, is shown in Figure 1. Standard background subtraction

algorithms were used to extract the characteristic EXAFS oscillation [6]. Figure 2 (a) shows exemplary the obtained spectra for the *LowTg-Br PolyIL*, plotted in electron momentum (k) space. The spectra are weighted with a factor of k^2 to emphasize the EXAFS oscillation in the relevant k-range. We see significant differences between the polymerized and the non-polymerized ionic liquid. Furthermore we calculated the Fourier transform of the EXAFS oscillation, which gives the pseudo radial distribution function (RDF). This function provides a measure for the number of atoms around the bromide ions as a function of radial distances, as distinct from the 'normal' radial distribution function it is shifted to lower values due to the influence of the atomic potentials. The pseudo-RDF for the *LowTg-Br PolyIL* are shown in Figure 2 (b). Interestingly, the PolyILs exhibit a distinct peak at 2.38 Å which do not occur in the spectra of the non-polymerized ionic liquids. This indicates a slightly higher degree of order in the PolyILs compared to the non-PolyILs. The recorded spectra show excellent the general feasibility to detect small changes in the near environment of the bromide ions in PolyILs. For a direct comparison with the previous ionic diffusivity experiments further measurements at different temperature conditions are necessary. Furthermore, for a quantitative and advanced analysis of the experimental data, calculations of theoretical EXAFS spectra will be performed using structures extracted from molecular dynamic simulations.

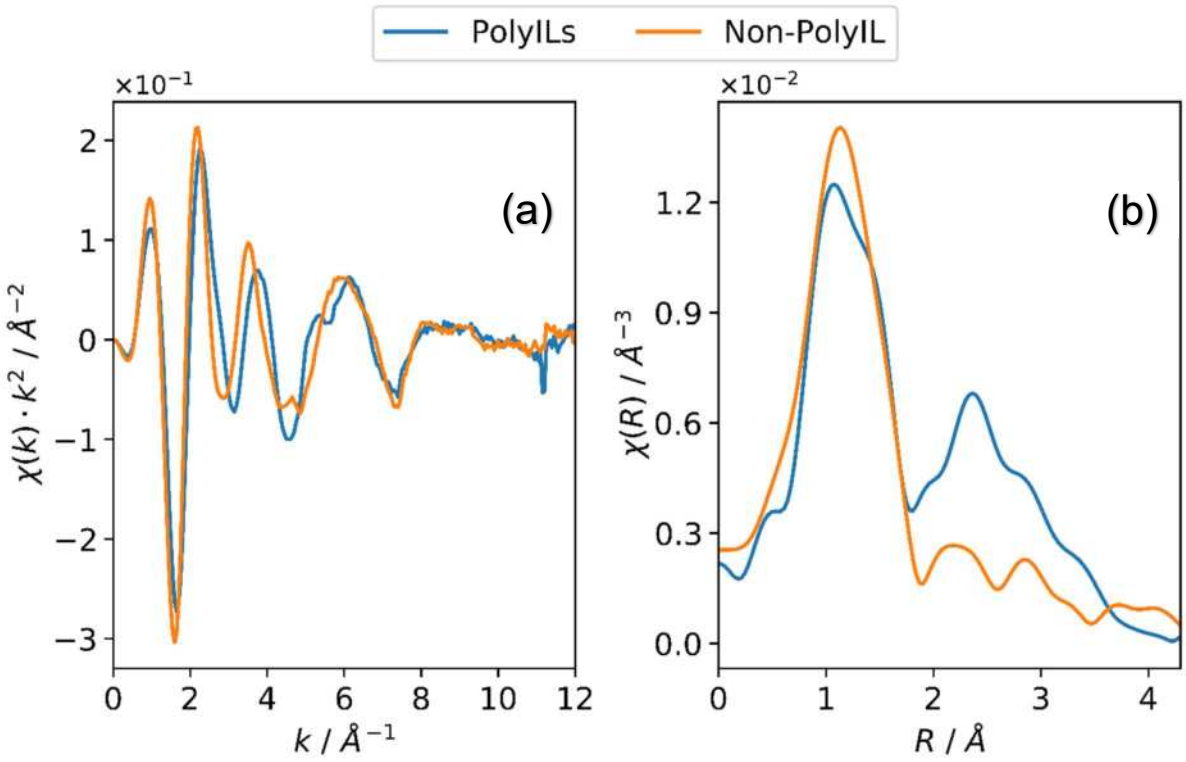

Figure 2: (a) The k^2-weighted EXAFS spectra in momentum space for the LowTg-Br (Non-)PolyIL. (b) Magnitude of the Fourier transform of the spectra in Figure 2 (a)

[1] Ratner, M., Johansson, P., & Shriver, D., Polymer Electrolytes: Ionic Transport Mechanisms and Relaxation Coupling, MRS Bulletin, 25(3), 31-37. (200) (doi:10.1557/mrs2000.16) [2] M. Frey, H. Didzoleit, C. Gainaru and R. Böhmer, Dynamics in Glass Forming Sulfuric and Nitric Acid Hydrates, J. Phys. Chem B 117, 12164-12174, (2013) [3] A. Rivera, T. Blochowicz, C. Gainaru, E. A. Rössler, Spectral response from modulus time domain data of disordered materials, J. Appl. Phys. 96, 5607 (2004) [4] J. Yuan, D. Mecerreyes, M. Antonietti, Poly(ionic liquid)s: an update, Prog. Polym. Sci. 38, 1009 (2013) N. Nishimura, H. Ohno, 15th anniversary of polymerised ionic liquids, Polymer 55, 3289 (2014) [5] C. Gainaru, E.W. Stacy, V. Bocharova, M. Gobet, A.P. Holt, T. Saito, S. Greenbaum and A.P. Sokolov, Mechanism of Conductivity Relaxation in Liquid and Polymeric Electrolytes: Direct Link between Conductivity and Diffusivity, J. Phys. Chem. B 120, 11074-11083 (2016) [6] M. Newville, P. Liviņ, Y. Yacoby, J.J. Rehr and E.A. Stern, Near-edge x-ray-absorption fine structure of Pb: A comparison of theory and experiment, Phys. Rev. B., 47, 14126-14131 (1993)

An Examination on the temperature dependency of Vanadium doped low friction wear resistant PVD coatings

Wolfgang Tillmann[1,a], David Kokalj[1,b] Dominic Stangier[1,c], Leif Hagen[1,d], Christian Sternemann[2,e], Michael Paulus[2,f], Metin Tolan[2,g]

[1]Institute of Materials Engineering, TU Dortmund, Germany
44227 Dortmund, Leonhard-Euler-Straße 2

[2]Fakultät Physik / DELTA, TU Dortmund, University, Germany
44227 Dortmund, Maria-Goeppert-Mayer-Straße 2

[a]wolfgang.tillmann@uni-dortmund.de, [b]david.kokalj@uni-dortmund.de,
[c]dominic.stangier@uni-dortmund.de, [d]leif.hagen@uni-dortmund.de,
[e]christian.sternemann@uni-dortmund.de, [f]michael.paulus@uni-dortmund.de,
[g]metin.tolan@uni-dortmund.de

Keywords: AlCrVN, X-ray diffraction, Magnéli phases, X-ray absorption near-edge structure sprectroscopy, high temperature oxidation, friction

Introduction

Cr-based nitridic PVD-coatings are well-known for their high wear resistance [1] and are often used for protective coatings on tool surfaces [2]. To further enhance the mechanical and tribological properties, several studies focus on the doping of binary coatings with aluminum [3],[4]. On the one hand, the thermal stability and oxidation resistance of the coatings can be improved due to the formation of Al_2O_3 and Cr_2O_3 phases [5], whereas the friction increases in dependency to the aluminum content [6]. On the other hand, the mechanical properties can be modified by substituting chromium with aluminum in the crystal structure up to a ratio of Al/Cr of 3 [7], prior to the occurrence of hexagonal closely packed (hcp) AlN wurtzite structure in addition to the face centered cubic (fcc) structure [8]. Especially, within the context of hot forming, the mentioned outstanding properties fulfill the high demands of the load spectrum with the exception of friction. To modify the friction behavior, a new approach by doping AlCrN coatings with vanadium is chosen. The oxidation of transition metals can lead to changes in the crystalline structure and to the formation of crystallographic shear structures [9–11], so-called Magnéli phases (Me_xO_{2x-1}, Me_xO_{3x-1} or Me_xO_{3x-2}). In the context of vanadium oxides, the homologous series V_nO_{2n-1} with $3 < n$ 10 can be formed [12], in dependence of the temperature and the sliding planes to reduce the friction forces. In addition, due to the low decohesion energy, vanadium pentoxide [12] can serve as a liquid lubricant [13] even at low temperatures (915 K [14] and 943 K [15], and thus can reduce the friction. To understand this phenomenological behavior, a systematic study on the variation of the vanadium content in AlCrN thin films was conducted at elevated temperatures. The changes of the structural properties and oxidation behavior are investigated with X-ray diffraction (XRD) and X-ray absorption near-edge spectroscopy (XANES) and correlated with the resulting friction properties in dependency of the vanadium content.

Experimental setup

As reference material, an AlCrN coating was selected [16], which was doped with an increasing amount of vanadium by adapting the power on the cathode from 1 to 4 kW. The details of the sequence of the heating and etching processes prior to the deposition process, as well as additional information regarding the experimental setup, chemical composition, and mechanical properties, can be found in [17,18]. To investigate the tribological behavior of the AlCrVN coatings, a high-temperature ball-on-disc tribometer was used at temperature levels of RT, 400°C and 700°C under atmosphere with a counterbody of 6 mm (100Cr6). A normal force of 10 N in combination with a relative sliding velocity of 0.4 m/s at a total sliding distance of 500 m was selected for the tribological investigations. According to the heating rate in the Tribometer, the specismes for XRD and XANES were heat-treated equally (400°C = 10 K/min and 700°C = 17 K/min). The XANES measurements were performed on the K-edge (5465 eV) of vanadium in a range between 5405 to 5565 eV. The beam dimension was set to a height of 1 mm and width of 5 mm using an angle of incidence of 5°. The phase evaluation was performed with a photon energy of 20 keV, using the image plate detector MAR345 with a beam size of 1 mm and a width of 0.05 mm. To minimize the influence of the nitrided steel substrate, an angle of incidence of 0.2° was selected.

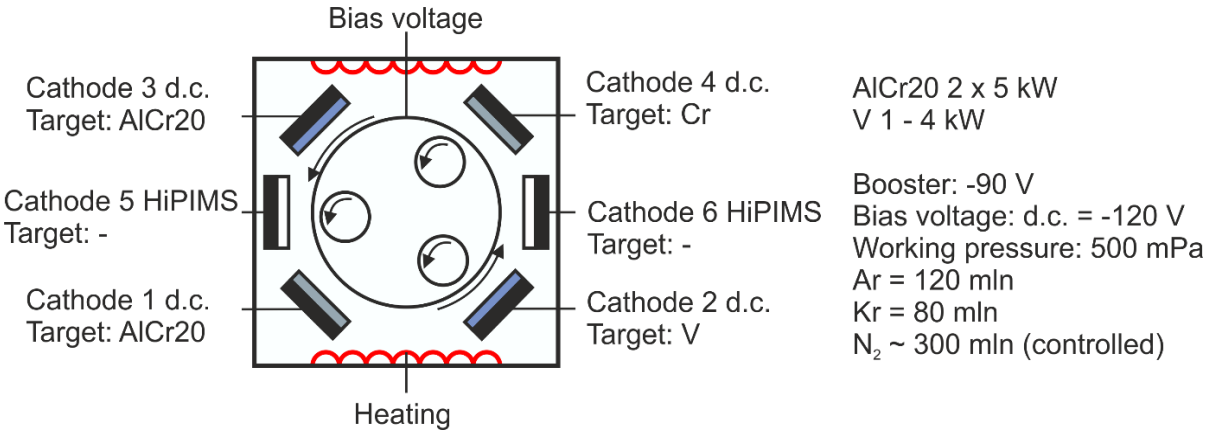

Figure 1: Target configuration and deposition parameters of the AlCrVN coatings

Results

The structural changes in dependency of the vanadium content were analyzed by means of XRD as presented in Figure 2. The as-deposited state of the different coatings reveal that there are no phase changes observed due to the vanadium incorporation. The coatings consist of a fcc solid solution in the NaCl structure, as reported for the CrN coatings. The hexagonal phases of AlN (hcp wurtzite structure) were not detected and therefore a solid solution of Al as well as V is indicated. In dependency to the coating thickness, low intensities of the iron γ' and ε-phases could be observed, which are a result of the nitriding process of the substrate material [19]. Even at a temperature level of 400°C, no phase transformation or oxidation was observed. This is in good correspondence with studies of CrN and CrAlN thin films, showing a thermal stability up to temperatures of 600°C [20]. For higher temperatures of 700°C, a phase separation of the solid solution was detected for the coatings. The AlCrV(1)N and AlCrV(2)N thin films revealed for lower vanadium contents the formation of hexagonal AlN, which is proven by the reflexes at 32.9 and 35.6°. In contrast to these results, higher vanadium contents showed the formation of VN phases due to the additional reflection at 44.1°. With respect to the oxidation behavior, the vanadium content shows a clear dependency. The

formation of oxides can be excluded for the coatings AlCrV(1)N and AlCrV(2)N, whereas several oxides are detected for the systems AlCrV(3)N and AlCrV4)N. The Magnéli phases V_2O_3 and V_4O_7 were as well detected at 700°C, as well some Bragg reflections for VO_2. The formation of CrO_4V is a result of the reaction of Cr_2O_3 withand V_2O_5 at 450°C [21]. The same observation was made for the reaction of Al_2O_3 with V_2O_5 in a temperature range from 600°C to 650°C, forming $AlVO_4$ [22]. Therefore, the formation of vanadium oxides is fostered by vanadium contents above 10 at. %.

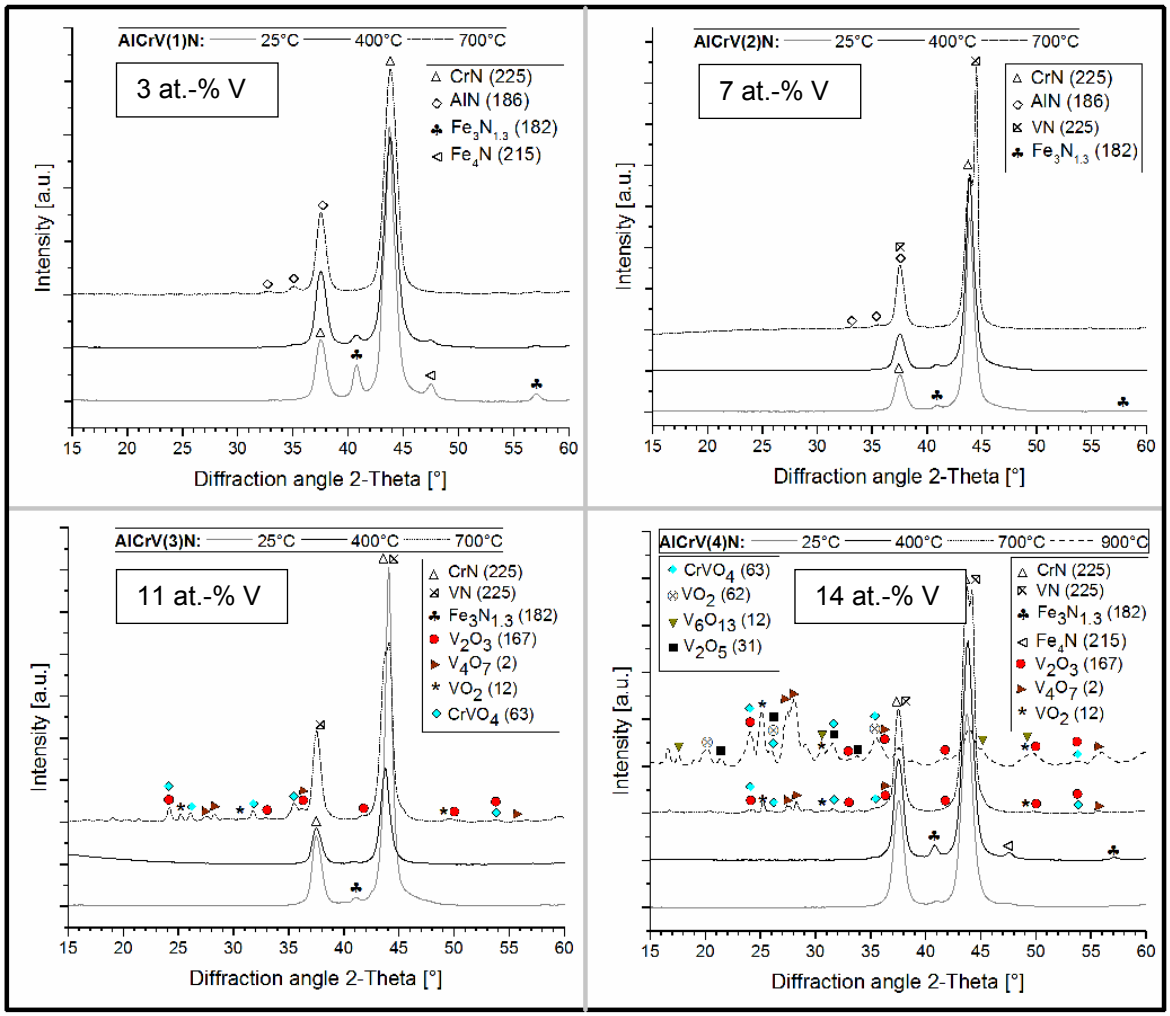

Figure 2: XRD patterns of the as-deposited and annealed AlCrVN coatings [18]

The oxidation state and behavior in detail is analyzed by the XANES spectra presented in Figure 3, taking into account the pre-edge maximum and its centroid position as presented in [23]. A detailed description of the results and the discussion can be found in [18]. Summarizing, no significant changes of the absorption edge could be observed for temperatures up to 400°C. In contrast to that, at a temperature of 700°C, the pre-edge maximum increases and a slight shift to higher energy levels could be observed. A comparison of the main edge position in dependency of the temperature revealed that the position is shifted to higher values for all coatings as well with an increasing vanadium content. Only AlCrV(3)N and AlCrV(4)N show slightly different results due to the formation of $CrVO_4$ and the formation of Magnéli phases and higher order oxides.

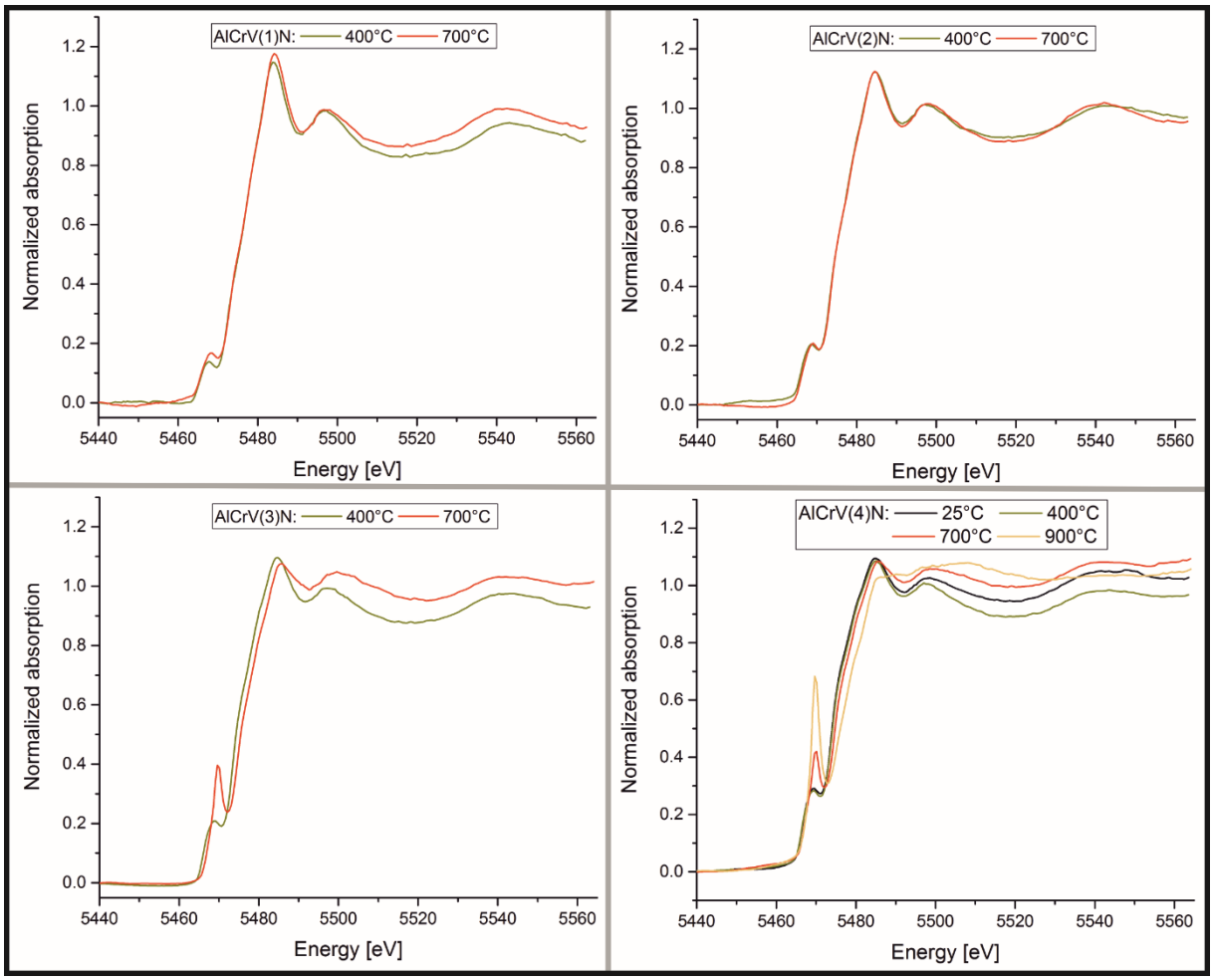

Figure 3: XANES spectra of AlCrVN thin films at RT, 400°C, 700°C, and 900°C for different vanadium contents [18]

Having analyzed the structural changes and the formation of oxides, the effect on the friction behavior is investigated. For room temperature as well as an elevated temperature of 400°C, a constant level of friction was measured. With an increasing temperature of up to 700°C, the level of the coefficient of friction for the lower vanadium contents is increased above the level of RT and 400°C. According to XRD and XANES, the AlCrV(3)N coating shows a higher amount V_2O_3 and $CrVO_4$ phases, compared to the AlCrV(4)N thin film. $CrVO_4$ is known for a higher coefficient of friction compared to Magnéli phases [12]. The decreasing friction of the AlCrV(4)N systems can be attributed to the higher amount of V_4O_7 at 700°C. Nevertheless, the reduction of friction due to the elemental oxidation of vanadium was presented and proven and correlated to the different types of oxides. In further studies, the effect of highly ionized deposition processes such as HiPIMS on the oxidation behavior will be investigated to gain a deeper understanding of the mechanisms involved in the formation of Magnéli phases.

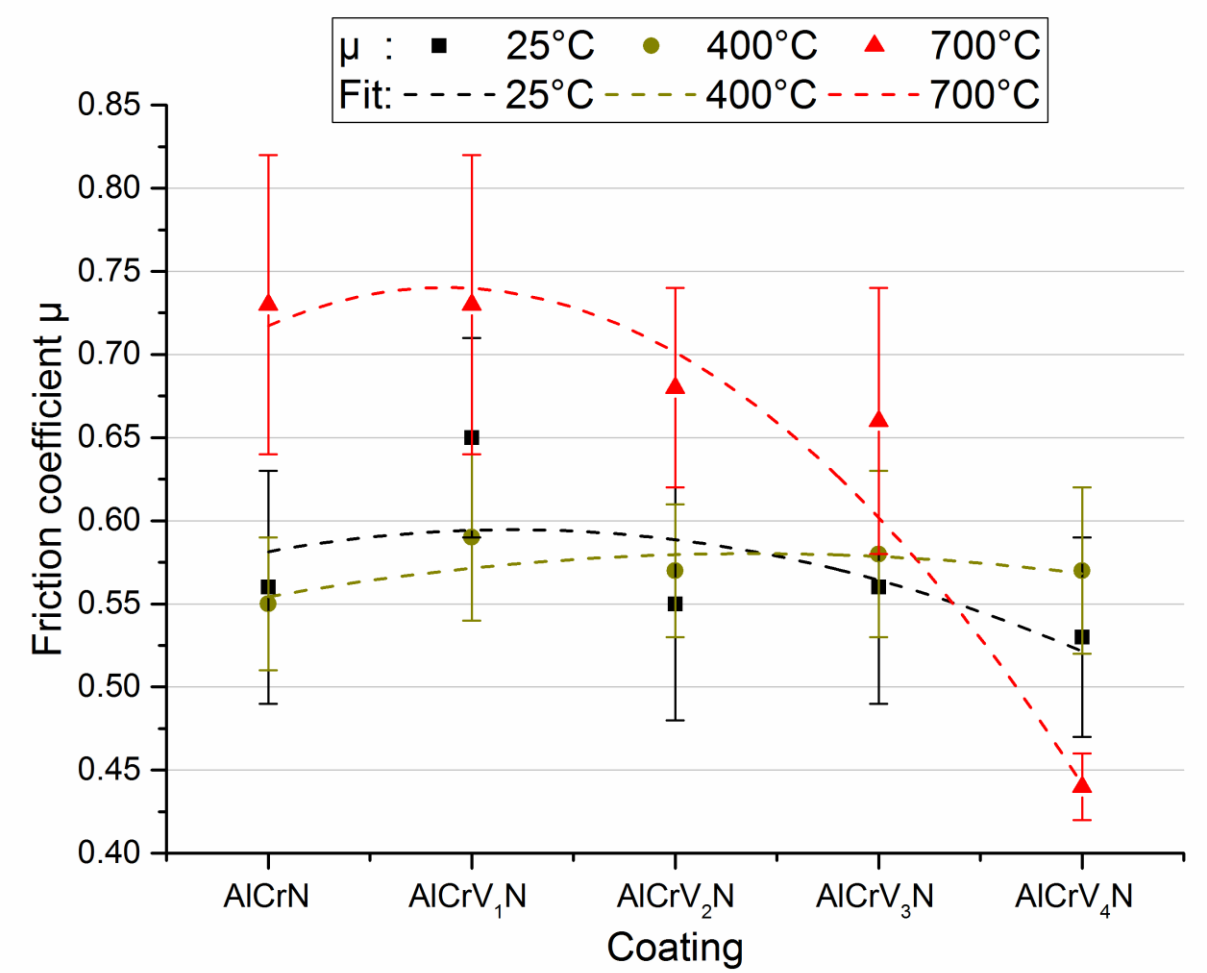

Figure 4: Coefficient of friction of AlCrVN coatings at RT, 400°C, and 700°C [18]

Acknowledgement

The authors thank the DELTA machine group for providing synchrotron radiation at beamline BL9 for X-ray diffraction and BL10 for X-ray absorption experiments. Furthermore, R. Wagner is acknowledged for his valuable support during the XANES measurements performed at beamline BL10.

References

[1] K. Bobzin, E. Lugscheider, R. Nickel, N. Bagcivan, A. Krämer, Wear behavior of Cr1−xAlxN PVD-coatings in dry running conditions, Wear 263 (7-12) (2007) 1274–1280.

[2] K. Bobzin, High-performance coatings for cutting tools, CIRP Journal of Manufacturing Science and Technology (18) (2017) 1–9.

[3] N. Bagcivan, K. Bobzin, S. Theiß, (Cr1−xAlx)N: A comparison of direct current, middle frequency pulsed and high power pulsed magnetron sputtering for injection molding components, Thin Solid Films 528 (2013) 180–186.

[4] X.-Z. Ding, X.T. Zeng, Y.C. Liu, F.Z. Fang, G.C. Lim, Cr1−xAlxN coatings deposited by lateral rotating cathode arc for high speed machining applications, Thin Solid Films 516 (8) (2008) 1710–1715.

[5] O. Banakh, P. Schmid, R. Sanjinés, F. Lévy, High-temperature oxidation resitance of Cr1-xAlxN thin films deposited by reactive magnetron sputtering, Surface and Coatings Technology (163-164) (2003) 57–61.

[6] M. Brizuela, A. Garcia-Luis, I. Braceras, J.I. Oñate, J.C. Sánchez-López, D. Martínez-Martínez, C. López-Cartes, A. Fernández, Magnetron sputtering of Cr(Al)N coatings: Mechanical and tribological study, Surface and Coatings Technology 200 (1-4) (2005) 192–197.
[7] Y. Makino, K. Nogi, Synthesis of pseudobinary Cr-Al-N films with B1 structure by rf-assisted magnetron sputtering method, Surface and Coatings Technology (98) (1998) 1008–1012.
[8] A. Sugishima, H. Kajioka, Y. Makino, Phase transition of pseudobinary Cr–Al–N films deposited by magnetron sputtering method, Surface and Coatings Technology 97 (1-3) (1997) 590–594.
[9] G. Gassner, P. Mayrhofer, K. Kutschej, C. Mitterer, M. Kathrein, A new low friction concept for high temperatures: lubricous oxide formation on sputtered VN coatings, Tribology Letters (4) (2004) 751–752.
[10] O. Storz, H. Gasthuber, M. Woydt, Tribological properties of thermal-sprayed Magnéli-type coatings with different stoichiometries (TinO2n-1), Surface and Coatings Technology (140) (2001) 76–81.
[11] V. Perfilyev, A. Moshkovich, I. Lapsker, A. Laikhtman, L. Rapoport, The effect of vanadium content and temperature on stick–slip phenomena under friction of CrV(x)N coatings, Wear 307 (1-2) (2013) 44–51.
[12] T. Reeswinkel, D. Music, J.M. Schneider, Ab initio calculations of the structure and mechanical properties of vanadium oxides, Journal of Physics: Condensed Matter 21 (14) (2009) 145404.
[13] R. Franz, C. Mitterer, Vanadium containing self-adaptive low-friction hard coatings for high-temperature applications: A review, Surface and Coatings Technology 228 (2013) 1–13.
[14] H. Wriedt, The O-V (Oxygen-Vanadium) System, Bulletin of Alloy Phase Diagrams (10) (1989) 271–277.
[15] D. Lide, CRC Handbook of Chemistry and Physics: A Ready-reference Book of Chemical and Physical Data, 85th ed., CRC Press, Boca Raton, 2004.
[16] P. Sieczkarek, S. Wernicke, S. Gies, A.E. Tekkaya, E. Krebs, P. Wiederkehr, D. Biermann, W. Tillmann, D. Stangier, Wear behavior of tribologically optimized tool surfaces for incremental forming processes, Tribology International 104 (2016) 64–72.
[17] W. Tillmann, D. Kokalj, D. Stangier, M. Paulus, C. Sternemann, M. Tolan, Investigation of the influence of the vanadium content on the high temperature tribo-mechanical properties of DC magnetron sputtered AlCrVN thin films, Surface and Coatings Technology 328 (2017) 172–181.
[18] W. Tillmann, D. Kokalj, D. Stangier, M. Paulus, C. Sternemann, M. Tolan, Investigation on the oxidation behavior of AlCrVxN thin films by means of synchrotron radiation and influence on the high temperature friction, Applied Surface Science 427 (2018) 511–521.
[19] T. Sprute, W. Tillmann, D. Grisales, U. Selvadurai, G. Fischer, Influence of substrate pre-treatments on residual stresses and tribo-mechanical properties of TiAlN-based PVD coatings, Surface and Coatings Technology 260 (2014) 369–379.
[20] J. Lin, B. Mishra, J.J. Moore, W.D. Sproul, A study of the oxidation behavior of CrN and CrAlN thin films in air using DSC and TGA analyses, Surface and Coatings Technology 202 (14) (2008) 3272–3283.
[21] M.J. Isasi, R. Sáez-Puche, M.L. Veiga, C. Pico, A. Jerez, Synthesis and magnetic properties of crystalline CrVO4, Materials Research Bulletin 23 (4) (1988) 595–601.
[22] O. Yamaguchi, T. Uegaki, Y. Miyata, K. Shimizu, Formation of AlVO4 Solid Solution from Alkoxides, Journal of the American Ceramic Society 70 (8) (1987) C-198-C-200.
[23] J. Wong, F.W. Lytle, R.P. Messmer, D.H. Maylotte, K-edge aborption spectra of selected vanadium compounds, Phys. Rev. B 30 (10) (1984) 5596–5610.

Impact of pressure on the volume fraction of lysozyme in crowded solutions

Karin Julius[1], Miren Büyükasik[1], Christian Sternemann[1], Michael Paulus[1], Paul Salmen[1], Metin Tolan[1], and Roland Winter[2]

[1] *Fakultät Physik / DELTA, Technische Universität Dortmund, 44227 Dortmund, Germany*

[2] *Fakultät für Chemie und Chemische Biologie, Technische Universität Dortmund, 44227 Dortmund Germany*

Inside cells, proteins are surrounded by different macromolecules, including proteins themselves, which cover approximately 30% of the available volume. It has been shown that the reduction of free space and the accompanied change of osmotic pressure has a significant impact on the conformational stability, dynamics and hence reactivity of proteins, which changes also their resistance to temperature or pressure-induced denaturation [1-9].
The conformation of the protein lysozyme was found to be stable in pure buffer in a pressure range up to 5 kbar [10]. The solution properties, however, such as the isothermal compressibility at high pressure depends strongly on the protein concentration. Knowledge of the volume fraction, occupied by the protein in the sample volume, is crucial for the advanced analysis of small-angle X-ray scattering data in order to investigate the impact of crowding on the pressure dependent intermolecular interaction potential of proteins in highly concentrated aqueous lysozyme solutions.

The aim of the experiment was the investigation of the impact of crowder molecules of various sizes and chemical properties on the compressibility of highly concentrated aqueous lysozyme solutions at pressures up to 4500 bar, and how the partial specific volume of lysozyme is modulated by changes in the solution properties imposed by these crowders. As model crowding agent, polymer polyethylene glycol (PEG) of the molecular weights 0.2 kDa, 0.6 kDa, 2 kDa, 4 kDa and 8 kDa and sucrose were chosen. To obtain the partial specific volume fraction of lysozyme as a function of crowder concentration and crowder identity, absorption spectra of 10 (w/v) % aqueous lysozyme solutions in 25 mM BisTris buffer at pH 7 were recorded for crowder concentrations ranging from 0 to 50 wt.-%. At 25°C and ambient pressure, the partial specific volume of lysozyme at infinite dilution was found to be $\Phi_v^0 = 0.742$ mL g^{-1} [11]. Based on the finding of a pressure resistant conformation of lysozyme and given that the protein is dissolved in the same volume regardless of the crowder concentration, the specific volume fraction ϑ of lysozyme in solution at elevated pressures and different crowding conditions can be calculated directly from Φ_v^0 and the measured density, ρ, of the solution (FIG. 1(D)).

X-ray transmission measurements in an energy range from 16.86 to 16.91 keV with an increment of 1 eV and a counting rate of 5 s were performed at DELTA BL8, with a custom build high pressure cell [12] in the pressure range from 50 – 4500 bar in 500 bar steps at a sample temperature of 25 °C. By measuring the radiant flux received and transmitted by the sample of thickness *d*, employing ion chambers filled with Argon and Xenon at 1 atm, the linear attenuation coefficient and thus the density of the sample for all pressures relative to 50 bar can be determined by Lambert-Berr law. The mass densities of the samples are normalized to an absolute scale by complementary density measurements at ambient pressure employing an *Anton Paar DSA 5000* density and sound velocity meter (FIG. 1(B)).

Applying pressure leads to a reduction of the volume of the sulotion and hence an increase of the volume fraction of the protein. Due to the reduction of the solutions volume, the effective volume occupied by the

protein increases. Even though sucrose leads to a markedly stronger increase in density at the same concentration as PEG at ambient pressure, the compressibilities of the solutions are comparable for all crowder conditions.

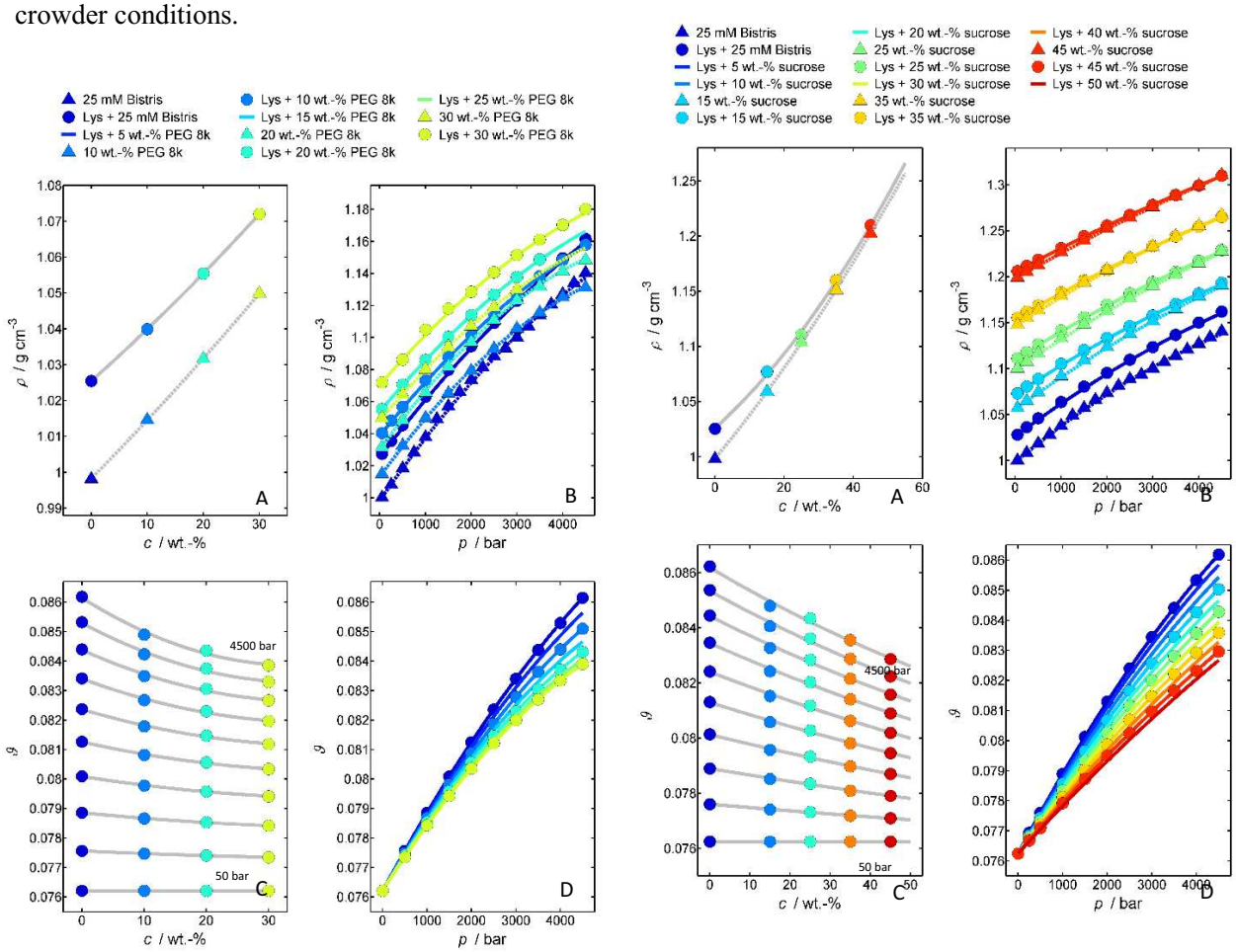

FIG. 1 Experimental absolute mass densities, ρ, of a 10 (w/v)% lysozyme + 25 mM BisTris (pH 7) solution at 25 °C for PEG 8k (sucrose) concentrations of 0 to 50 wt.-% and the refinement of the data at ambient pressure in dependence of the PEG 8k (sucrose) concentration (A) and in dependence of hydrostatic pressure (B). Calculated protein volume fraction ϑ at ambient pressure in dependence of the crowder concentration c (C) and at pressures p (D)

1. A. P. Minton, *J. Cell Sci.*, 2006, **119,** 2863–2869.
2. A. P. Minton, *Biophys. J.*, 2005, **88,** 971–985.
3. H. X. Zhou, *Arch. Biochem. Biophys.*, 2008, **469,** 76–82.
4. M. Erlkamp, S. Grobelny and R. Winter, *Phys. Chem. Chem. Phys.*, 2014, **16,** 5965–5976.
5. M. Erlkamp, J. Marion, N. Martinez, C. Czeslik, J. Peters and R. Winter, *J. Phys. Chem. B*, 2015, **119,** 4842–4848.
6. R. Ellis, *Trends Biochem. Sci.*, 2001, **26,** 597–604.
7. B. van den Berg, R. J. Ellis and C. M. Dobson, *EMBO J.*, 1999, **18,** 6927–6933.
8. R. J. Ellis, in *Molecular Aspects of the Stress Response: Chaperones, Membranes and Networks*, eds. P. Csermely and L. Vígh, Springer New York, 2007, **594**, 1–13.
9. M. S. Cheung, D. Klimov and D. Thirumalai, *Proc. Natl. Acad. Sci. U. S. A.*, 2005, **102,** 4753–4758.
10. M. Schroer, J. Markgraf, D.C.F. Wieland, C.J. Sahle, J. Möller, M. Paulus, M. Tolan, and R. Winter, *Phys. Rev. Lett.,* 2011, **106**, 178102-1 – 178102-4
11. F.J. Millero, G. Ward, and P.J. Chetirkin, *Bio. Chem.,* 1976, **251**, 4001-4004.
12. C. Krywka, C. Sternemann, M. Paulus, M. Tolan, C. Royer, and R. Winter, *Chem. Phys. Chem.*, 2008, **9**, 2809–2815.

X-ray fluorescence and X-ray diffraction analysis of a historical painting

Fatima Mallal, Alex von Bohlen, Michael Paulus, Anne K. Hüsecken, Paul Salmen, Christian Sternemann, Wolf-Dieter Köster, Jörg Hansen and Metin Tolan

Fakultät Physik/DELTA, TU Dortmund, 44221 Dortmund, Germany

Email: fatima.mallal@tu-dortmund.de

The aim of the experiment is to analyze the colors used for a painting, presumably a portrait of Johann Sebastian Bach (1685-1750), in order to constrain its authenticity and to identify if corrections of the painting have been made in the subsequent centuries. For this purpose the portrait was analyzed using synchrotron X-ray radiation at beamline BL9 at DELTA exploiting two different methods. The qualitative and quantitative determination of the elemental composition of a sample at a certain position on the painting was determined by X-ray fluorescence (XRF) analysis. The fluorescence radiation, which exhibits fluorescence radiation charactaristic for each element containt in the painting, has been recorded using an Amptek Si-Pin diode X123 detector. In order to analyze the crystal structure of colours and pigments X-ray diffraction (XRD) was applied. Diffraction patterns were captured parallel to the fluorescence analysis using a MAR345 image plate detector. The illuminated area on the painting was 1x1mm^2. The corresponding experimental setup is shown in figure 1.

Fig. 1: Experimental setup for materials characterization at beamline BL9 of DELTA. The fluorescence detector analyzes X-ray fluorescence in backscattering and the MAR345 detector (left) acquires diffraction pattern in transmission geometry. The painting is mounted on horizontal and vertical translation stages.

The Bach painting was positioned between the source of incident radiation (right) and the MAR345 detector (left). The Amptek detector was placed at an angle about 45 degrees oblique to the sample. This measurement was carried out at room temperature with an incident photon energy of 20keV. We have measured at several positions in different parts of the painting to obtain a thorough overview on different colors used. By XRF analysis we identified the elements lead, zinc, calcium and barium in high amount. A typical fluorescence spectrum is presented in figure 2.

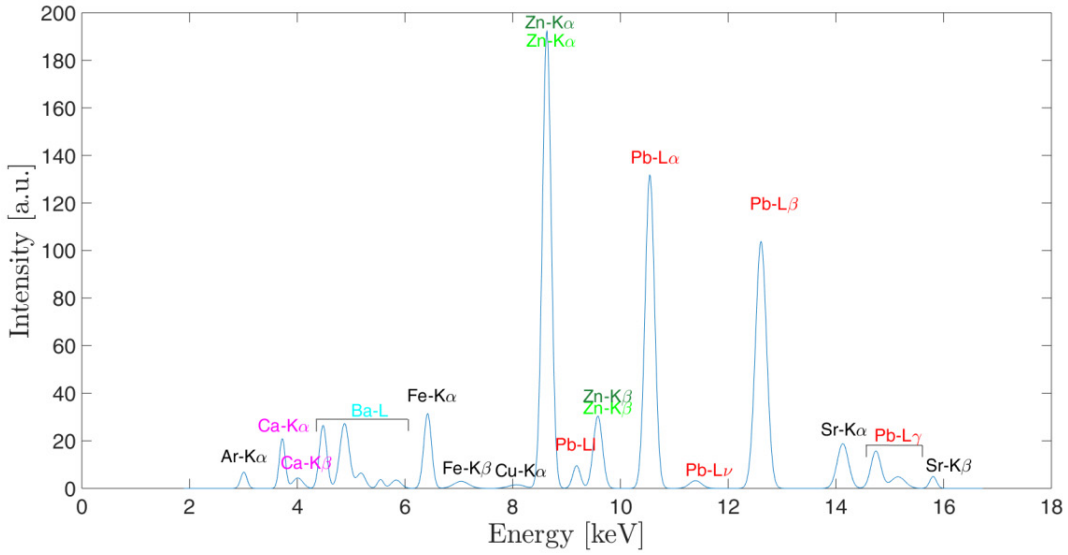

Fig. 2: Typical X-ray fluorescence spectrum recorded at the upper part of the painting within the white region of Bach's hairs.

Diffraction patterns were measured in order to identify distinct colors used. Therefore, diffraction patterns of reference samples were measured, i.e. of the white colors lead white (ancient), zinc white (use started 1830/1850) and lithopone (1850). The diffraction pattern that corresponds to the XRF spectrum of figure 2 is shown in figure 3. Here we identify strong contribution of lead white ($(PbCO_3)_2$ $Pb(OH)_2$) and lithopone ($BaSO_4$ ZnS) with only negligible amount of zinc white (ZnO). Furthermore, we found fingerprints of chalk ($CaCO_3$) explaining the high amount of calcium in the fluorescence spectrum. However, for a statement about the time of issue of the painting all measured XRD and XRF spectra have to be evaluated carefully. This is in progress.

The authors thank the DELTA machine group for providing synchrotron radiation.

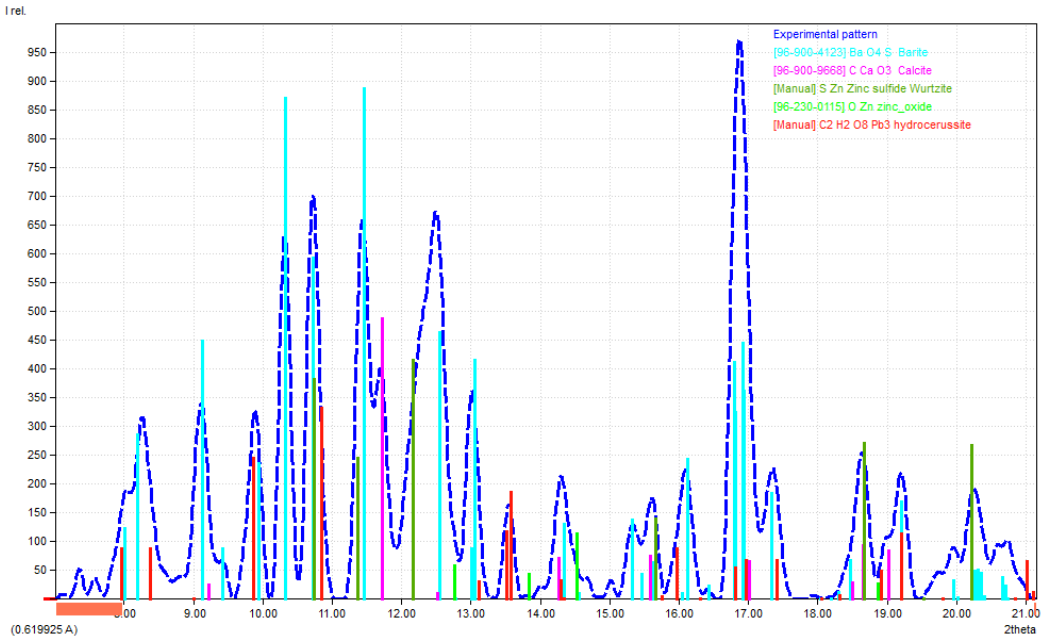

Fig. 3: Typical X-ray diffraction pattern measured at the upper part of the painting within the white region of Bach's hairs.

EXAFS investigations of Niobium processed in vacuum and different gas atmospheres

J. Kläs, R. Wagner, B. Bornmann, R. Frahm, D. Lützenkirchen-Hecht

Fakultät 4-Physik, Bergische Universität Wuppertal, Gaußstr. 20, 42097 Wuppertal, Germany

Tailored properties of many metals and alloys may be obtained using high-temperature treatments in gas atmospheres. Here we are interested in the structural modifications of niobium, in particular in N_2-atmospheres. Such a treatment has been recently introduced for high-temperature nitriding of superconducting Nb-cavities, leading to substantially improved RF-superconductivity in mid acceleration fields recently [1]. In 2017, we continued our activities in EXAFS measurements of heat-treated Nb foils. Nb K-edge (18986 eV) EXAFS experiments were conducted at DELTA beamline 8 using the Si(311) monochromator and gas-filled ionization chambers as detectors. Until now Nb foils of different thickness have been heated to about 900 °C in vacuum for one hour and been processed in diluted nitrogen gas. The samples were measured both in-situ at high temperature during the gas exposure as well as ex-situ after cooling down to room temperature, and some of the samples were also measured at liquid nitrogen temperatures in order to further pronounce any structural changes with the heat-treated samples. As we will show here, slight changes of the short-range order within the Nb-foil samples could also be detected if the samples are only heated in vacuum, without any additional gas load in the process chamber.

In Fig. 1, the modeled EXAFS data of a 25 μm Nb foil processed in vacuum only is shown. For the data analysis, the bcc-structure of Nb was assumed, and no Nb-N or Nb-O coordinations were required to obtain a significant fit. For the purpose of this report, only the first two nearest neighbors were considered, and a free parameter fit was performed using the Artemis software [2].

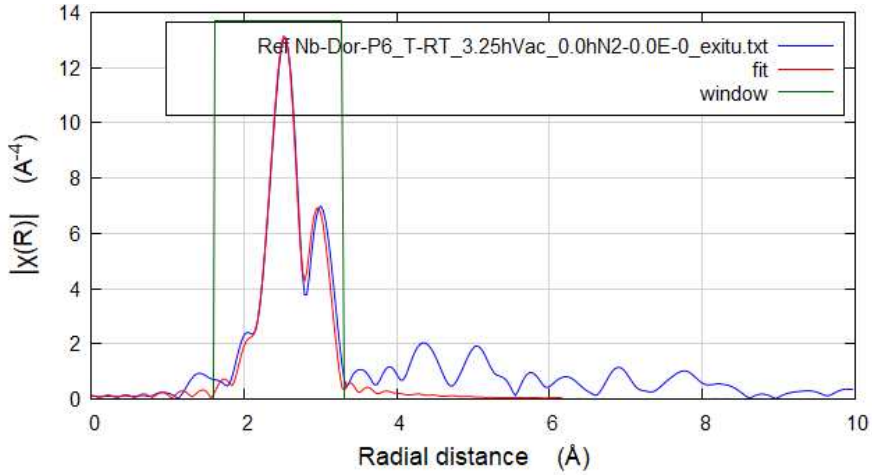

Fig. 1: Fit results obtained for a Nb foil (25 μm thickness) heat-treated in vacuum (10^{-7} mbar) at 900 °C for 2 hours. The sample was cooled down to room temperature in vacuum. A bcc-structure model including the first two Nb-Nb-coordinations was used (data are not corrected for phase-shifts. K-range for the Fourier-transform 1.8 $Å^{-1}$ < k < 15 $Å^{-1}$.)

The systematic investigation of various samples prepared for different temperatures and under a variation of the process time and the process gases indicated that no substantial changes of the bcc structure occurred. However, small but distinct structural modifications are detectable. In particular, an irreversible decrease in amplitude with time is obvious for all coordination shells, as well as a slight shift of the peaks to higher radial distances can be observed. The quantitative fitting of the measurements performed so far indicate that the disorder parameter for the Nb-Nb-coordinations increases as a function of the heating time, irrespective of a possible gas exposure with partial pressures in the range of up to 10^{-3} mbar. In Fig. 2, values determined for σ^2 for the second Nb-Nb shell are presented.

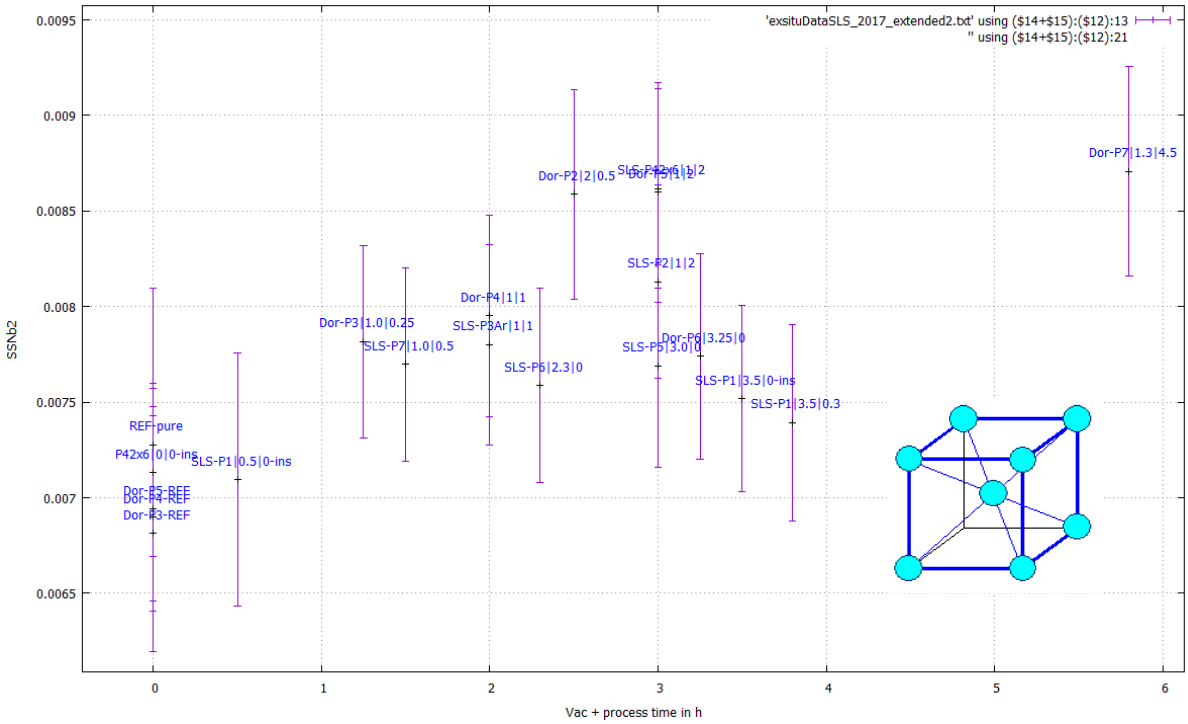

Fig. 2: Plot of σ^2 for the second Nb-Nb shell in bcc Nb as determined from a quantitative EXAFS data fitting as a function of the process time for various vacuum and nitrogen treated Nb foils as indicated. The disorder shows a slightly increasing trend as a function of the duration of the heat treatment, irrespective of the actual heating conditions. The inset shows the bcc-structure, with tetrahedral cavities between the Nb-atoms at the edges of the cubic unit cell.

In the bcc structure, distinctive cavities are present Nb-atoms at the corners of the cube (see inset in Fig. 2). Those locations appear to be promising candidates for interstitial atoms in the bcc-structure, and it is thus likely that absorbed gas atoms or molecules may reside on those positions. Thus, the investigation of the disorder parameter σ^2 of the second Nb-Nb-shell (the first shell corresponds to the corner atoms and the center atom in the bcc unit cell) is a sensitive parameter for the occupation of those sites, i.e. the increase of σ^2 during the heat treatments may indicate that either doping gas or residual gas from the vacuum system enters the Nb structure and occupies those tetrahedral cavities.

Further measurements on vacuum heated samples have been performed lately in September 2017, however those data still needs to be analyzed in detail. It is expected to gain more insight in the details of gas uptake by using other gases such as argon, krypton and xenon, that are substantially larger compared to the gases used so far. Those experiments are planned for the near future.

Acknowledgements

We gratefully acknowledge the DELTA machine group for providing synchrotron radiation reliably. We would like to thank O. von Polheim and P. Becker for their help with the experiments at the beamlines.

References

[1] A. Grasselino, A. Romanenko, D. Sergatskov, et al., Supercond. Sci. Technol. 26 (2013) 102001
[2] B. Ravel, M. Newville, J. Synchrotron Radiat. 12 (2005) 537

Post-deadline contributions

First Results from the Short-Pulse Narrowband THz Source at DELTA

C. Mai, B. Büsing, S. Khan, N. Lockmann,
A. Meyer auf der Heide, B. Riemann, B. Sawadski, P. Ungelenk
Zentrum für Synchrotronstrahlung (DELTA), Technische Universität Dortmund

Overview

At the DELTA short-pulse facility [1], a laser-electron interaction is routinely used to produce THz radiation between 75 GHz and 5.6 THz. The generation principle is based on an energy modulation of relativistic electrons in an electromagnetic undulator. Figure 1 shows the longitudinal electron distribution after a laser electron interaction in three different situations. A method thoroughly studied during the last years is the formation of a single dip caused by the laser interaction, giving rise to the coherent emission of THz radiation. Recently, a setup to produce multiple dips in the longitudinal charge density was commissioned allowing to generate narrowband radiation in the (sub-)THz regime (see Fig. 1, right). To realize this configuration, an intensity modulation of the laser seed pulse is required. Here, the chirped-pulse beating technique is used, in which two chirped laser-pulse copies interfere producing a laser intensity beating [2,3].

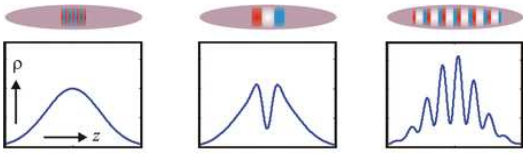

Figure 1: Left: Longitudinal profile of the electron bunch with a central energy modulation caused by the laser-electron interaction. Center: Dispersion leads to the formation of a dip giving rise to broadband THz radiation. Right: A several picoseconds long, intensity modulated laser pulse is used to imprint a density modulation onto the electron bunch resulting in narrowband (sub-)THz radiation [4].

The experimental setup to produce narrowband THz radiation is shown in Fig. 2. A laser interferometer is used to create two chirped laser pulses being several picoseconds long.

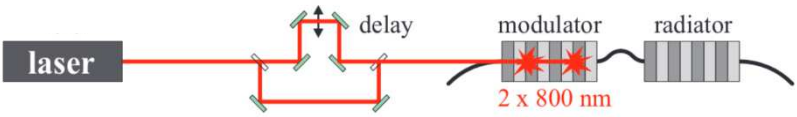

Figure 2: Left: The interference of chirped laser pulses is used to generate laser pulses with a tunable intensity modulation in the picosecond range (see text for details) [5].

Laser Diagnostics for Chirped-Pulse Beating

The laser setup at DELTA was extended by an interferometer to generate the beating and an intensity autocorrelator for laser diagnostics. An autocorrelation signal of the modulated laser pulse is shown in Fig. 3 (left). The modulation frequency is tunable by a remote-controlled piezo delay line. The calibration of the chirped-pulse beating setup (see Fig. 3, right) shows a linear correlation between the interferometer delay and the modulation frequency.

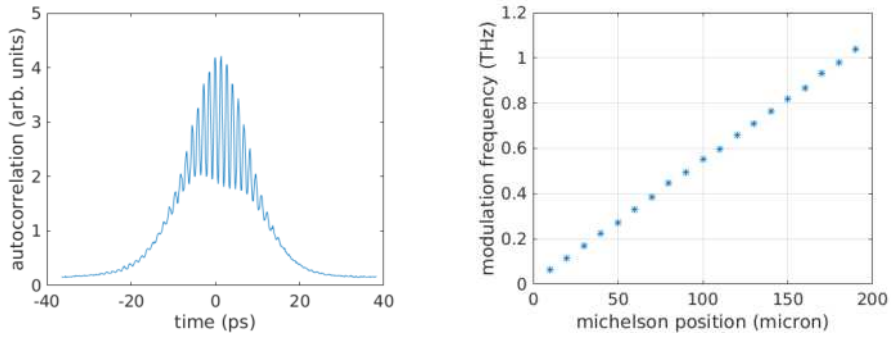

Figure 3: Left: Intensity autocorrelation of the modulated laser pulse. Right: Calibration of the modulation frequency and the laser interferometer setting (see text for details) [6].

Generation and detection of narrowband THz radiation

The spectral response and the overall performance of commercially available detectors are difficult to compare. To provide a test procedure to measure the spectral response of different narrowband THz detectors, the narrowband source at DELTA was used to perform fast sub-THz frequency sweeps. The respective data for 5 detectors are presented in Fig. 4. Each detector was tested in a frequency range between 75 GHz and 1 THz. Detailed simulation studies of the narrowband THz generation process are currently ongoing to further improve the setup. Here, one aim is to decrease the spectral broadening at higher frequencies.

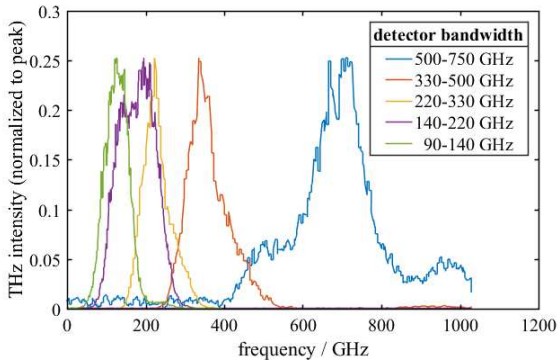

Figure 4: The chirped-pulse beating scheme allows for a fast change of the THz frequency. Tests of the spectral response of narrowband Schottky detectors were performed (see text for details) [6].

References

[1] M. Höner et al., *A dedicated THz Beamline at DELTA*, IPAC 2011, San Sebastian, Spain, 2939.

[2] S. Bielawski, *Tunable narrowband terahertz emission from mastered laser-electron beam interaction*, Nat. Phys. 4, 390 (2008).

[3] P. Ungelenk et al., *Continuously tunable narrowband pulses in the THz gap from laser-modulated electron bunches in a storage ring*, Phys. Rev. Accel. Beams 20, 020706 (2017).

[4] S. Khan, *Ultrashort Pulses from Synchrotron Radiation Sources*, in: E. Jaeschke, S. Khan, J. R. Schneider, J. B. Hastings (Eds.), Synchrotron Light Sources and Free-Electron Lasers, Springer (2015).

[5] S. Khan et al., *Seeding of Electron Bunches in Storage Rings*, Proc. FEL 2017, Santa Fe, USA, MOP027.

[6] C. Mai et al., *A THz Detector Benchmark Campaign at DELTA*, Workshop on Longitudinal Diagnostics, Villigen, Switzerland (2017).

Notes

Notes